Multiscale computational study of polymer solar cell active layers

by

Jan Ulric M. Garcia

A thesis submitted in partial fulfillment of the requirements for the degree of

Master of Science

in

Chemical Engineering

Department of Chemical and Materials Engineering
University of Alberta

Abstract

Solar energy holds great potential in securing humanity's energy future in a sustainable manner. Unfortunately, the costs of silicon photovoltaics continue to impede the use of solar energy. Polymer solar cells (PSCs) can make solar energy more affordable due to their lower production costs. However, PSC efficiencies remain too low to compete with silicon photovoltaics. One of the most important factors affecting PSC efficiencies is the phase morphology of the device active layers. To achieve the most efficient devices, a lamellar morphology is ideal.

Using block copolymers in the active layer is a promising strategy to achieve the desired lamellar morphology. In this strategy, the polymer electron donor and the polymer electron acceptor are spliced covalently at one end. This unique structure allows the donor and acceptor to form lamellar phase domains with sizes around 10 nm. This strategy was shown to be effective with poly(3-hexylthiophene) (P3HT) as the donor and poly((9,9-dioctylfluorene)-2,7-diyl-alt-[4,7-bis(thiophen-5-yl)-2,1,3-benzothiadiazole]-2',2"-diyl) (PFTBT) as the acceptor. However, much optimization is still necessary to the design and processing of the active layer materials. One fundamental factor is P3HT regioregularity (RR). The percent RR is defined as the fraction of head-to-tail bonds in the polymer backbone. In terms of processing, device annealing temperature must also be optimized. In this dissertation, both factors were studied using multiscale computational modeling. Atomistic molecular dynamics (MD) simulations were used to calculate the Flory-Huggins interaction parameter (χ) between P3HT and PFTBT under different values of RR and temperature. The calculated χ values were then used as inputs for mesoscopic dissipative particle dynamics (DPD) simulations to predict the active layer phase morphologies of the P3HT-PFTBT system under different conditions.

Through MD simulations, the average χ parameter values were estimated to be 3.3 for RR < 50%, 1.6 for RR=63%, and 0.9 for RR ≥ 90%. This χ-RR trend was attributed to the increased π-π stacking for lower RR values in the simulated amorphous phase. The cause for the RR-π-π stacking relationship remained unclear; the issue was not explored any further due to the time constraints of this dissertation. For temperatures from 373 K to 503 K, the χ parameter was found to follow a linear relationship with the reciprocal of the absolute temperature (1/T). The slope and intercept of the χ vs. (1/T) regression line were estimated to be 5.37×10^3 K and -12.0, respectively. The optimal annealing temperature was 438 K. The temperature 503 K was found to be too high to maintain phase separation, *i.e.,* extreme temperatures led to homogeneous mixing.

Through DPD simulations, it was observed that systems with RR < 50% resulted in non-lamellar morphologies. The lamellar morphology was observed for RR values of at least 63%. Only slight improvements in the morphology were observed when RR was increased from 63% to 100%. Slight improvements to the morphology were also observed when temperature was increased from 373 K to 438 K. The simulations also showed that the lamellar morphology was only achievable with the diblock copolymer architecture. Simply mixing P3HT and PFTBT in a blend was not enough to achieve the lamellar morphology.

Despite the qualitative utility of our method, much improvement can be made for future work. The equilibration of MD cells can be extended with better computing resources. High temperature equilibration can also be applied. The accuracy of DPD simulations can also be improved by considering anisotropic rod-rod interactions found in conjugated polymers such as those used in PSC applications.

For my grandfathers, Pepito L. Macaraeg and Joee Y. Garcia.

Acknowledgements

First and foremost, I am indebted to my thesis advisor, Dr. Phillip Choi. I appreciate his patience and guidance throughout the development of this dissertation. I am forever grateful for everything he taught me in science, engineering, and life.

I would also like to thank Dr. Tian Tang and Dr. Gabriel Hanna for respectively teaching me statistical mechanics and molecular dynamics. Both were instrumental in the completion of this thesis.

I am also grateful to my past and present colleagues in the Choi research group. I would especially like to acknowledge Ali Reza Ashrafi Khajeh, Choon Ngan Teo, Dr. Diwen Zhou, Dr. Abolfazl Noorjahan, and Yang Zhou for all the assistance they provided.

Finally, I would like to thank my family for their love and support through all my years of education, both in the past and in the future. I would especially like to thank Kara N. M. Garcia, my sister, for her assistance in the preparation of several images in this dissertation.

CONTENTS

List of Tables

List of Figures

1 Introduction

Our world is in crisis. In 2011, the global population reached 7 billion, a figure that continues to increase at an alarming rate of 1 billion people every 12 years (1). Energy demand increases not only with the number of people in the world, but also with their quality of life. In 2050, it is estimated that global energy demand will be 70% higher than in 2011 (2). In addition to an ever increasing energy demand, our planet also faces the challenge of climate change. Not only do we need to secure our energy future but we also have to ensure that we do it in a sustainable manner.

Solar energy holds great potential. The energy our planet receives from one hour of sunlight exceeds the amount we use in a year (1). Unfortunately, we still have to realize this potential. Economic costs are the most often cited reason for the underutilization of solar energy. Compared to fossil fuels, photovoltaics are still prohibitively expensive. Devices based on crystalline silicon, which constitute 90% of all photovoltaic devices, are expensive not only because of the high costs of the material but also the processing technology used to manufacture them (3).

Polymer solar cells (PSCs) offer several advantages. The most important advantage is the lower cost of material and production. PSCs can be manufactured in a large-volume, solution-based process using roll-to-roll machinery, similar to printing newspapers (3). PSCs are also lighter and more flexible than silicon-based devices, enabling cheaper installations and applications on virtually any kind of surface.

Unfortunately, three major challenges continue to hinder the successful commercialization of PSCs. First is device efficiency. The efficiencies of silicon devices are around 20%. On the other

hand, the highest efficiency for an organic photovoltaic device is currently at 11% (4). Second is device stability. Commercial silicon solar cells can operate for 25 years whereas prototype PSCs can only operate for about a year (3). Third is process upscaling. The most efficient devices to date are fabricated through spin-coating, a process not fit for large-scale production. The challenge is to find the right combination of roll-to-roll processes to produce the most number of PSCs in the cheapest way possible (5). Although all three issues are critical to the successful commercialization of PSCs, the scope of this dissertation will be limited to addressing the challenge of improving device efficiencies.

Nothing affects the efficiency of a PSC device more than the active layer. The active layer is responsible for converting light energy into electrical energy. The active layer is composed of two chemical species: an electron donor and an electron acceptor. The morphology of the active layer greatly affects the efficiency of a PSC device. In the state of the art device, the donor and the acceptor molecules are mixed in the bulk forming interpenetrating networks. This morphology is called the bulk heterojunction (BHJ). Although the BHJ has significantly raised the efficiency of PSCs, its random formation poses a problem to charge collection. A lamellar morphology is ideal for device efficiency as it maintains the advantages of the BHJ and also enables better charge collection. The use of block copolymers is a promising strategy to achieve the lamellar morphology through molecular self-assembly. Unfortunately, determining which combination of polymers can form the lamellar structure requires countless experiments that take time and precious materials. Computational polymer science can reduce these laboratory costs by providing a guide to which polymer structures and combinations are most likely to succeed even before the first polymer is synthesized. In this dissertation, a multiscale modelling strategy is proposed to study PSC active layer morphologies. The strategy uses molecular dynamics (MD) to model the atomistic scale and

dissipative particle dynamics (DPD) to model the mesoscale. The Flory-Huggins interaction parameter (χ) between the model donor and model acceptor will be calculated using MD simulations. The χ parameter will then be used as input for the DPD simulations to predict the active layer morphology of the model donor and acceptor. This computational strategy will be tested with the active layer materials poly(3-hexylthiophene) (P3HT) as the electron donor and poly((9,9-dioctylfluorene)-2,7-diyl-alt-[4,7-bis(thiophen-5-yl)-2,1,3-benzothiadiazole]-2',2''-diyl) (PFTBT) as the electron acceptor. These materials were chosen as models for the study because they were reported to form the lamellar morphology by using the diblock copolymer architecture (6).

This dissertation will focus on the effect of P3HT regioregularity (RR) on the active layer morphology of the P3HT/PFTBT system. The percent RR is defined as the fraction of head-to-tail bonds in the polymer backbone, *i.e.,* it describes the orientation of side chains along the backbone. Although the optimal RR for BHJ systems has already been determined to be from 90% to 95% (7), no previous studies on the effect of RR in block copolymer systems have been reported. In addition to P3HT RR, this dissertation will also explore the effects of the annealing temperature and the effectiveness of the block copolymer strategy as predicted by the computational strategy proposed.

This dissertation is organized as follows. Chapter 2 justifies the need for solar energy. Chapter 3 presents background material on polymer solar cells. Chapter 4 introduces the fundamental theories behind the computational methods used in this dissertation. Chapter 5 presents the results of the computational studies. Results are then recapitulated in Chapter 6.

2 Solar energy

Before we delve into the subject of polymer solar cells, we must first understand our research motivation. We will begin by discussing the need for solar energy and its advantages over fossil fuels and other renewable energy sources. We will then explore the different solar technologies used in the world today. We will finish the chapter by discussing the various types of solar photovoltaic devices and how polymer solar cells fit in that picture.

2.1 Energy security, climate change, and renewable energy

Our species has come a long way from its rudimentary existence in the Stone Age. From our species' humble beginnings in Africa, we developed tools and ways of transport that allowed us to conquer all corners of the world. We developed agriculture to feed our growing populations. We developed medicine and sanitation systems that improved our health and increased our lifespan. Our species has been so successful in creating adaptive technologies that in just 200,000 years of existence, we have already stepped outside of our own atmosphere. Ironically, this same success could be the cause of our own demise. In 1927, there were only 2 billion people in the world; since 2011, there has been at least 7 billion: a 250% increase in just 84 years (1). Based on today's population growth of 1 billion every 12 years, there will be 9 billion people on the globe by 2035, and all of them need energy to live (1).

The world's energy demand will dramatically increase in the near future. The International Energy Agency (IEA) projects a 70% increase in energy demand in 2050 compared to 2011 levels (2). This increase does not come solely from having more people in the world. Energy is necessary to improve one's quality of life. For instance, 20% of the global population still has no access to

electricity (8). We can expect this percentage to shrink in the future as developing nations improve their socioeconomic conditions, *i.e.,* energy demand will also increase as more people are lifted from poverty. Unfortunately, meeting this increased energy demand is not as simple as it seems. We have to solve it simultaneously with an equally pressing issue: climate change.

Climate change is one of the greatest challenges we have ever faced. Consequences of a changing climate include rising sea levels, displaced and disappearing flora and fauna, and extreme weather. Ironically, climate change is a direct product of our technological advancement. The International Panel on Climate Change (IPCC) concluded in its fourth assessment report that "most of the observed increase in global average temperature since the mid-20th century is very likely due to the observed increase in anthropogenic greenhouse gas concentrations" (9). Table 2.1 shows the sources of greenhouse gas emissions. As shown, 56.6% of all greenhouse gases are CO_2 emissions coming from our consumption of fossil fuels. Evidently, we need to reduce our emissions from fossil fuel use to address climate change. Table 2.2 shows the breakdown of energy sources for the world's total global energy supply in 2008. As shown, 85.1% of the world's energy comes from fossil fuels. We have a conundrum. We need to increase our energy production but at the same time reduce our emissions from fossil fuels. The most obvious strategy is to change our energy mix in favour of more renewable energy. Renewables hold promise in both providing energy security and mitigating climate change.

Table 2.1. Sources of greenhouse gas emissions (8)

Gas	Use	Share (%)
Carbon dioxide, CO_2	Fossil fuel consumption	56.6
Carbon dioxide, CO_2	Deforestation, decay of biomass	17.3
Carbon dioxide, CO_2	Other	2.8
Methane, CH_4	Agriculture, livestock raising, etc.	14.3
Nitrous oxide, N_2O	Agriculture	7.9
Chlorofluorocarbons, CFC	Refrigeration, packing, etc.	1.1

Table 2.2. The source distribution of the global energy supply in 2008 (8)

Source	Share (%)
Fossil Fuels	85.1
Oil	34.6
Coal	28.4
Gas	22.1
Renewables	12.9
Bioenergy	10.2
Hydropower	2.3
Wind	0.2
Direct Solar	0.1
Geothermal	0.1
Ocean Energy	0.002
Nuclear	2.0

Renewables hold great potential in securing our energy future. This may not seem obvious at first. Compared to renewables, fossil fuels are more convenient for transportation and storage. There are also ample fossil fuel reserves for the near future. Based on our current energy use, there are still 46, 58, and 150 years of proven reserves for oil, gas, and coal, respectively (10). Theoretically, this means we can meet all our energy needs up to the year 2269 with only fossil fuels. Unfortunately, access to these proven reserves will not be as easy as in the past. Unconventional technologies will be necessary, and these technologies will have higher costs (10). Some examples of these technologies include the extraction and processing of heavy oil from the Alberta oil sands and drilling for oil in the Arctic. On the other hand, the total amount of energy that the earth receives in a single year is equivalent to 6000 years of our current consumption (10). Remember that most forms of renewable energy are actually derived from the sun: solar, wind, bioenergy, hydropower, and ocean energy (geothermal energy is the only renewable energy not derived from the sun). In short, although fossil fuels can provide enough reserves up to the year 2269, renewables can provide the same amount of energy up to the year 8015, with only one year of sunlight.

Renewables can also contribute significantly to reducing greenhouse gas emissions. The International Energy Agency (IEA) projects three different scenarios for 2050. The 6DS, 4DS, and 2DS scenarios predict that global average temperatures will increase by 6°C, 4°C, and 2°C above pre-industrial levels, respectively (2). The 6DS scenario is based on the present state of the world. The 4DS scenario is based on the assumption that governments will follow their stated intentions of cutting emissions and boosting energy efficiency. The 2DS scenario is based on the most optimistic assumptions that the world will have developed a sustainable energy system and that together with other strategies, emissions will have been reduced by more than 50% compared to

2011 levels (2). There is international consensus that to avoid the most severe effects of climate change, the global average temperature must not increase more than 2°C compared to pre-industrial levels (8). In short, our world is currently on track to the 6DS scenario whereas our goal is the 2DS scenario. According to the IEA, 30% of emission reductions from the 6DS to the 2DS scenarios will come from the use of renewable energy. Other emission reductions will come from improving energy efficiencies (38%), deployment of carbon capture and storage (14%), and nuclear energy and fuel switching (18%) (2). It also makes sense to produce more renewable energy from an economic perspective. Moving from the 6DS to the 2DS scenario will require a global financial investment of 44 trillion USD which will result in 115 trillion USD of fuel savings, a total net gain of 71 trillion USD (2).

Increasing renewable energy's part in the global energy mix can simultaneously solve our need for both energy security and reduced greenhouse gas emissions. However, changing the global energy mix is easier said than done. There needs to be contributions from both scientists and government policymakers. This dissertation aims to contribute to this global effort by advancing solar photovoltaic technology.

2.2 Advantages of solar energy

Solar energy holds the most potential among all forms of renewable energy. Table 2.3 reports the maximum and minimum technical potential of all forms of renewable energy according to the IPCC (8). The IPCC gathered data from many different studies that estimated the technical potential of each energy source. Note that technical potential is a much more useful estimate than absolute potential. Technical potential estimates consider factors that would limit our ability to

capture 100% of the energy offered by a specific source whereas absolute potential simply assumes all energy capture and conversion are 100% efficient. For example, in the case of solar energy, instead of taking into account all the energy the earth receives from the sun, technical potential estimates would only consider the energy received on terrestrial areas where installation of solar devices is feasible. The large differences between the maximum and minimum potentials reported in Table 2.3 for the same energy source are caused by the uncertainties of these limiting assumptions. For reference, note that the global primary energy supply in 2008 was 492 EJ (8). As shown, solar energy's capacity to provide our energy needs is way above the capacity of other forms of renewable energy. In fact, the minimum potential of solar is still greater than the maximum potential of geothermal, the second largest renewable resource.

Table 2.3 Technical potential of renewable energy (8)

Source	Max (EJ/yr)	Min (EJ/yr)
Solar	49837	1575
Geothermal	1421	128
Wind energy	580	85
Biomass	500	50
Ocean energy	331	7
Hydropower	52	50

Solar energy offers many other advantages aside from its astounding potential. First, solar energy is versatile. Technologies range from large on-grid power plants to small off-grid installations. The latter is very advantageous in powering remote areas where grid installations are still prohibitively expensive. For example, the poorest people in the world still use traditional biomass in cooking their food and providing light and heating for their homes. Burning traditional biomass, which

includes wood, charcoal, animal dung, and other agricultural wastes, has detrimental health effects and is the cause of 600,000 premature deaths each year in Sub-Saharan Africa (11). Second, extensive use of solar energy can reduce air pollution and save precious freshwater resources. Solar technologies produce fewer emissions than fossil fuels and solar technology cooling requirements are minimal, if any. Third, solar energy is not limited to terrestrial applications. In fact, solar photovoltaics were first used in space before they were functional on the earth's surface (10). Fourth, solar energy is available throughout the world and not limited to any geographical location, making solar energy less susceptible to market fluctuations. We can understand this better by looking at oil. Unlike solar energy, oil is found in concentrated deposits. As a result, the global supply of oil is controlled by only a handful of countries. This situation engenders oil price volatility, exemplified by the sharp oil price decline in the middle of 2014. The economy of Alberta, which relies heavily on the oil industry, was devastated. Such economic events can be better withstood with the incorporation of more solar energy in the Albertan economy. In fact, Alberta has good solar energy potential despite its distance from the equator. Table 2.4 ranks some of the major cities in the world in terms of yearly potential for solar photovoltaics. Canadian cities are highlighted in the table. Today, the most mature solar photovoltaic markets are Japan and Germany (12) whereas the fastest growing market is China (4). Note that four Canadian cities, including the Albertan cities of Calgary and Edmonton, hold greater potential than Beijing, China, Tokyo, Japan, and Berlin, Germany. The development of solar energy in China, Japan, and Germany should encourage all countries, not just the sunniest ones, to harness the untapped potential of solar energy.

Table 2.4 Ranking of major cities in terms of solar photovoltaic potential latitude tilt (12)

City	Yearly potential (kWh/kW)
Cairo, Egypt	1635
New Delhi, India	1523
Los Angeles, USA	1485
Regina, SK, Canada	1361
Sydney, Australia	1343
Calgary, AB, Canada	1292
Rome, Italy	1283
Winnipeg, MB, Canada	1277
Rio de Janeiro, Brazil	1253
Edmonton, AB, Canada	1245
Beijing, China	1148
Tokyo, Japan	885
Berlin, Germany	848

2.3 Forms of solar energy

There are four major ways to utilize solar energy: solar heat, solar thermal electricity, solar photovoltaics, and solar fuels. Solar heat currently provides the most solar energy contribution to the world energy mix (10). Solar heat involves the collection of solar radiation as heat and its utilization as heat. Solar heat technologies require collectors: materials with good thermal conductivity that transfer the thermal energy they gather to heat transfer fluids such as water and air. Commonly used collectors include flat-plate collectors, evacuated tube collectors, compound parabolic collectors, and solar ovens (10). Concentrating devices such as mirrors and lenses could be used to amplify the energy harnessed by these collectors. Parabolic troughs, Fresnel reflectors, parabolic dishes, Scheffler dishes, and solar towers include some of the most commonly used

11

techniques to concentrate solar power. Solar thermal electricity is simply an extension of solar heat technologies. Instead of the energy's utilization as heat, the thermal energy collected is used to turn water into steam which is then used to drive steam turbines for electricity generation. Unlike solar thermal electricity, solar photovoltaics generate electricity directly from light via the photoelectric effect. Solar photovoltaics will be discussed in more detail in the next section. Solar fuels are a derivative of solar heat and solar photovoltaics. There are three kinds of solar fuels: electrochemical, photo-chemical/ photo-biological, and thermo-chemical (8). Electrochemical solar fuel technologies use electricity from solar heat and solar photovoltaic technologies to produce hydrogen from water via hydrolysis. This strategy produces fewer emissions than steam-methane reforming, currently the most popular way of producing hydrogen. Photo-chemical and photo-biological solar fuel technologies use light energy to drive reactions that mimic photosynthesis. One popular example is artificial photosynthesis (13, 14). Much like natural photosynthesis, artificial photosynthesis uses carbon dioxide, water, and light energy to produce liquid carbon-based fuels. Thermo-chemical solar fuel technologies use the thermal energy from solar heat devices to drive endothermic reactions (8). The reactants for these endothermic reactions include water, carbon dioxide, coal, biomass, and methane; the products include hydrogen, syngas, methanol, dimethyl ether, and synthesis oil. In general, solar fuel technologies are still in the research and development phase. However, the eventual commercialization of solar fuels will be important in allowing solar energy to penetrate the transportation sector where liquid fuels with high energy density are the ideal energy source.

2.4 Solar photovoltaics

The story of solar photovoltaics (PVs) began in 1839 when Edmond Becquerel first observed the photoelectric effect on an electrode in an electrolyte solution (15). In 1877, Adams and Day observed the same phenomenon in the solid material selenium (15). The photoelectric effect was generally unexplained until Albert Einstein's miracle year of 1905. Einstein was awarded the Nobel Prize in Physics in 1921 for his explanation of the photoelectric effect. In the 1920's, Walter Snelling and Walter Schottky filed the first patents for solar cells (8). In 1954, Darryl Chapin, Calvin Fuller, and Gerald Pearson of Bell Labs invented single-crystal silicon solar cells with 6% efficiency for satellite applications (8, 15). In the same year, Reynolds reported 6% conversion efficiency for a cuprous sulfide/ cadmium sulfide heterojunction, the prototype for thin film solar cells (15). Elliot Berman adapted PV devices for terrestrial applications in the 1970s (8). Much progress has been made since then. In 2014, the world has installed a total PV capacity of 150 GW (4). Advancements in science and technology have also given rise to different types of solar cells beyond crystalline silicon solar cells and inorganic thin films. This section will introduce the different types of PV devices and also discuss their outlook for the future.

2.4.1 Crystalline silicon

Crystalline silicon (c-Si) devices comprised about 90% of the PV market in 2014 (4). There are two kinds of c-Si devices: monocrystalline and polycrystalline. Efficiencies for monocrystalline and polycrystalline range from 14% to 22% and from 12% to 19%, respectively (10). Monocrystalline solar cells have higher efficiencies because they are free of grain boundary defects that can slow down electrons and holes during device operation (16). Crystalline silicon devices are guaranteed 80% of their rated output for 25 to 30 years (10). Although they have the largest

market share and are the most mature solar PV technology, lots of improvements can still be made for c-Si devices. The major costs of these devices still come from the polysilicon feedstock (4). The most cost-effective cells are now at 5 g/W; thinner wafers are still possible and 3 g/W is achievable (4). Costs can also be reduced by producing devices with specialized resistance. For instance, solar cells made for Edmonton, Alberta would be fitted to operate under dry and cold conditions whereas solar cells made for Vancouver, British Columbia would be fitted to withstand a humid and rainy climate (4). Also note that reducing the amount of silver used in these devices is necessary: 5% of the c-Si module costs come from silver; in fact, 10% of the global demand for silver comes from the PV industry (10). Another technical challenge for c-Si devices is that their efficiencies decrease with higher temperatures (10). This is especially challenging for the proliferation of PV technology: places with hotter climates like the Middle East usually receive the most solar irradiation.

2.4.2 Inorganic thin films

To make thin films, inorganic semiconductor materials are sputtered on a glass or ceramic substrate instead of growing crystals (16). Inorganic thin films comprised 10% of the PV market in 2014, a disappointing loss in market share compared to 2009 when they comprised 16% of the market (4). Inorganic thin films can be classified into three types. The first type is amorphous silicon (a-Si) devices. Amorphous silicon is noncrystalline, *i.e.,* its atoms are not arranged in any order, impeding electron and hole motion through the material during operation. Amorphous silicon devices have efficiencies between 4% and 8% (10). Despite the low efficiencies and problems with degradation, these materials garnered attention due to their lower costs. Unfortunately, although the degradation problems have been solved by 2014, the difference in costs with c-Si devices has

become too small to justify any further development (4). The second type is Cadmium Telluride (CdTe) devices. CdTe devices are 11% efficient (10). First Solar, a leading company in CdTe production, aims for efficiencies of 25% in research devices and 19% in commercial devices with a degradation rate of 0.5% per year by 2017. The third type is copper-indium-gallium-(di) selenide (CIGS) devices. The efficiencies of CIGS devices range from 12% to 14% and research cells by the company Solar Frontier has exceeded 20% (4). Although CdTe and CIGS currently lag behind c-Si in terms of efficiency, they do offer several advantages in other areas. Unlike c-Si devices, CdTe and CIGS efficiencies do not decrease with an increase in cell temperature (10). They also reduce costs by using less material and reducing labor for wiring (16). As thin films, CdTe and CIGS devices also show great promise as building-integrated PV, *i.e.,* they are more easily installed on walls and windows whereas c-Si devices are limited to roof and ground installations.

2.4.3 Tandem cells

Tandem or multijunction cells are made by stacks of materials with varying bandgaps connected to each other by heterojunctions, similar in structure to a layered cake. The materials are arranged from top to bottom in decreasing bandgap. In this way, high-energy photons are first absorbed, leaving the lower-energy photons to be used by the bottom-most layer (16). Spectrolab achieved a 3-junction device efficiency of 38.8% and Sharp achieved a 44.4% with a concentrated radiation of 300 suns (4). Standard materials used for these devices are germanium (Ge), gallium arsenide (GaAs), and gallium indium phosphide (GaInP). Despite their high efficiencies, the high costs of these materials have limited the use of these devices to niche applications such as unmanned aerial vehicles and extraterrestrial devices (4). Tandem cells are also used for concentrating PV modules (CPVs). CPVs are made especially to capture sunlight normal to their surface. CPVs use mirrors

and lenses to focus sunlight into a small area of the tandem cells. CPV module efficiencies can reach 25% (10) but problems with cooling, light tracking, and series resistance have limited their use (16). As a result, these devices comprised less than 1% of the solar PV market in 2014 (4).

2.4.4 Dye-sensitized solar cells, organic PV, and quantum dots

The following PV devices are mostly in the research phase and will benefit from niche markets requiring "low-weight, transparency, flexibility, colour, and freedom of form" as PV device properties to facilitate their commercialization (4). Dye sensitized solar cells (DSSCs) consist of a "film of titanium dioxide coated with a monolayer of a charge-transfer dye to sensitize the film for light harvesting" (17). To complete the circuit, the titanium dioxide film is electrically connected to a counter electrode which is separated by an electrolyte solution. Sharp achieved the highest DSSC efficiency at 12% (4). Readers interested in more details about DSSCs should consult a comprehensive review by Hagfeldt *et al*. (18) Organic PV (OPVs) are similar in structure to inorganic PV devices. The defining factor for an OPV is its active layer; the active layer must contain at least one functional organic molecule. Mitsubishi Chemical achieved the highest OPV efficiency at 11.7% (4). The focus of this dissertation, polymer solar cells (PSCs), is one type of OPV. The reader should note, however, that in literature, the terms "PSC" and "OPV" are often treated synonymously. As their name suggests, at least one functional molecule in the device active layer must be a polymer. State of the art PSC devices use the polymer poly(3-hexylthiophene) and the fullerene derivative phenyl-C61-butyric acid methyl ester (PCBM) in their active layers. PSCs will be discussed in more detail in the next chapter. Quantum dots (QDs) are nanocrystalline semiconductors (16). QD PV devices take advantage of quantum confinement which allows their absorption properties to be adjusted at will, *i.e.,* one can specify what wavelength of light can be

absorbed by the device. Unfortunately, QD PVs are still in the early research phase. Readers interested in more details about QD PVs should consult the review by Kamat (19).

2.4.5 Cost reductions

Solar PV devices have become more affordable in the last 30 years. The IEA outlines the cost reduction in PV devices in its 2011 Solar Energy Perspectives report (10). From 1980 to 2001, PV devices showed a learning rate of 20% for modules and 12.5% for systems. The learning rate is defined as the resulting rate of cost reduction from the doubling of cumulative installed capacity. Major reasons for cost reduction during this time period include increases in manufacturing plant size and module efficiencies and decreases in the cost of purified silicon. From 2004 to 2007, a bottleneck in the production of purified silicon caused an increase in PV costs resulting in deviations from the learning rate. From 2007 to 2009, costs fell by 40%, returning to an average learning rate of 19.3% from 1976 to 2010. The PV industry has the highest learning rate in the energy sector which is very encouraging for the future of PVs.

2.4.6 Future outlook

The growth of the solar PV industry in the last several years has been astounding. The global PV capacity at the end of 2009 was only 23 GW; this number grew to 150 GW by 2014 (4). In fact, the whole world installed a total of 37 GW in the year 2013 alone, equivalent to a total investment of 96 B USD (4). It is also noteworthy that Asia deployed more than 50% of the solar capacity in 2013; leading the Asian installations were China and Japan with 11 GW and 7 GW, respectively (2, 4). Considering that the majority of the human population lives in Asia, these numbers are very encouraging. Assuming that the world reaches the 2DS scenario by installation of significant

amounts of renewables, the IEA credits 20% of emission reductions in the power sector to solar PV alone (2, 4). Considering the unprecedented growth of solar PV in the last decade and its undeniable potential for energy security and emissions reduction, there is no doubt that solar PV will play a big role in a sustainable human future.

3 Polymer solar cells

This chapter will serve as a general introduction to the field of polymer solar cells (PSCs). We will begin by outlining the benefits and challenges of PSCs. We will then focus our attention to the PSC active layer, the part of the PSC responsible for harnessing solar energy. We will then proceed with an overall picture of the PSC device, looking at its components in addition to the active layer. We will finish the chapter by looking at strategies to improve PSC device efficiencies.

3.1 Benefits and challenges

PSCs can help pave the way to low-cost solar energy. PSCs offer many cost reductions to the commercialized solar cells today (20). The most obvious source of savings is the cheaper cost of raw material. Traditional silicon cells require highly purified crystalline silicon and inorganic thin films need precious and scarce materials such as gallium, arsenic, indium, and selenium. On the other hand, the carbon-based PSC materials are more affordable and also more readily available. Another source of cost reduction is the solution-based processing of PSCs. PSCs can be manufactured in large volumes using roll-to-roll (R2R) coating, the same technique used to print newspapers (5). The R2R process is much cheaper than the fabrication steps used in making crystalline silicon devices. Crystalline silicon PV manufacturing requires high temperatures (~500-800°C) and vacuum deposition (15). The flexibility and light weight of PSCs also make them excellent candidates for building-integrated photovoltaics (BIPVs). "BIPV are photovoltaic materials that are used to replace conventional building materials in parts of the building envelopes, such as the roofs, skylights or facades (21)." BIPVs offer cost reduction in several ways (22). First, BIPVs do not require land resource allocation. Second, BIPVs reduce the overall costs of building materials because they serve functions of both structure and energy generation. Third, BIPVs do

not need mounting structures such as brackets and rails. All in all, the savings from raw material costs, processing costs, and the benefits of BIPVs have pushed many researchers into the field of PSCs in the last decade.

Unfortunately, PSCs still face several challenges before they can be successfully commercialized. PSCs still trail inorganic devices in terms of efficiency. Mitsubishi Chemical reported the highest device efficiency for an OPV at 11.7% using benzoporphyrin and a fullerene-derivative as active layer materials (23). It is worth noting that the device is an OPV but not a PSC. However, the fact that only the use of benzoporphyrin in the active layer precludes the device as a PSC justifies the comparison. On the other hand, crystalline silicon device efficiencies range from 14% to 22% (10). It must also be noted that the comparison between the two values of efficiency is not direct. The efficiency of the Mitsubishi device is already the best in the world and is only at the research and development phase whereas the range given for silicon devices includes many commercialized devices that were manufactured in an industrial scale. Another challenge for PSCs is device stability. Most commercialized solar cells are guaranteed 80% of their original efficiency for 25-30 years (10). Meanwhile, PSCs can only maintain their efficiencies for several thousand hours under favourable conditions (24). There are many factors that shorten device lifetimes, but there is a general consensus that the oxidation of the active layer by water and oxygen from the atmosphere is the most detrimental (25, 26). Another challenge for PSC commercialization is the upscaling of the production processes. Much of the laboratory devices used to advance the PSC field were fabricated using spin-coating. Unfortunately, spin-coating is not ideal for large volume production. Many R2R techniques are already available and applicable to the large volume production of PSCs. The challenge is determining the combination of R2R techniques that will result in the most efficient and cheapest industrial manufacturing of PSCs (5). Although all these

three challenges are important, discussions in this dissertation will be limited to improving device efficiencies. Consequently, device stability and process upscaling will not be covered in this chapter. Instead, the interested reader is directed to excellent references by Krebs on PSC stability (27) and manufacturing techniques (28).

3.2 The active layer

The active layer is responsible for absorbing light and converting it into electrical energy. One can argue that the active layer is the most important part of any PV device. After all, the active layer initiates the energy generation process. This section will serve as a general introduction to the PSC active layer. We will begin with the concept and development of polymer semiconductors. We will then introduce the most commonly used materials in PSC active layers and describe how the active layer converts light into electricity. We will finish this section by describing the evolution of the morphology of the active layer.

3.2.1 Semiconductors

Semiconductor materials are at the heart of the active layer. This is true for all kinds of solar cells, not just PSCs. Semiconductor properties are in between that of metals and insulators. To better explain this concept, it is customary to use the band theory of solids (29-31). For a single atom, electrons are allowed to occupy only a select number of energy levels as per quantum theory. When these atoms get close enough to each other, the orbitals of the outermost electrons interact and overlap. These interactions result in close but separate permissible energy levels. A large enough number of atoms arranged in a crystal lattice will result in a continuous band of energy, *i.e.,* the levels will be so close and numerous that they will form a continuous band. There are two kinds

of energy bands: the conduction band and the valence band. Electrons in the valence band are still bound to their respective atomic nuclei. On the other hand, the electrons in the conduction band are free to move within the crystal. Figure 3.1 illustrates the conduction and valence bands for conductors, semiconductors, and insulators. Two scenarios exist for conductors: the conduction band is either partially filled with electrons (e.g., copper) or the conduction band actually overlaps with the valence band (e.g., zinc) (29). These band structures allow electrons to move freely since the occupied energy levels are very close to the higher unoccupied levels. For semiconductors (e.g., silicon) and insulators (e.g., glass), there is a clear separation between the conduction and valence bands. This separation is commonly known as the "bandgap." Electrons require additional kinetic energy in order to clear the bandgap and move from the valence band into the conduction band. As shown in Figure 3.1, the only real difference between a semiconductor and an insulator is the size of their respective bandgaps. Semiconductor bandgaps are around 1 eV whereas insulator bandgaps are larger than 9 eV. This difference in bandgaps results in another distinction between semiconductors and insulators. Insulators have "filled" valence bands and "empty" conduction bands whereas semiconductors have "almost-filled" valence bands and "almost-empty" conduction bands. This distinction arises because thermal energy can push some electrons in the valence band of the semiconductor to its conduction band. On the other hand, the large bandgap for insulators precludes any transfer effected by thermal energy, *i.e.,* thermal energy is not enough to overcome the large bandgap. In fact, at absolute zero (*i.e.,* 0 K), the valence and conduction bands of semiconductors would be indistinguishable from those of insulators. Electrons can also gain kinetic energy from the absorption of photons. Charge carriers can be generated when photons carrying sufficient energy give electrons the required energy to jump the bandgap, moving them from the valence band to the conduction band. This is also known as the photoelectric effect.

Visible light does not have enough energy to overcome the insulator bandgap; the semiconductor bandgap, however, is small enough to allow photon absorption, making semiconductors ideal solar cell materials.
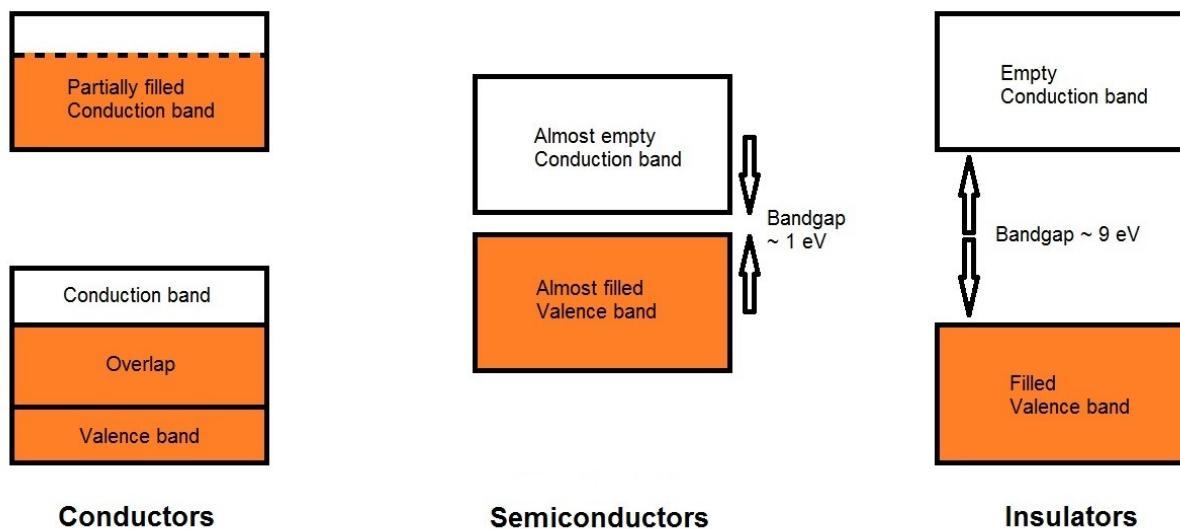
Figure 3.1 Electronic band diagrams for conductors, semiconductors, and insulators

3.2.2 Molecular orbitals

Band theory applies well to materials that form crystal structures. Most organic molecules, however, do not form crystals. Because their intermolecular forces are not strong enough, electronic energy levels in organic molecules stay separate and do not form continuous bands (32). For organic molecules, molecular orbital (MO) theory is more applicable. Qualitative MO theory was developed by Fukui, Hoffmann, and Woodward for which Fukui and Hoffmann were awarded the Nobel Prize in Chemistry in 1981 (33). Discussion of MO theory will be limited to parts that are most important to active layer materials. Detailed treatment of MO theory can be found in most

organic chemistry textbooks (34, 35). MO theory is in fact very similar to band theory: when atoms are covalently bonded, their individual atomic orbitals interact and combine to form MOs. Figure 3.2 shows the linear combinations of atomic orbitals. Two s-orbitals combine to form a σ MO and two p-orbitals combine to form a π MO. Electrons found in MOs no longer belong to a specific atom; instead, they are delocalized to the volume covered by their respective MOs.
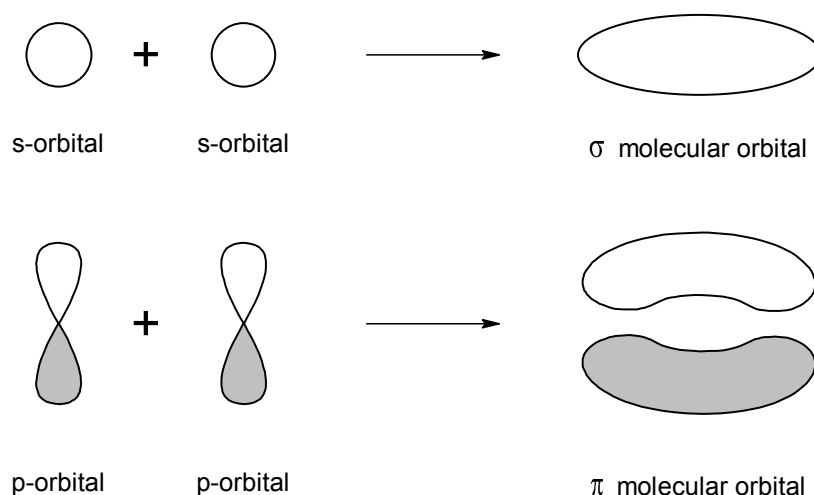
Figure 3.2 Constructive linear combinations of atomic orbitals into molecular orbitals

In reality, the linear combination of atomic orbitals is more complicated than is shown in Figure 3.2. To better explain the formation of MOs, it is customary to study the p-orbitals of 1,3-butadiene as shown in Figure 3.3. The number of orbitals is always conserved, *i.e.,* the addition of two p-orbitals should result to two MOs. In the case of 1,3-butadiene, there are four p-orbitals adjacent to each other. As expected, these four p-orbitals combine to form four MOs. The number of orbitals is conserved because there are two ways to combine the wave functions of p-orbitals: constructive and destructive interference. Constructive interference results into bonding MOs as shown in

Figure 3.2. Destructive interference, on the other hand, results into antibonding MOs. In the ground state, bonding MOs usually contain two electrons whereas antibonding MOs contain no electrons. Although they do not hold electrons in the ground state, antibonding MOs are still important, especially in the excited states of the molecules, *i.e.,* when molecules absorb energy. It is customary to mark the lobes of p-orbitals differently to indicate the phase of the wave function at the particular volume of space covered by the lobe. The combination of lobes with the same phases results in constructive interference whereas the combination of lobes with opposite phases produces destructive interference. Destructive interference also produces nodal planes. As shown in the figure, energy increases with the number of nodal planes. Although the case of 1,3-butadiene only shows the combination of four p-orbitals, it is not difficult to extend the concept to a large number of orbitals. For any number of orbitals combined, two MOs always stand out in terms of reactivity. These are the frontier orbitals: the highest occupied molecular orbital (HOMO) and the lowest unoccupied molecular orbital (LUMO). The HOMO contains the most weakly held electrons, justifying why HOMO electrons are the ones donated in reactions. On the other hand, the LUMO is the lowest energy orbital available to accept electrons. If molecules absorb enough energy to cover the LUMO-HOMO difference, electrons from the HOMO jump into the LUMO. This process is similar to the transition of electrons from the valence band to the conduction band as shown for Figure 3.1. It probably is not surprising to the reader that the energy difference between the LUMO and the HOMO is called the "bandgap" of the molecule.

Highest Unoccupied
Molecular Orbital

3 nodal planes
0 electrons

Lowest Unoccupied
Molecular Orbital
(LUMO)

2 nodal planes
0 electrons

$\Delta E = \text{Bandgap}$

Highest Occupied
Molecular Orbital
(HOMO)

1 nodal plane
2 electrons

$H_2C = \overset{}{\underset{}{}} = CH_2$

Lowest Occupied
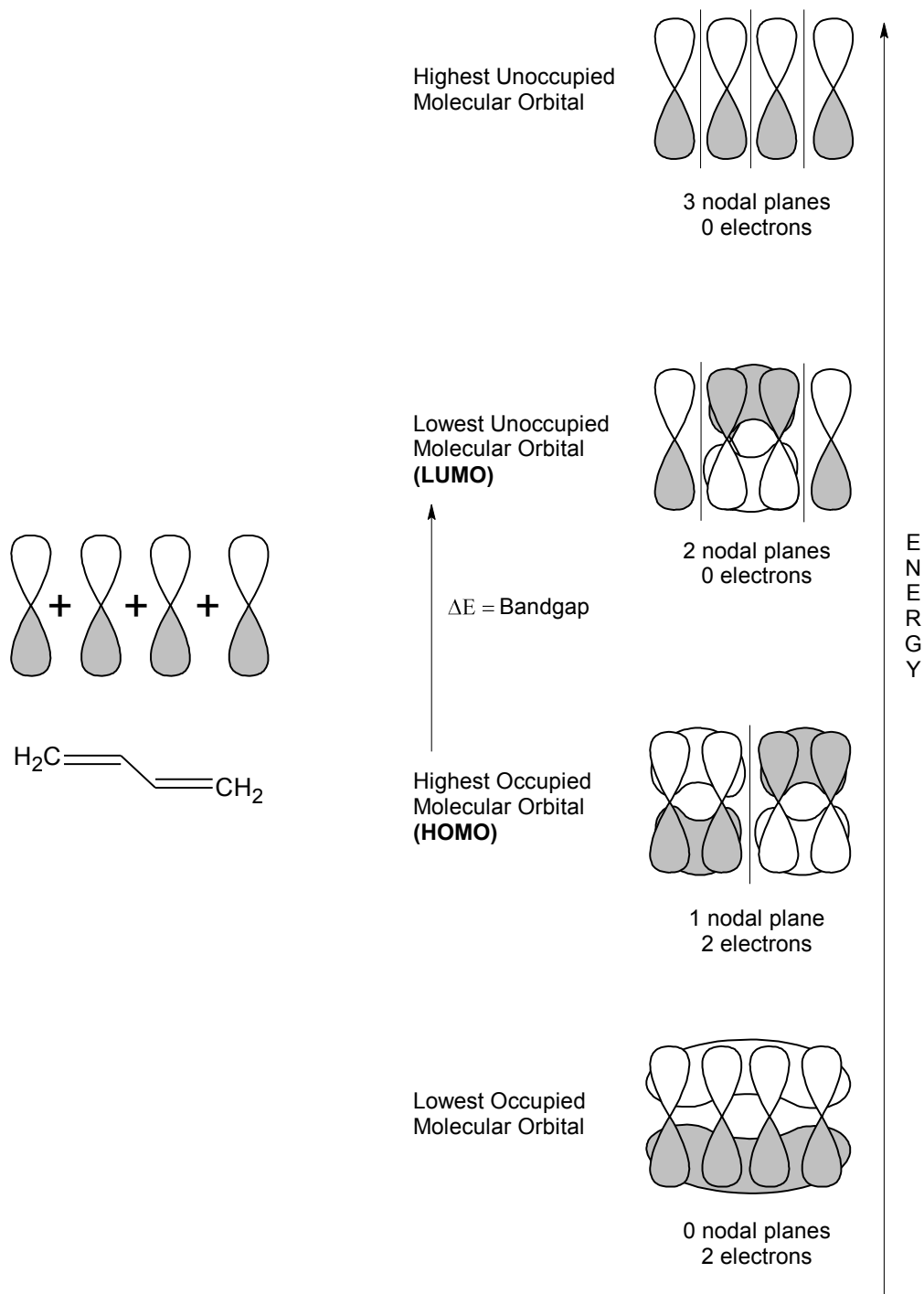Molecular Orbital

0 nodal planes
2 electrons

ENERGY

Figure 3.3 Molecular π-orbitals of 1,3-butadiene

3.2.3 Fundamental steps in energy conversion

There are four steps in the conversion of light into electricity. Figure 3.4 illustrates these four steps. The first step is exciton generation. When a photon is absorbed, the energy is used to promote an electron from the donor's HOMO to its LUMO. This process leaves a positively charged hole in the donor's HOMO. For inorganic semiconductors, the electron and hole are free charge carriers. This is not the case for organic semiconductors: due to their low dielectric constant and the localized electron and hole wave functions, the electron and hole remain bound to each other (36). This bound electron-hole pair is called an "exciton." The binding energy of an exciton ranges from 0.1 to 1.4 eV (37). The second step is exciton diffusion. The exciton travels to the interface of the donor and the acceptor. However, the exciton can only travel a maximum distance before the electron and the hole recombine. This maximum distance is called the "exciton diffusion length." Several studies measured the exciton diffusion lengths of poly(p-phenylene vinylene) (PPV), poly(3-hexylthiophene) (P3HT), and some low bandgap polymers to be all below 10 nm (38-41). The implications of the exciton diffusion length on the active layer morphology will be discussed in section 3.2.5. The third step is exciton dissociation. In order for the exciton to dissociate, the difference between the acceptor's LUMO and the donor's HOMO must be less than the potential difference between the electron and the hole, as shown in Figure 3.4. This requirement allows the exciton dissociation to be an energetically favourable process. After dissociation, the electron and the hole, although no longer bound excitons, still need to overcome their mutual Coulombic attraction before they can proceed to charge collection (42). Note that the electron and hole are commonly referred to as "geminate pairs" at this point in the process. The fourth step is charge collection. The electrons and holes are collected at their respective electrodes. There are two carrier transport mechanisms: drift current and diffusion current (36). Drift current is the motion of the

charge carriers along the potential gradient determined by the choice of the electrode materials. When an external bias is applied to the device, the charge carriers follow the resulting internal electric field to their respective electrodes. On the other hand, the diffusion current relies on the concentration gradient of the charge carriers. Since the excitons dissociate at the donor-acceptor interface, there will always be a high concentration of charge carriers at this same location, forcing the electrons and holes to move away from the interface. The drift current dominates when the internal electric field is large whereas the diffusion current dominates when the internal electric field is small.
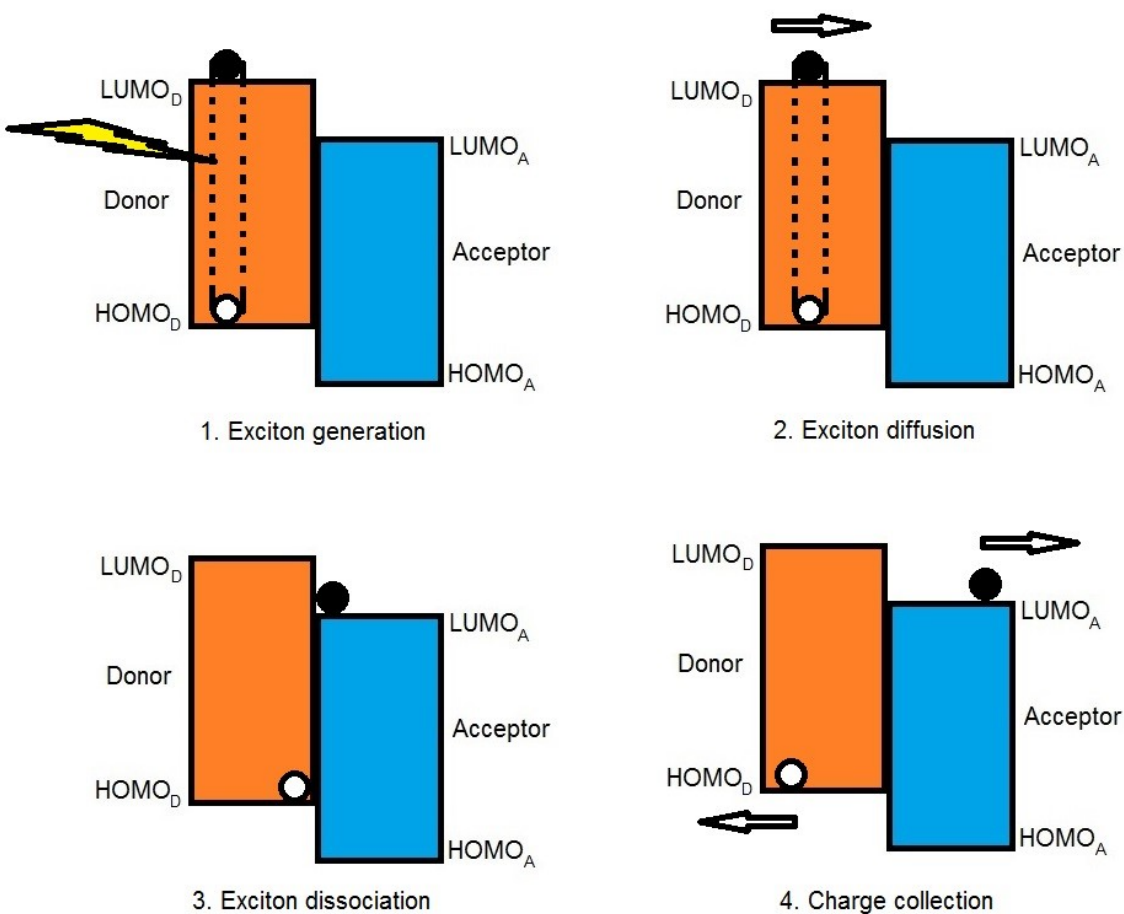

Figure 3.4 Fundamental steps in energy conversion

28

3.2.4 Active layer materials

To be considered as a PSC device, the active layer must contain at least one functional polymer. For a layperson, this may sound ludicrous. After all, polymers are known for being excellent insulators. What business do polymers have in the active layer of a solar cell? It was only recently that scientists themselves discovered that polymers can be made to conduct electricity. In 1977, Shirakawa, Heeger, and McDiarmid discovered that polyacetylene's conductivity can be increased from that of an insulator to a level comparable to actual metals, a discovery that earned them the Nobel Prize in Chemistry in 2000 (43, 44). Figure 3.5 shows the structure of polyacetylene. Their contributions led to an explosion of research activity on π-conjugated polymers, or simply "conjugated polymers." By definition, a conjugated molecule has alternating single and multiple bonds within its molecular structure. For example, benzene and 1,3-butadiene would be considered conjugated molecules. Conjugated polymers, on the other hand, are only required to have conjugated backbones like polyacetylene, *i.e.,* alternating single and double bonds in their backbone structure. Conjugated polymers do not need to have conjugated side-chains. Conjugated polymers are special because their electrons are delocalized along their backbones. This is a result of the interactions of adjacent and parallel p-orbitals, giving the molecule increased stability and unique electronic properties. The polymer backbone atoms need to be on the same plane to keep the p-orbitals parallel to each other. In reality, conjugated polymers have finite conjugation length, *i.e.,* electron delocalization along the backbone is limited. This is expected as polymers are large chain molecules and the chances of whole backbones being on one plane are very slim.
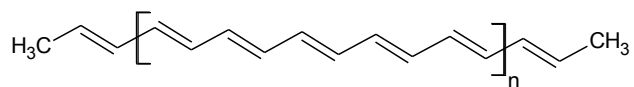
Figure 3.5. Polyacetylene

PSC active layers comprise at least two chemical species: an electron donor (material of low electron affinity) and an electron acceptor (material of high electron affinity). Distinguishing an electron donor from an electron acceptor by visual inspection is not straightforward, especially for large molecules. Experimental photoelectron techniques and density functional theory (DFT) calculations are often used to determine a particular molecule's electron affinity (45). Of course, a well-trained chemist or physicist in the field can develop an intuitive sense as to which structures can be used as electron donors or acceptors. For example, fullerene structures are always used as electron acceptors. Aside from electron affinity, donors and acceptors also need to exhibit relatively higher hole and electron mobilities, respectively. Finding viable donor-acceptor matches requires even more work. First, the energy levels of the frontier orbitals (*i.e.,* HOMO and LUMO) of the donor and acceptor need to match in a certain way. Second, as will be discussed in Section 3.2.5, the donor and acceptor molecules need to form nanoscale domains when mixed with each other. Another important requirement is that at least one of these molecules (usually the donor) has an electronic bandgap that matches the solar spectrum in order to absorb the maximum amount of solar energy.

Conjugated polymers are often used as electron donors. Figure 3.6 shows the molecular structures of commonly used electron donors. The development of conjugated polymers as PSC electron donors can be divided into three phases (46). The derivatives of poly(p-phenylene vinylene) (PPV) which include poly[2-methoxy-5-(2'-ethylhexyloxy)-1,4-phenylenevinylene] (MEH-PPV) and

30

poly[2-methoxy-5-(3',7'-dimethyloctyloxy)-1,4-phenylenevinylene] (MDMO-PPV) constitute the first phase. Although PPV-based devices were able to deliver efficiencies as high as 2.5% (47), the large bandgap of these polymers limited the maximum efficiencies achievable. The solar spectrum's maximum photon flux lies in the vicinity of 1.8 eV whereas PPV-derivatives have bandgaps in the range of 2.0 to 2.2 eV (48), *i.e.,* any photons with less energy than 2.0 eV would have not been absorbed by a PPV-based device. This led to the second phase of electron donor development which centred on poly(3-hexylthiophene) (P3HT), a conjugated polymer with a bandgap of 1.9 eV (46). P3HT's higher crystallinity and π-π stacking led to higher hole mobility, and thus to more efficient devices. In addition, the processability and active layer morphology of P3HT devices are also excellent. Despite P3HT's relative success as an electron donor, it still has shortcomings that the third phase of electron donor development aims to address. P3HT's most obvious shortcoming is its bandgap. Although it was an improvement on PPV-based devices, P3HT still wastes a significant amount of the solar spectrum. For comparison, note that the bandgap of silicon at 300 K is 1.11 eV (49). Many researchers have suggested different polymer structures with lower bandgaps to maximize the absorption of the solar spectrum (48, 50-54). Unfortunately, this third phase is still ongoing and no clear frontrunner has been identified.
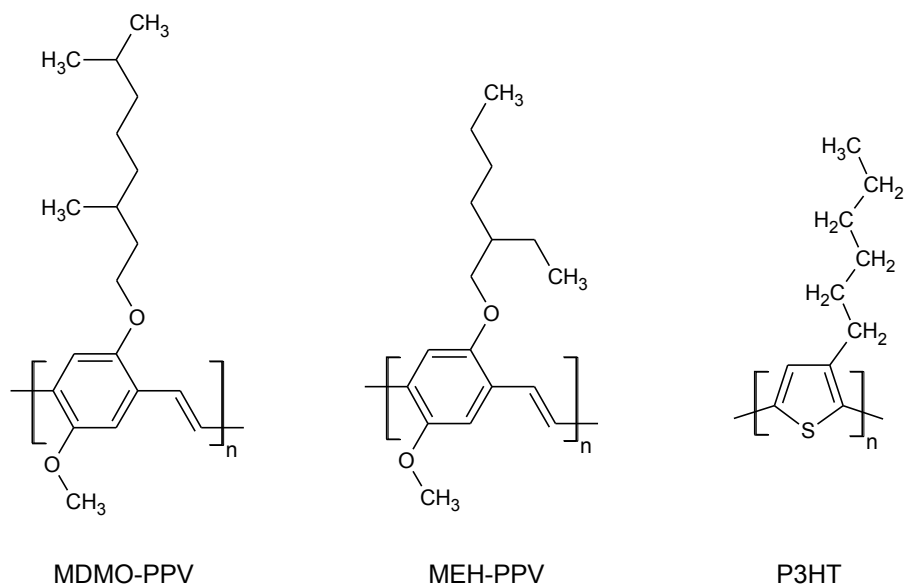
Figure 3.6 Commonly used electron donors

Fullerene materials are the most popular electron acceptors for PSCs due to their high electron mobilities, high electron affinity, and good processability (54). Fullerenes were named after the famous architect Buckminster Fuller whose geodesic domes shared a similar shape. Figure 3.7 shows the molecular structures of C_{60} (fullerene) and phenyl-C_{61}-butyric acid methyl ester (PCBM). Curl, Kroto, and Smalley were awarded the Nobel Prize in Chemistry in 1996 for their discovery of fullerenes. Sariciftci and co-workers were the first to demonstrate photoinduced charge transfer from a conjugated electron donor (MEH-PPV) to C_{60} (55). Despite the efficient charge transfer, making devices based on conjugated polymers and C_{60} were found to be problematic. Conjugated polymers and C_{60} are incompatible and tend to phase separate. To solve this problem, C_{60} was functionalized to improve its solubility with conjugated polymers, resulting into PCBM (56, 57). To date, PCBM remains as the preferred organic electron acceptor. Although new electron acceptors, both fullerene derivatives and conjugated polymers, have been reported (58-61), there is still no consensus on the best substitute for PCBM as the organic electron acceptor.

Note that inorganic electron acceptors have also been paired with organic electron donors (54); however, they will not be discussed in detail as they are outside the scope of this dissertation.
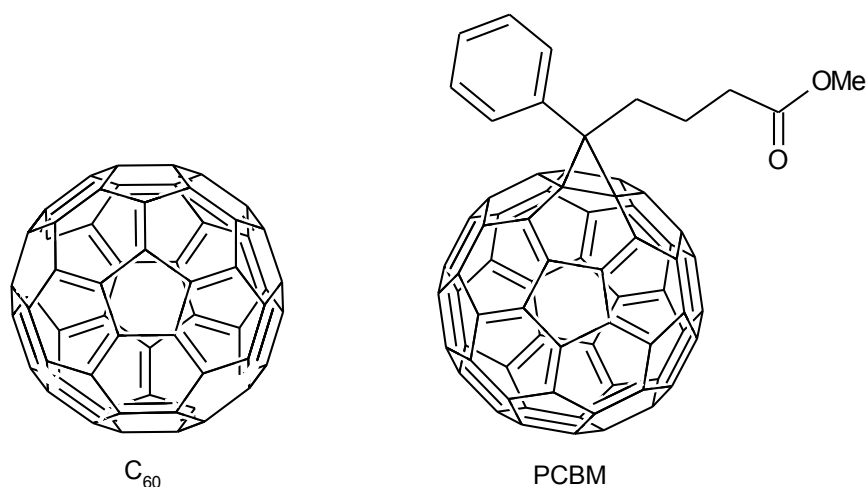
Figure 3.7 Commonly used electron acceptors

3.2.5 Morphology

The active layer morphology is a large determining factor of device efficiencies. Figure 3.8 illustrates the different active layer morphologies. The first devices were based on the single layer morphology. Excitons were generated in the active layer but exciton dissociation occurred in the interfaces between the active layer and the electrodes (3). The inefficient exciton dissociation at the electrode interface limited the success of this morphology. Exciton dissociation was greatly improved with the introduction of the bilayer heterojunction by Tang in 1986 (62). The bilayer heterojunction introduced the concept of using electron donors and acceptors in the active layer. Also note how the bilayer heterojunction mimics the p-n junction used in silicon solar cells. Despite improvements from the single layer morphology, efficiencies were still limited for bilayer devices. The biggest challenge comes from the short exciton diffusion lengths of conjugated

33

polymers. Remember that excitons can only dissociate efficiently at the donor-acceptor interface. Any exciton generated at a point that is more than 10 nm away (maximum exciton diffusion length) (38-41) from a donor-acceptor interface will recombine before dissociation, effectively wasting the energy used to generate the exciton in the first place. This challenge implies that the bilayer structure can only be, at most, 20 nm thick (10 nm each for the donor and the acceptor phase assuming both phases can absorb visible light). The high absorption coefficients of organic molecules are not enough to compensate for this limitation on the active layer thickness. An extremely thin active layer would capture an insignificant amount of sunlight. In short, a bilayer device cannot be made too thick or too thin. Another shortcoming of the bilayer structure is its limited interfacial area. The interfacial area between the donor and the acceptor phases is limited by the cross sectional area of the device, thereby limiting the chances of exciton dissociation. To overcome these problems, Yu and coworkers introduced the bulk heterojunction (BHJ) in 1995 (63). The BHJ is an interpenetrating network of donor and acceptor phases as shown in Figure 3.8. BHJ morphologies with phase domains around 10-20 nm allow excitons to reach a donor-acceptor interface in active layers as thick as 100-200 nm, enough thickness to capture the majority of incident photons (64). To date, the BHJ morphology remains as the standard for PSC devices. Nonetheless, the BHJ morphology is not perfect. The formation of the BHJ morphology is largely unpredictable: cul-de-sacs and dead-ends can be introduced for either phase as shown in Figure 3.8. This random structure is problematic as charge carriers (electrons or holes) can be trapped within one phase if there is no clear path to their respective electrodes. Many researchers have been working to improve the BHJ morphology over the last two decades (37, 65-70). The goal is to achieve an ordered lamellar structure shown in Figure 3.8. Notice that with a lamellar structure, the advantages of the BHJ morphology are preserved. In addition, the tortuous pathways towards

the electrodes are eliminated. Several strategies have been explored to move the BHJ morphology towards the ideal lamellar morphology. These strategies are molecular design and processing techniques. Molecular design involves the development of donor and acceptor chemical structures that match and mix just enough to form the ideal morphologies. The use of donor-acceptor block copolymers is a promising strategy that takes advantage of the self-assembling properties of this class of materials (71). Processing techniques include thermal annealing, solvent annealing, and the use of chemical additives during the manufacturing of the PSC device. These strategies will be discussed in more detail in Section 3.4.2.
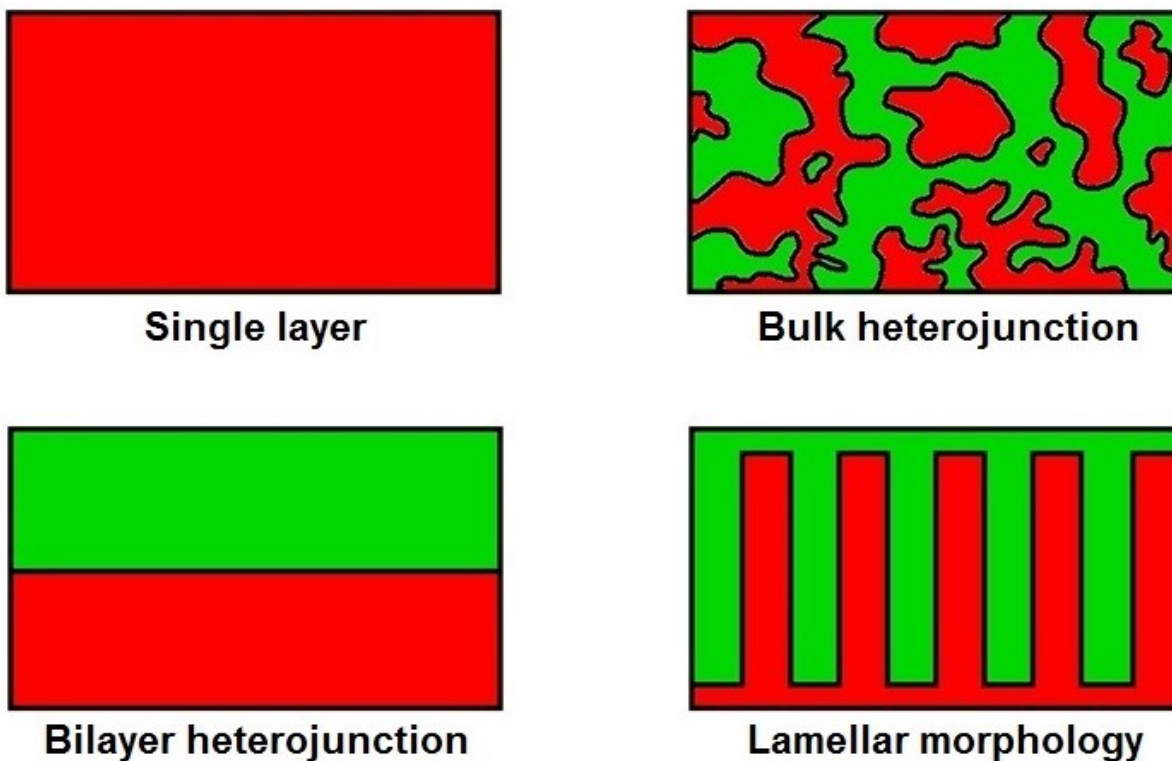

Figure 3.8 Active layer morphologies

35

3.3 Device architecture

Although the active layer is the most important part of a PSC device, it cannot deliver energy by itself. The PSC device is composed of different layers stacked on top of each other, each serving invaluable functions. Figure 3.9 shows the general schematic of a PSC device. The active layer is found in the middle of the device. Sandwiching the active layer are the two electrode buffer layers, one for the metal electrode and another for the transparent electrode. The buffer layers facilitate charge collection. Although buffer layers improve device performance and stability, their inclusion is optional for basic operation, *i.e.,* the device would still work without them, albeit not very well. Electrodes, on the other hand, are vital to sweeping out the charge carriers from the active layer and delivering electricity to an external load. The substrate is another important part of the device. The substrate protects the device from outside elements and also serves as the base component during the manufacturing of the device. By convention, the side of the substrate is considered the "front" of the device (72). In the case of frontside illumination as shown in Figure 3.9, it is necessary for the substrate to be optically transparent. Though uncommon, backside-illuminated devices are also feasible (72). A backside-illuminated device would not require a transparent substrate, however, at least one electrode and its buffer layer would still need to be transparent. Most research devices in the last decade were designed for frontside illumination. The convention for frontside illuminated devices will be followed for the rest of this dissertation.

Frontside illumination

Substrate
Transparent electrode
Buffer layer (transparent electrode)
Active layer
Buffer layer (metal electrode)
Metal electrode
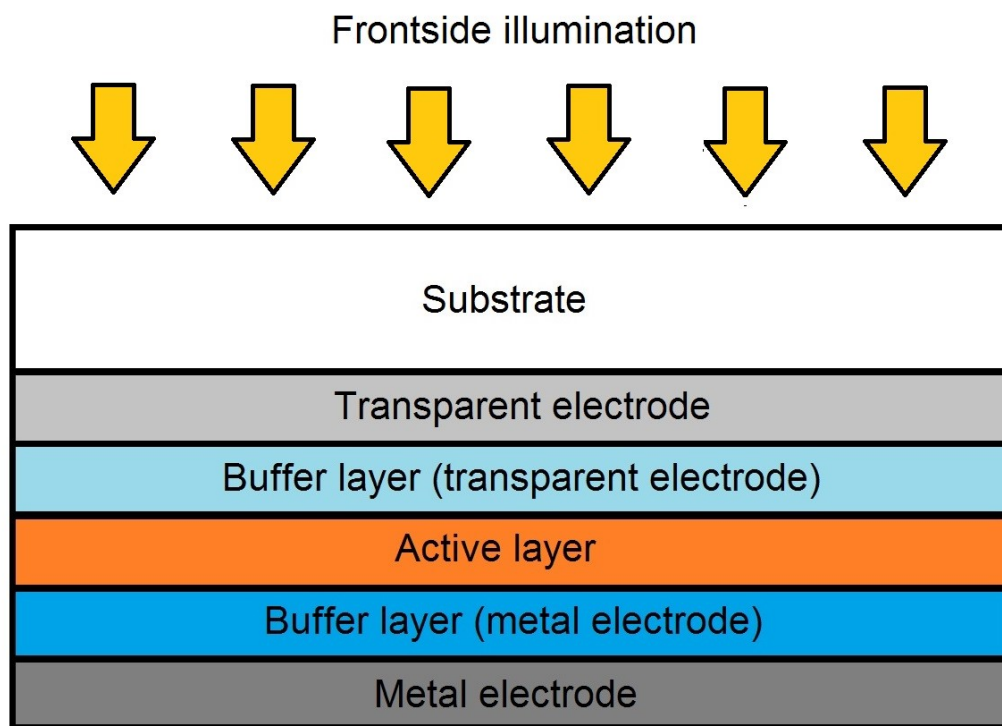
Figure 3.9 General PSC device architecture

3.3.1 Device geometries

In literature, there are two predominant device geometries: normal and inverted. Figure 3.10 shows

the makeup of these two geometries. To further facilitate comparison, Table 3.1 lists representative

materials for each geometry. By convention of the PSC field, the negative charge carriers

(electrons) are collected in the negative electrode (cathode) whereas the positive charge carriers

(holes) are collected in the positive electrode (anode) (72). This flow description is followed in

both the normal and inverted device geometries as shown in Figure 3.10. Structurally, the only

difference between the two geometries lies in the placement of the cathode and the anode. In the

normal geometry, the cathode is the metallic electrode located at the back of the device whereas

the anode is the transparent electrode adjacent to the substrate. In the inverted geometry, the anode

is the metallic electrode located at the back of the device whereas the cathode is the transparent electrode adjacent to the substrate. The convention on which geometry to designate as "normal" is arbitrary. Normal geometry devices have become the de facto standard for research cells due to their relatively higher efficiencies and ease of processing (72). Unfortunately, processing of normal geometry devices requires vacuum deposition which is not favourable for upscaling and device stability. On the other hand, inverted geometry devices can be made without vacuum deposition, albeit they are less efficient in energy generation (73). To minimize confusion, please assume the configuration of the normal geometry device hereafter unless otherwise noted, *i.e.,* assume the anode as the transparent electrode and the cathode as the metallic electrode.
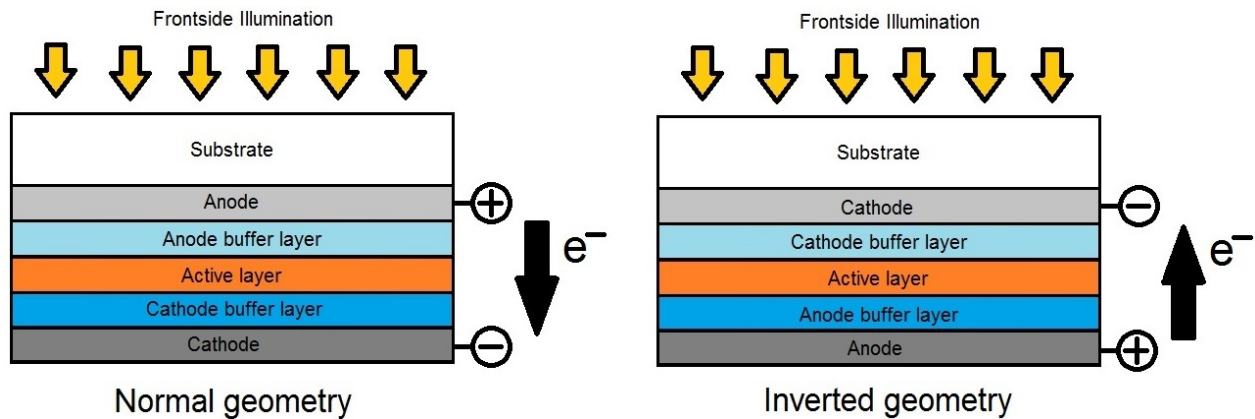

Figure 3.10 Normal and inverted device geometries

Table 3.1 Representative materials for normal and inverted devices (72)

Component	Normal	Inverted
Substrate	Glass or PET	Glass or PET
Transparent electrode	Indium tin oxide	Indium tin oxide
Buffer layer (transparent electrode)	PEDOT:PSS	Zinc oxide
Active layer	P3HT:PCBM	P3HT:PCBM
Buffer layer (metallic electrode)	Lithium fluoride	PEDOT:PSS
Metallic electrode	Aluminum	Silver
PET = Polyethylene terephthalate; PEDOT = Poly(3,4-ethylenedioxythiophene); PSS = Poly(styrenesulfonate); P3HT = Poly(3-hexylthiophene); PCBM = fullerene derivative [6,6] – phenyl C61 butyric acid methyl ester		

3.3.2 The substrate

The substrate plays two major roles: it acts as the base layer during device processing and it protects the device during operation. There are three classes of substrate materials: metal, polymer, and glass (74). Stainless steel is the most commonly used metal substrate owing to its high resistance to corrosion. Stainless steel substrates offer many advantages including high temperature resistance, dimensional stability, and excellent barrier properties against oxygen and water, the primary agents of the active layer's chemical degradation. Unfortunately, metallic substrates are limited to backside-illuminated devices due to being non-transparent. Metallic substrates also require polishing to smooth their rough surface. Rough surfaces can easily cause short circuits in thin films such as PSCs. For polymer substrates, polyethylene terephthalate (PET) and polyethylene naphthalate (PEN) are the usual choice. These substrates are favoured due to their optical transparency and compatibility with R2R processes, facilitating process upscaling. Polymer substrates also maintain the flexibility of the device. Unfortunately, polymer substrates

are more susceptible to mechanical and UV degradation. Most polymer substrates also have low glass transition temperatures, limiting the temperatures during processing. They also do no provide adequate barrier properties against oxygen and water. It is commonly accepted that additional encapsulation is necessary to allow polymer substrates to be feasible. On the other hand, one can say that glass substrates are the complete opposite of polymer substrates. Glass has excellent temperature resistance, chemical resistance, and barrier properties against oxygen and water. However, glass cannot be processed through R2R techniques and it also negates the flexibility of PSC devices. Since upscaling and flexibility do not become important until later in the technology development process, glass has been the most popular substrate material for research devices. Unfortunately, more work has to be done to find the ideal substrate material with great thermal stability, barrier properties, flexibility, and compatibility with process upscaling techniques.

3.3.3 The electrodes

The main function of the electrodes is to collect charge carriers (electrons and holes) and deliver them to an external load. In addition to their electrical properties, electrodes also need to meet several other requirements in order to function well in a PSC device. As mentioned before, at least one of the electrodes must be optically transparent. Finding an electrode material that meets both the electrical and optical requirements is actually quite challenging. In fact, reducing the sheet resistance of a material often means sacrificing its optical transmittance (75). Electrodes also need to be chemically stable. Some electrode materials can degrade over time and migrate into other parts of the device. This migration can be especially problematic as they can cause direct damage to the active layer. Electrodes also require mechanical properties such as flexibility and good adhesion to their adjacent layers to prevent device delamination. In addition to processability,

electrodes also need to be affordable. In fact, the electrode can make up to 50% of the cost of a PSC device (75). To date, there is still no perfect electrode material with all these required properties. The most commonly used materials for electrodes prioritize electrical and optical properties. For transparent electrodes, indium tin oxide (ITO) is the most popular material used. ITO has good conductivity and good optical transmittance. The main drawbacks of ITO are its costs and its poor flexibility. A cheaper and more flexible alternative to ITO is the conductive polymer blend PEDOT:PSS. However, the poor conductivity of PEDOT:PSS limits its use as the transparent buffer layer, as will be discussed in the next section. For non-transparent electrodes, aluminum is the material of choice due to its abundance and the fact that its work function matches the LUMO of most acceptor materials (76). Like ITO, aluminum is not perfect. Aluminum is known to allow atmospheric water and oxygen to pass through and attack the PSC active layer (77). Aluminum itself can also react with the organic molecules in the active layer (78). To fix the shortcomings of electrodes, buffer layers are introduced between them and the active layer. Buffer layers not only work to improve efficiency but they can also significantly improve device stability.

3.3.4 The buffer layers

The electrode buffer layers serve many functions, but none as important as improving charge transport from the active layer to the electrodes. As there are two electrodes, there are also two types of buffer layers. The cathode buffer layer (CBL) is also known as the electron transport layer or equivalently as the hole blocking layer. The anode buffer layer (ABL) is also known as the hole transport layer or equivalently as the electron blocking layer. As their names suggest, the buffer layers improve the selectivity of the cathode to electrons and the anode to holes. Selectivity is improved through proper energy alignment among the different components of a PSC device.

Figure 3.11 shows the ideal energy alignment between the active layer materials, the buffer layers, and the electrodes. In a similar fashion to Figure 3.4, the top and bottom edges of the rectangles shown in Figure 3.11 represent the LUMO and the HOMO of the materials, respectively. Remember that electron energy increases from bottom to top, *i.e.,* the LUMO has a higher electron energy than the HOMO. Thus, it is energetically favourable for the electron to move down the diagram whereas the opposite tendency is true for the hole. Note how the ABL LUMO acts as a barrier for electrons to move into the anode. The CBL HOMO serves the same purpose for holes (remember that for BHJ active layers, the acceptor phase is not always physically in between the donor and the CBL). Better energy alignment also improves the Ohmic contact of the active layer with the electrodes which results into better device efficiencies (76). In addition to their electrical effects, buffer layers can also serve to improve device stability. Buffer layers can act as diffusion barriers against atmospheric oxygen and water, the main oxidizing agents for active layer materials. In addition to oxidation, the active layer is also susceptible to damage from UV light (79). Buffer layers can absorb UV light before it damages the active layer. Buffer layers can also protect the active layer from the roughness of the electrode materials. In addition, buffer layers can have advantageous optical effects such as improving light absorption to the active layer (80). The most widely used ABL is PEDOT:PSS. PEDOT:PSS is commonly paired with ITO as the anode material. PEDOT:PSS improves Ohmic contact, planarizes the ITO surface, and is also compatible with R2R processes (80). Unfortunately, the acidic and hygroscopic nature of PEDOT:PSS is detrimental to device stability (81, 82). Other ABLs include fullerene derivatives like PCBM and high work function oxides such as V_2O_5, VO_X, and MoO_3 (80). For CBLs, LiF is usually paired with an aluminum cathode (72). Other widely used CBL materials are low work function oxides such as TiO_2, TiO_X, ZnO, and Al_2O_3 (80). Unfortunately, none of the materials above individually

42

holds all the properties required of the ideal buffer layer; there is still much work to be done to find and develop the best buffer layer material.
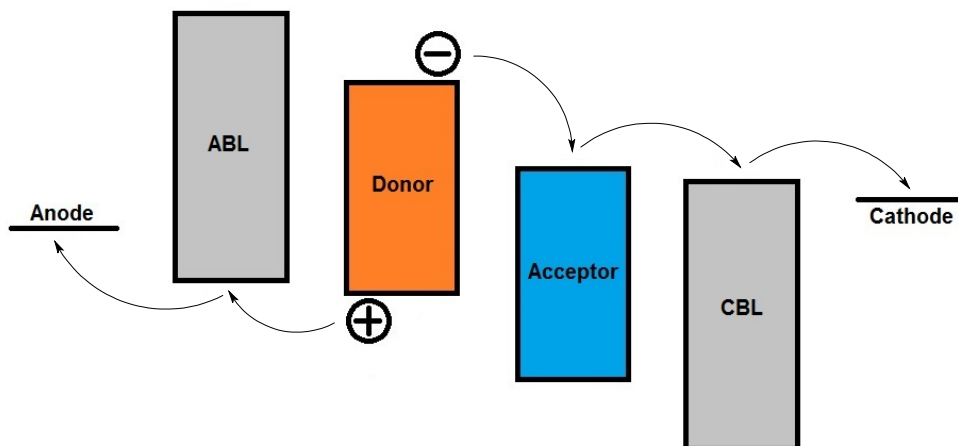

Figure 3.11 Energy level alignment and charge transport

3.4 Device efficiency

We have already touched on several aspects of device efficiency in our discussions above. This section will serve to organize those aforementioned details to create a more comprehensible picture of efficiency. We will formally define device efficiency, discuss challenges that limit efficiency, and outline the strategies to address those challenges.

3.4.1 The definition of efficiency

There are two general ways to define the efficiency of a solar cell. The first definition is the quantum efficiency and the second is the power conversion efficiency (PCE). The quantum efficiency compares the number of charge carriers collected at the electrodes to the number of photons incident to the device surface area at a specific wavelength of light (72). There are also

two distinctions of quantum efficiencies: external quantum efficiency (EQE) and internal quantum

efficiency (IQE). The EQE takes into consideration all photons that hit the device at a specific

wavelength whereas the IQE only considers the photons that are actually absorbed by the device

(72). The EQE and the IQE are seldom used in literature to compare device performance. For this

purpose, the PCE is preferred. One must be careful as the magnitudes of quantum efficiencies and

PCEs can be very different. Park *et al*. reported a device with an IQE close to 100% but with a

PCE of only 6.1% (83). The PCE measures the percentage of solar energy converted into electrical

energy. The PCE is more easily measured as it can be determined from the current density- voltage

(J-V) curve of a solar cell. Note that J-V curves are not unique to solar cells. These curves are often

used to characterize electronic components such as resistors and diodes. A J-V sweep is performed

on a device to generate a J-V curve, *i.e.,* a voltage is applied across the solar cell and the current

response of the solar cell is measured (84). Figure 3.12 shows a typical solar cell J-V curve under

illumination. Important parameters in the PSC J-V curve include the open-circuit voltage (V_{OC}),

the short-circuit current density (J_{SC}), and the maximum power generated by the device (P_{max}). The

V_{OC} is the voltage when the current density is zero whereas the J_{SC} is the current density when the

voltage is zero. The power generated by the device is simply the product of the current density and

the voltage. In Figure 3.12, V_{max} and J_{max} are the corresponding current density and voltage that

give out the maximum power, P_{max}. The PCE is simply the ratio of the maximum power output of

the device to the power provided by sunlight as shown in Equation (3.1)

$$PCE = \frac{P_{max}}{P_{IN}} = \frac{V_{max}\,J_{max}}{P_{IN}} \tag{3.1}$$

Another important parameter in the J-V curve is the fill factor (*FF*), In Figure 3.12, the *FF* square refers to the imaginary square (or rectangle) formed by the V_{max} and J_{max}. The *FF* itself, however, is the ratio between the areas of the *FF* square and the imaginary square formed by the V_{OC} and the J_{SC}. One can even interpret the *FF* as the "squareness" of the J-V curve (15). Note that a perfectly square (or rectangular) J-V curve would have an *FF* of unity. Equation (3.2) expresses the *FF* in simpler terms:

$$FF = \frac{V_{max} J_{max}}{V_{OC} J_{SC}} \tag{3.2}$$

The definition of the *FF* in Equation (3.2) can be combined with the definition of the PCE in Equation (3.1) to give us the following expression:

$$PCE = \frac{V_{OC} J_{SC} FF}{P_{IN}} \tag{3.3}$$

Note that P_{IN}, the power provided by sunlight, is easily controlled during characterization measurements. In fact, P_{IN} is usually kept at 100 mW/cm^2 of the solar spectrum (70). Equation (3.3) helps us understand how to improve device PCEs. Notice how the PCE is directly proportional to the V_{OC}, J_{SC}, and *FF*, *i.e.,* any improvement to these three parameters translates into an increase of the PCE. Thus, these three drivers of efficiency can be used as guides to understand how several factors affect the PCE of a device.
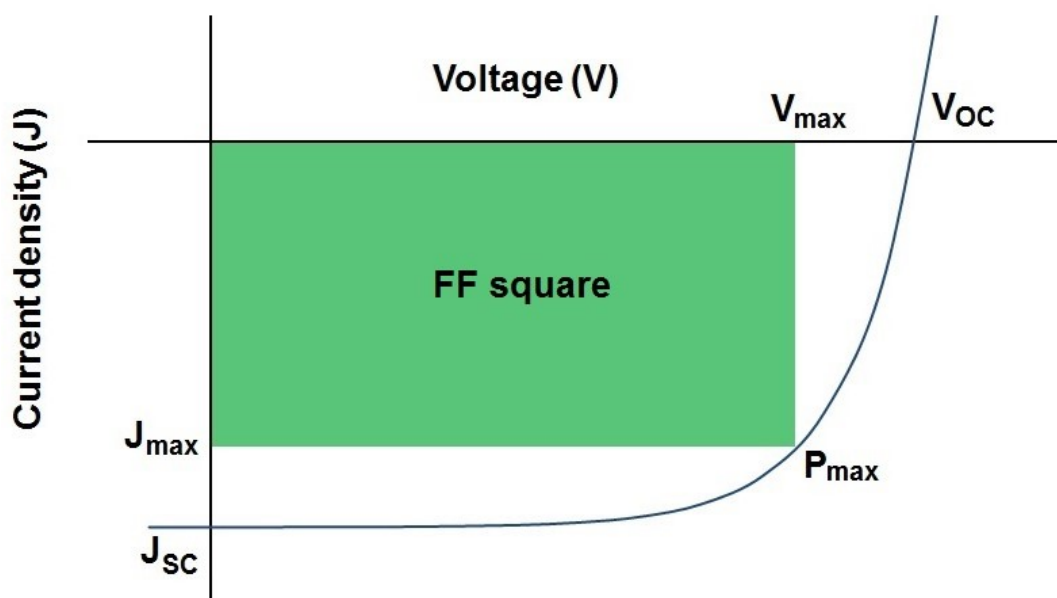
Figure 3.12 Current density-voltage (J-V) curve of a PSC

3.4.1.1 Open-circuit voltage (V_{OC})

The main factor that affects the V_{OC} is the relative placement of the frontier energy levels (*i.e.,* HOMO and LUMO) of the donor and acceptor (64). It may be helpful to refer back to Figure 3.4 to facilitate our present discussion. The V_{OC} is directly proportional to the difference between the HOMO of the donor and the LUMO of the acceptor, *i.e., V_{OC}* α ($LUMO_A - HOMO_D$). To increase V_{OC}, the LUMO of the acceptor must be increased or the HOMO of the donor must be decreased. However, the difference between the LUMOs of the donor and the acceptor ($LUMO_D - LUMO_A$) must be maintained to at least 0.3 eV as this energy difference provides the driving force for exciton dissociation (64). Thus, improving the V_{OC} largely depends on molecular design to fine-tune the energy levels of the active layer materials. Other factors that affect the V_{OC} include the bulkiness of polymer side chains, interchain distances, and the active layer morphology (46).

3.4.1.2 Short-circuit current density (J_{SC})

The J_{SC} is affected by many factors including the active layer's absorption breadth and intensity (64), the quantum efficiency of charge separation, charge carrier mobility (70), and even the active layer morphology (85). Akin to the V_{OC}, molecular design is the most popular way to increase the J_{SC}. For example, using low bandgap donors increases the breadth of the solar spectrum absorbed by the active layer. The bandgap of acceptors can also be engineered so they too can absorb light and generate excitons. This strategy, however, has been largely neglected since most fullerene materials absorb light in the UV range and their absorption coefficients are fairly poor compared to conjugated polymers (64). Other strategies to increase the J_{SC} will be discussed in Section 3.4.2.

3.4.1.3 Fill factor (FF)

The fill factor quantifies the competition between the sweep-out of the charge carriers to the electrodes and electron-hole recombination (70). The sweep-out time is limited by the mobility of the charge carriers and the morphology of the active layer. A more ordered morphology will allow charge carriers to reach their respective electrodes more easily. The most commonly used strategies to improve the active layer morphology are solvent annealing, thermal annealing, and the introduction of additive substances. Another strategy is the use of block copolymers to take advantage of microphase separation. The above strategies will be discussed in greater detail in Section 3.4.2. Aside from the active layer morphology, the interfaces between the active layer and the electrode also play a major role in the device's *FF* (64). These interfaces are usually improved by introducing the buffer layers discussed in Section 3.3.4.

3.4.2 PCE improvement strategies

PCE improvement strategies include molecular design and processing techniques. These two strategy types are often combined to achieve optimal results.

3.4.2.1 Molecular design

The molecular design of conjugated polymers as electron donors can be better understood by dividing its structure into the backbone, the side-chains, and the substituents (46). First, there are three types of backbones: homopolymer, donor-acceptor, and quinoid. The conjugated homopolymer backbone is often composed of single or fused aromatic rings as repeating units. Polymers with this type of backbone usually have relatively high bandgaps similar to P3HT (46). Donor-acceptor backbones are composed of alternating donor and acceptor moieties. Note that despite containing acceptor moieties, these polymers are still electron donors overall. The donor-acceptor backbone is commonly used for developing low bandgap polymers (64). The LUMO of the polymer largely depends on the acceptor moiety whereas the HOMO largely depends on the donor moiety, *i.e.,* one can easily tune the HOMO and LUMO of a donor-acceptor polymer by careful selection of the donor and acceptor moieties (85). Quinoid backbones are constructed by fusing two aromatic units in a specific geometry "to take advantage of the larger value of resonance energy of the first aromatic unit over the second unit" (46). The bandgap of the polymer is reduced since the quinoid resonance form is lower in energy than the aromatic form (46). Second, the side-chains are used for improving the solubility of the electron donor with other substances. The side-chains play a large part in making the polymer processable and in determining the active layer morphology. Third, the substituents can be used to adjust the HOMO and LUMO of the electron donor. Electron donating substituents like alkoxy groups can increase energy levels (more effect

48

for the HOMO) whereas electron withdrawing substituents like cyano groups or a fluorine atom can decrease energy levels (more effect for the LUMO) (64, 85). For electron donors, introducing electron withdrawing substituents is preferred as this will decrease the donor HOMO, thus increasing V_{OC}. Of course, one must be careful to preserve enough driving force between the donor and acceptor LUMOs after the introduction of the electron withdrawing substituents. In doing all the above modifications, one must always make sure that the π-π stacking of the electron donors is not negatively affected.

In contrast to electron donors, the molecular design of electron acceptors has been largely neglected. Consequently, a rational design process for electron acceptors in PSC applications has not been reported. Fullerene derivatives such as PCBM still remain as the standard electron acceptor due to their high electron mobility, ultrafast charge transfer, and their ability to form the BHJ morphology with conjugated polymers (60). However, fullerene derivatives are not perfect: they have weak absorption at the visible region, they have relatively low LUMO levels, and they have bad long-term stability (60). Upshifting the LUMO of fullerene acceptors can easily be done by the introduction of electron donating substituents (46, 85). Unfortunately, it is more difficult to improve the visible spectrum absorption and long-term stability of fullerene derivatives. It is wiser to develop non-fullerene acceptors for this purpose. In particular, conjugated polymer acceptors are a promising class of materials. Similar to their donor counterparts, conjugated polymer acceptors have high absorption coefficients in the visible region and their energy levels are easier to tune (86). Polymer donors and polymer acceptors can also be combined into block copolymers to take advantage of the self-assembling properties of these structures (42, 71, 86). There have been many non-fullerene acceptors reported in literature (59, 87), however, more work has to be done to determine the optimal structure to replace fullerene derivatives.

3.4.2.2 Processing techniques

Several processing techniques are used to improve device efficiencies. The most studied technique is thermal annealing (88-90). The process is implemented "by simply annealing a finished device on a hot plate" (72). Annealing the device above the glass transition temperature of the conjugated polymer (usually P3HT) results in enhanced crystallization within the conjugated polymer phase which increases hole mobility (91). The increased temperature also allows the polymer chains to move more easily around the BHJ matrix which is favourable for the morphology of the mixture. However, there is a limit to the annealing temperature as too much mixing can degrade the morphology. Remember that the BHJ morphology requires nanoscale phase separation and that there would be no phase separation if the donor and the acceptor mixed too well. For P3HT:PCBM blends, the optimal annealing temperature was reported to be around 140°C whereas thermal annealing at P3HT's melting point of 230°C resulted in lower J_{SC} and FF (88, 89). Another processing technique is solvent annealing. After spin-coating the active layer materials on the substrate (with one electrode and its buffer layer already deposited), the device is placed in a controlled atmosphere in order to manipulate solvent evaporation. Solvent annealing results in more organized polymer phases thereby improving photon absorption and hole mobility (72). The use of additives is another technique to improve efficiencies. Small amounts of additives are mixed in the solution of the donor, the acceptor, and the solvent for spin-casting. This technique is especially useful for devices whose morphologies cannot be improved with thermal annealing. For example, alkane dithiols were found to be excellent additives to the blend of a low bandgap polymer donor and a fullerene acceptor (92). The list of methods above is not exhaustive but these methods are the most widely used techniques to improve device efficiencies.

4 Computational theory

This dissertation primarily uses atomistic molecular dynamics (MD) and mesoscopic dissipative particle dynamics (DPD) for the study of the active layer morphology. We will begin with introductions to MD and DPD. Discussions will be limited to the general theoretical constructs of each method; we cannot do these two techniques justice for reasons of brevity. The reader is urged to consult more comprehensive references for a full explanation of these two techniques and their respective nuances (93-95). We will finish the chapter by introducing the Flory-Huggins theory. This theory plays an integral part in connecting MD and DPD, thus requiring a basic understanding of its fundamentals.

4.1 Molecular dynamics (MD)

Molecular dynamics (MD) can easily be understood by its name. "Molecule" refers to the scale of the simulations. MD treats systems in the scale of individual atoms. "Dynamics" refers to the manner in which the simulations are conducted. MD takes into account the forces experienced by atoms to predict how their positions and velocities will evolve in time. The first MD simulations were reported in 1958 by Alder and Wainwright when they studied the dynamics of hard spheres (94, 96). In 1964, Rahman was the first to apply MD simulations to study real liquids (94, 97). More than fifty years later, MD remains as one of the most popular computational techniques to study the most complex chemical, physical, and biological systems.

MD can be separated in three major steps: the initialization of the system, the system evolution, and the averaging of desired properties. An MD simulation schematic is shown in Figure 4.1. First, the system must be initialized. Thermodynamic parameters such as temperature, pressure, and

volume must be set. The initial positions, velocities, and forces of all atoms must also be set. Setting the forces acting upon all the atoms involves specifying all bond and non-bond pairwise interactions. In general, these would include van der Waals forces, covalent bonding, and electrostatic interactions. The set of these force definitions is referred to as the "force field" of the atom. Note that it is possible for atoms of the same species to have different force fields; it all depends on their individual environments. For example, an oxygen atom in a water molecule would experience different forces than an oxygen atom in an oxygen molecule. Although they are both oxygen atoms, the expression for the forces acting upon them would be different as one is bonded to two hydrogen atoms with single bonds whereas the other is bonded to another oxygen molecule with double bonds. After successful initialization, the system is evolved by solving Newton's equations of motion. Solution is done through discretization of variables and numerical integration. Solution of the equations of motion is continued until enough data points have been collected for analysis. The principles of statistical mechanics are then used to translate the results from the microscopic to the macroscopic environment. Statistical mechanics is a large subject by itself and will not be covered in this dissertation except for a conceptual description of statistical mechanical ensembles. The interested reader is directed to excellent reference books in statistical mechanics (98, 99). In general, MD is applicable to studying systems in the scale of nanometres and nanoseconds. However, the reader is cautioned about applying MD to smaller and faster systems. MD is not applicable in studying systems with significant quantum-mechanical effects. Problems involving electrons, protons, or light-matter interactions are not represented well by Newton's equations of motion.
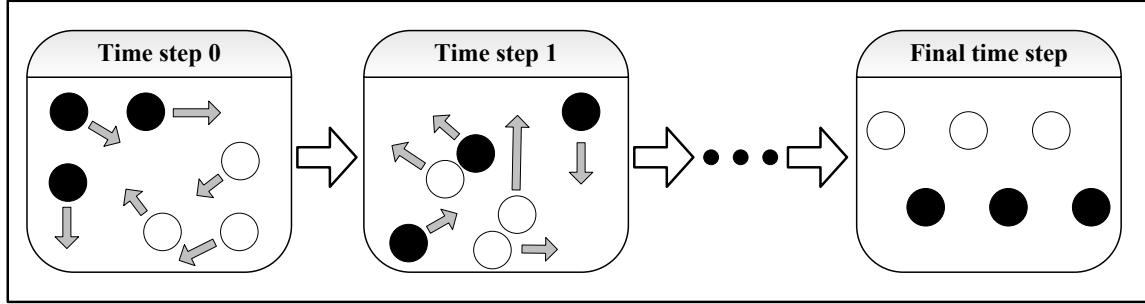
Figure 4.1 Molecular dynamics schematic

4.1.1 Force fields

Force fields describe the potential energy of the atoms in an MD simulation as a function of interatomic distances. The common form for a force field is given in Equation (4.1).

$$U(\vec{r}) = \sum_{bonds} K_r\left(r - r_{eq}\right)^2 + \sum_{bonds} K_\theta\left(\theta - \theta_{eq}\right)^2 + \sum_{dihedrals} \frac{V_n}{2}[1 + \cos(n\phi - \gamma)]$$

$$+ \sum_{i<j} \left(\frac{A_{ij}}{r_{ij}^{12}} - \frac{B_{ij}}{r_{ij}^{6}}\right) + \sum_{i<j} \frac{q_i q_j}{4\pi\varepsilon_0 r_{ij}} \tag{4.1}$$

The left hand side of Equation (4.1) refers to the total potential energy in the system. The symbol r refers to interatomic distances. Note how the r on the left hand side is in vector form as it represents the set of all interatomic distances in the system. The first, second, third, fourth, and fifth terms on the right hand side refer to potentials due to bond stretching, bond angle bending, rotations about dihedral angles, van der Waals interactions, and electrostatic interactions, respectively. The bond stretching potential represents the chemical bond as a harmonic oscillator. Notice how the first term is similar in form to the potential energy of a spring obeying Hooke's law. K_r is simply the bond stretching constant and r_{eq} is the equilibrium interatomic distance. The

second term is similar to the first; instead of distance, it quantifies bond angles. K_θ is the bond angle bending constant and θ_{eq} is the equilibrium angle. In the third term, V_n, n, and γ, are coefficients that quantify the barrier to rotation, the number of local extremes (maximum/minimum) in one full rotation, and the angular offset, respectively. The fourth term is the *AB* form of the Lennard-Jones potential where *A* and *B* are the constants for repulsion and attraction, respectively. In the fifth term, q refers to the charge of a specific atom and ε_0 is the permittivity of free space.

In practice, parameters are determined before the simulation, *i.e.,* the parameters in Equation (4.1) are already set as constants during the MD simulation. Force field determination can be done through experiments and first-principles calculations. Cramer gives an extensive list of force fields in his book (100).The most popular force fields used today include CHARMM (Chemistry at HARvard Molecular Mechanics), AMBER (Assisted Model Building and Energy Refinement), GROMOS (GROningen MOlecular Simulation), OPLS (Optimized Potential for Liquid Simulations), and COMPASS (Condensed-phase Optimized Molecular Potentials for Atomistic Simulation Studies). COMPASS (101) is the force field used for the simulations in this dissertation.

4.1.2 Statistical mechanical ensembles

The complete mathematical and physical treatment of statistical mechanical ensembles is quite involved and lengthy. For a complete theoretical development, the reader is advised to consult references on statistical mechanics (98, 99). The concept of ensembles is introduced in a conceptual fashion, as they apply to MD simulations in a practical manner.

MD simulations happen in systems within the scale of nanometres. The thermodynamic state of such systems can be characterized by only a handful of properties: the number of particles (N), the

system's chemical potential (μ), the system temperature (T), the system pressure (P), the system volume (V), and the system's total energy (E). In order to translate the particles' microstates to macroscopic properties of interest, MD simulations are performed under a chosen statistical mechanical ensemble. An ensemble is the collection of all possible microstates for a specified system. The ensemble chosen dictates which properties remain constant and which quantities are allowed to change. Ensembles are identified by the properties that remain constant. For example, in the *NVE*, also known as the microcanonical ensemble, the number of particles, the system volume, and the total system energy do not change. The NVE ensemble is the natural ensemble for the MD scheme, *i.e.,* no additional algorithms need to be implemented outside the solution of the equations of motion. Other common ensembles used in MD include the canonical ensemble, NVT, and the isothermal-isobaric ensemble, NPT. Implementing these other ensembles require additional algorithms such as thermostats and barostats to keep the temperature and pressure of the system constant. The ensemble used in a simulation is not limited to the aforementioned three and is usually chosen as the most appropriate to tackle the problem at hand.

4.1.3 Equations of motion

To demonstrate the equations of motion, consider a number of *N* particles in a system of volume *V*. We shall treat them in the NVE ensemble as it is the natural ensemble for MD. The following demonstration is adapted from Sholl and Steckel (102).

The total energy of the system is referred to as the Hamiltonian (*H*). The Hamiltonian is the sum of the total kinetic energy of the particles (*K*) as a function of their velocities ($\vec{v}$) and the total

potential energy of the particles (U) as a function of their positions ($\vec{r}$). Note that an equivalent notation may be employed where momentum is used instead of velocity.

$$H\,(\vec{v},\vec{r}) = K(\vec{v}) + U(\vec{r}) \tag{4.2}$$

K is defined by classical mechanics as:

$$K = \sum_{i=1}^{3N} \frac{m_i v_i^2}{2} \tag{4.3}$$

The reader should be reminded that the indicator does not stop at N, but at $3N$, under the assumption that the model is being studied in 3-dimensional space. On the other hand, the definition of U varies with the system and the force field chosen. The total potential energy of the system (U) is related to the force (f_i) acting on the ith coordinate of a particle by the following equation:

$$f_i = -\frac{\partial U(r_1, \dots, r_{3N})}{\partial r_i} \tag{4.4}$$

Newton's 2nd Law relates f_i with the particle's velocity at the ith coordinate.

$$f_i = m_i \frac{\partial v_i}{\partial t} \tag{4.5}$$

To complete the system of equations, the following fundamental relationship is also used.

$$v_i = \frac{\partial r_i}{\partial t} \tag{4.6}$$

4.1.4 Numerical integration

Numerical integration is applied to solve the system of differential equations presented above. Figure 4.2 shows a schematic of this solution process. Note that Newton's second law is an ordinary differential equation. The differential equations are discretized and the required variables are solved for in every time step. The most popular integration scheme in MD is the Velocity-Verlet algorithm (94). The discretized solution given by this algorithm is shown in Figure 4.2. An explicit formula for the forces cannot be provided because the expression would change depending on the system and the force field. The choice of the time step is crucial in balancing accuracy with computation time. In practice, a time step of 1 femtosecond (fs) is commonly used as dictated by the natural vibrational frequencies of the particles in the model. To put this into perspective, it would take $1\text{x}10^{15}$ iterations to simulate one full second of MD. Thus, MD simulations are usually set up in the magnitude of nanoseconds (ns). Notice that the equations used above are provided by classical mechanics. Quantum-classical mechanics formulations do exist for MD. However, classical mechanics already provides a good approximation for polymer systems without the additional strain on computational resources. As one can deduce from the system of equations above, the particles' positions and velocities are not the only quantities solved for in every time step. The algorithm must also calculate the force acting on each particle's coordinate direction and the total potential energy of the system as a function of all the coordinate positions. The required amount of computational power depends on the number of particles in the model. Again, one must balance accuracy with computation time.
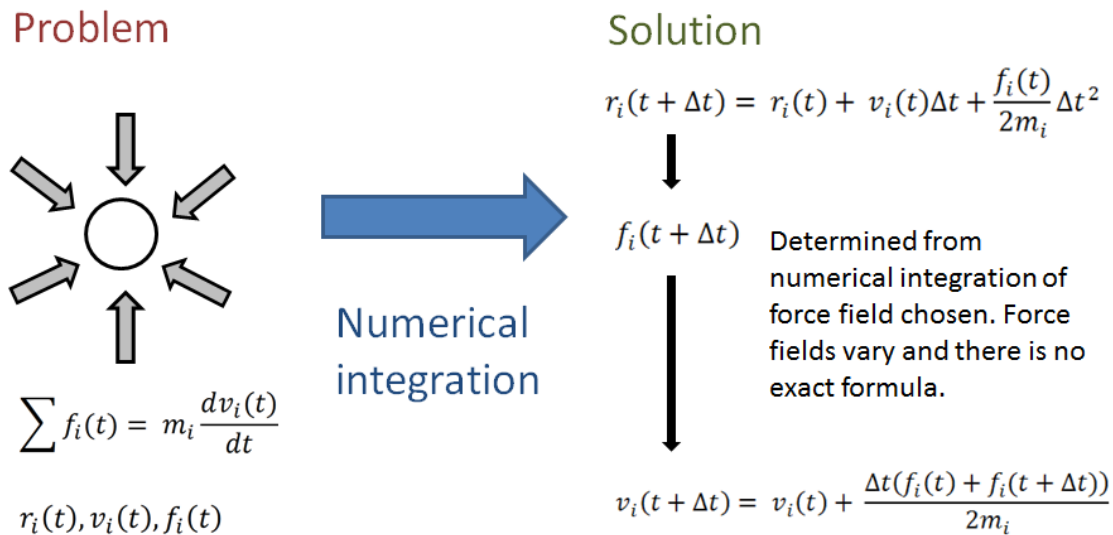
Figure 4.2 Solving Newton's equations of motion

Today, writing the integration code from scratch is not necessary. Many MD software packages are open-source and available for free such as *DL_POLY*, *GROMACS*, *LAMMPS*, and *NAMD*. Although computationally flexible and powerful, the disadvantage of these free programs is that their interface is not user-friendly; users must be comfortable working in a UNIX environment without any graphical user interface (GUI). The commercial program *Materials Studio* from BIOVIA (formerly Accelrys) provides a more intuitive interface at the price of less flexibility. Due to this less flexibility, *Materials Studio* is not usually implemented in supercomputers such as the WestGrid facilities of Compute Canada, thus limiting the computing power available for the software. Note that the computational studies presented in this dissertation were all implemented in *Materials Studio 5.0* due to logistical reasons.

4.1.5 Thermostats

The NVE ensemble is the natural implementation of MD. However, it is often desired to study systems in isothermal conditions as isothermal systems are more commonplace in real life than constant energy systems. The macroscopic system temperature is reflected by the kinetic energy of the particles in the system. In practice, it is convenient to define the "instantaneous kinetic temperature" of the system, *i.e.,* the temperature as defined by the kinetic energy of the particles:

$$T_{instant} = \frac{2K}{3Nk} \tag{4.7}$$

In the above equation, K is the instantaneous total kinetic energy of the system as defined in Equation (4.3), N is the total number of particles, and k is the Boltzmann constant. Note that the system temperature, T, is the average of all $T_{instant}$. During the initialization stage, the momentum (or equivalently, the velocity) of each particle is randomly assigned according to the Maxwell-Boltzmann distribution at that given T. The Maxwell-Boltzmann distribution gives the probability P of finding any one particle with a momentum p (98):

$$P(p) = \frac{\exp\left(\frac{-p^2}{2mkT}\right)}{(2\pi mkT)^{3/2}} dp \tag{4.8}$$

In the above expression, m is the mass of the particle. The variance of the distribution above is equal to mkT. When the MD algorithm is used to evolve the system, the total energy of the system will stay constant, but not the system temperature, *i.e.,* the initial Maxwell-Boltzmann distribution

of the particle momenta (velocities) will not be preserved. We need to implement additional algorithms to modify the particle velocities in the course of the simulation. These algorithms are called thermostats. Many thermostats have been developed, including Berendsen (103), Andersen (104), Nosé-Hoover (105, 106), and velocity-rescaling (107). Due to reasons of brevity, we will only look at the Berendsen thermostat as it is the thermostat used in this dissertation.

4.1.5.1 Berendsen thermostat

The Berendsen thermostat couples the system to a heat bath with the desired system temperature using first-order kinetics. The system temperature is corrected according to the following equation (108):

$$\frac{dT}{dt} = \frac{T_0 - T}{\tau} \tag{4.9}$$

Solution of Equation (4.9) reveals the following relationship:

$$|T_0 - T| \propto exp\left(\frac{-t}{\tau}\right) \tag{4.10}$$

In both expressions above, T is the instantaneous temperature (not the thermodynamic, average temperature), T_0 is the heat bath temperature, t is time, and τ is the decay time constant. Notice that a large time constant will drive the decay slower and vice-versa. For crude equilibration runs, the time constant can be made very small (~ 0.01 ps). For delicate production runs, the time constant should be relatively larger (~ 0.5 ps). In the latter case, the effect of the thermocouple on

the MD algorithm is minimized (108). In its implementation, the velocity of each particle is multiplied by a factor λ shown below (109):

$$\lambda = \left[1 - \frac{\Delta t}{\tau}\left(\frac{T - T_0}{T}\right)\right]^{1/2} \tag{4.11}$$

In Equation (4.11), Δt represents the discrete time step of the MD algorithm. The Berendsen thermostat introduces error to the fluctuation of kinetic energy in the system. This error scales with 1/N. Thus, ensemble average errors for very large systems are not significant; however, caution must be taken in calculating fluctuation properties such as heat capacity (108).

4.1.6 Barostats

Similar to thermostats, barostats are introduced to the MD algorithm to maintain constant pressure. Pressure is defined as force per unit area. We can also define the instantaneous pressure of the system as shown below (109):

$$P_{inst} = \frac{2}{3V}(K + W) \tag{4.12}$$

In the above equation, P_{inst} is the instantaneous system pressure, V is the instantaneous system volume, and K is the instantaneous system kinetic energy. The term W is defined by the following equation (109):

$$W = \sum_{i>j}^{N} (\vec{r_{iJ}} \cdot \vec{f_{iJ}}) \qquad (4.13)$$

In the above equation, r and f represent the position and forces acting upon each particle. Note that the vector notation is used as there are three components for each particle in a three dimensional system. The most popular barostats include Berendsen (103), Parrinello-Rahman (110, 111), and Martyna-Tuckerman-Tobias-Klein (MTTK) (112). For the same reasons of brevity, we will only look at the Berendsen barostat as it is the only barostat used in this dissertation.

4.1.6.1 Berendsen barostat

The Berendsen barostat couples the system to a pressure bath with first order kinetics. The pressure relaxation is done according to the following equation (108):

$$\frac{dP}{dt} = \frac{P_0 - P}{\tau_P} \qquad (4.14)$$

Notice the similarity in form between Equations (4.9) and (4.14). P is the instantaneous system pressure, P_0 is the pressure of the bath, t is time, and τ_P is the decay time constant for pressure control. To control pressure, the coordinates of each atom and the simulation cell vectors are scaled by the following factor:

$$\mu = \left[1 + \frac{\Delta t}{\tau} \gamma (P - P_0) \right]^{1/3} \qquad (4.15)$$

In the above equation, γ is the isothermal compressibility of the system and Δt is the discrete time step of the MD algorithm. Note that the Berendsen algorithm changes the size of the simulation cell uniformly in all directions, *i.e.,* the simulation cell will change size, but not its shape. If it is necessary for the simulation cell to change shape, the Parrinello-Rahman barostat is more applicable (109).

4.2 Dissipative particle dynamics (DPD)

Mesoscale structure and behaviour are important to many systems in biology and nanotechnology. In our case, the mesoscale is important as it is the relevant scale for the morphology of PSC active layers. Unfortunately, it is still prohibitively expensive to model these systems using atomistic MD. We need to combine MD with a mesoscopic simulation tool in order to predict the active layer morphology based on the molecular structure of the active layer materials. In this dissertation, we use Dissipative Particle Dynamics (DPD) as our mesoscopic simulation tool.

DPD is a particle-based method introduced by Hoogerbrugge and Koelman in 1992 (113, 114). Figure 4.3 illustrates the concept of DPD. Each DPD particle is commonly referred to as a "bead." These beads contain a collection of atomistic particles that move together as one unit. In fact, we can treat DPD as a coarse-graining of MD. Akin to MD, the motion of these beads are determined by the forces acting upon them. However, in addition to the conservative forces, DPD also includes dissipative and random forces to correctly simulate the hydrodynamic behaviour of fluids.
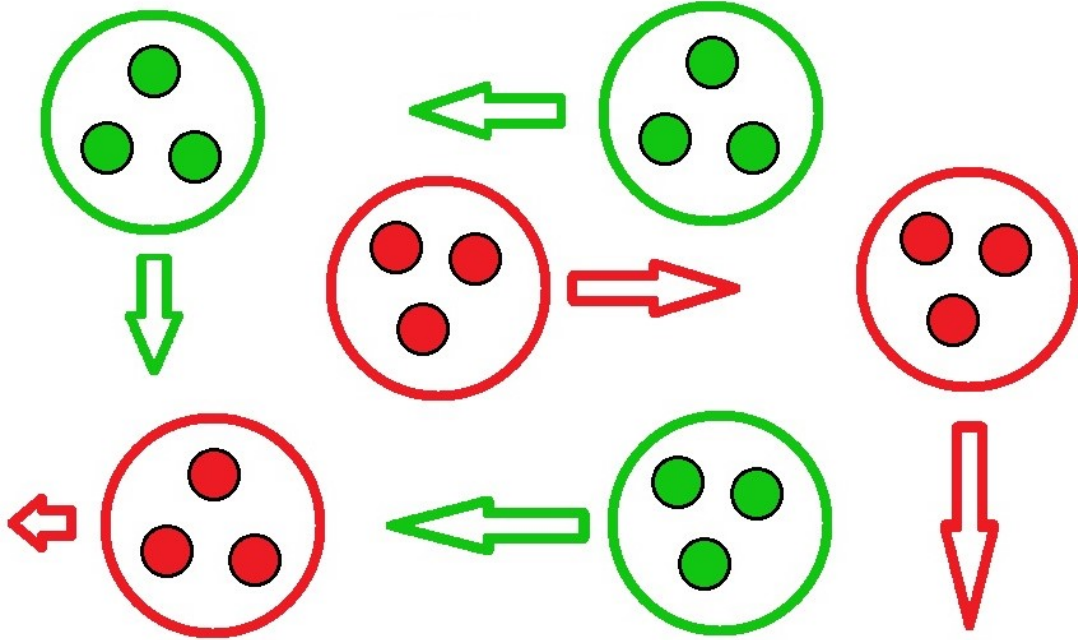
Figure 4.3 Conceptual schematic of DPD

4.2.1 Forces

There are three kinds of forces used in DPD simulations. The first force is conservative and represents the soft non-bonded repulsion between neighbouring beads. The soft repulsion force acted by bead j on bead i is shown below (115):

$$\vec{f}_{ij}^{C}(\vec{r}_{ij}) = \begin{cases} a_{ij}\left(1 - \dfrac{r_{ij}}{r_c}\right)\vec{e}_{ij}, & r_{ij} < r_c \\ 0, & r_{ij} \geq r_c \end{cases} \tag{4.16}$$

In the above equation, a_{ij} is the repulsion parameter between beads i and j, r_{ij} is the distance between beads i and j, r_c is the cutoff radius for bead interactions, and e_{ij} is the unit vector from bead j to bead i. The second force is dissipative and represents the frictional forces between the

64

beads. These dissipative forces reflect the viscosity of real fluids (115, 116). The dissipative force acted by bead j on bead i is shown below (95):

$$\vec{f}_{ij}^{D}(\vec{r}_{ij},\vec{v}_{ij}) = -\gamma\omega^{D}(r_{ij})(\vec{v}_{ij}\cdot\vec{e}_{ij})\vec{e}_{ij} \quad \left|\vec{v}_{ij} = (\vec{v}_i - \vec{v}_j)\right. \tag{4.17}$$

In the above equation, γ reflects the magnitude of the dissipative force and $\omega^{D}(r_{ij})$ is a function that describes how the dissipative forces change with respect to the distance between beads i and j. The third force is random and represents the degrees of freedom lost due to coarse graining. These random forces reflect Brownian motion (115). The random force acted by bead j on bead i is shown below (95):

$$\vec{f}_{ij}^{R}(\vec{r}_{ij}) = \sigma\omega^{R}(r_{ij})\xi_{ij}\vec{e}_{ij} \quad \left|\xi_{ij} = \xi_{ji}\right. \tag{4.18}$$

In the above equation, σ reflects the magnitude of the random force, $\omega^{R}(r_{ij})$ is a function that describes how the random forces change with respect to the distance between beads i and j, and ξ_{ij} is "a random variable with Gaussian distribution and unit variance" (94). The dissipative and random functions (ω^{D} and ω^{R}) are not independent of each other. In order for the system configurations to exhibit proper Boltzmann distribution, the fluctuation-dissipation theorem requires the following relationship (94):

$$\omega^{D}(r_{ij}) = \left(\omega^{R}(r_{ij})\right)^{2} \tag{4.19}$$

65

DPD simulates the canonical (NVT) ensemble. Note how the dissipative and random forces act as an indirect thermostat to the simulation as shown in the following relationship (94):

$$T = \frac{\sigma^2}{2k\gamma} \tag{4.20}$$

In the above equation, T is the simulation temperature, k is the Boltzmann constant, and γ and σ are the coefficients of dissipation and random forces, respectively. It is also important to note that collectively, all three forces obey Newton's 3rd law of action and reaction (116). Thus, total momentum is conserved in a DPD simulation. Momentum conservation is important as it is essential for recovering hydrodynamic behaviour in the continuum scales (94, 116).

4.2.2 Equations of motion

Akin to the MD scheme, DPD follows Newton's 2nd law of motion. The following system of equations describe the motion of beads in a DPD simulation (95):

$$\vec{f}_{ij} = \sum_{j \neq i} [\vec{f}_{ij}^{C}(\vec{r}_{ij}) + \vec{f}_{ij}^{D}(\vec{r}_{ij}, \vec{v}_{ij}) + \vec{f}_{ij}^{R}(\vec{r}_{ij})] \tag{4.21}$$

$$\vec{f}_{ij} = m\frac{d\vec{v}_i}{dt} \tag{4.22}$$

$$\vec{v}_i = \frac{d\vec{r}_i}{dt} \tag{4.23}$$

4.2.3 Numerical integration

Numerical integration is more straightforward in MD than it is in DPD; forces in MD depend only on positions whereas forces in DPD depend on both positions and velocities. This dependence comes from the fact that the dissipative forces are functions of the relative bead velocities. The stochastic nature of the random forces add even more complexity. To tackle these complications, Groot and Warren (117) introduced the modified velocity-Verlet scheme shown below:

$$\vec{r}_i(t + \Delta t) = \vec{r}_i(t) + \vec{v}_i(t)\Delta t + \frac{\vec{f}_i(t)(\Delta t)^2}{2m} \tag{4.24}$$

$$\vec{w}_i(t + \Delta t) = \vec{v}_i(t) + \frac{\lambda \vec{f}_i(t)\Delta t}{m} \tag{4.25}$$

$$\vec{f}_i(t + \Delta t) = \vec{f}_i\big(\vec{r}(t + \Delta t), \vec{w}(t + \Delta t)\big) \tag{4.26}$$

$$\vec{v}_i(t + \Delta t) = \vec{v}_i(t) + \frac{\big(\vec{f}_i(t) + \vec{f}_i(t + \Delta t)\big)\Delta t}{2m} \tag{4.27}$$

In the above equations, w is the predicted velocity and λ is an empirical factor introduced to account for some of the stochastic nature of the integration. The predicted velocity w was introduced to avoid numerous reiterations per time step in an effort to solve for the force and velocity terms simultaneously. The parameter λ can be tuned "to obtain properties to be expected of self-consistent solutions" (109). Stable and computationally efficient simulations were found to correspond with $\lambda = 0.65$ (109).

4.3 Flory-Huggins theory of mixing

The Flory-Huggins treatment is the most-widely used theory for polymer mixtures. In this dissertation, the original publication by Flory (118) and a more recent text by Strobl (43) were used as basis for the following explanation.

We first consider two different homopolymers, *A* and *B*. Homopolymers are macromolecular chains with uniform repeating units. Consider two states: before and after mixing. In the first state, n_A polymer chains of *A* are found in a volume V_A and n_B polymer chains of *B* are found in volume V_B. In the second state, n_A and n_B chains of *A* and *B* respectively are mixed in one volume, *V*. For the sake of this formulation, we will assume that the change in volume due to mixing is zero, *i.e.,* $V=V_A+V_B$. We are most interested in the phase behaviour of the polymer mixture. Will polymers A and B form a homogeneous phase in the volume *V* or will they phase separate? We use the change in the Gibbs free energy due to mixing, ΔG_{mix}. Mixing is favoured only if $\Delta G_{mix} < 0$, otherwise phase separation will occur. The Flory-Huggins treatment defines ΔG_{mix} as the sum of two contributions showed in Equation (4.28).

$$\Delta G_{mix} = -T\Delta S_t + \Delta G_{loc} \tag{4.28}$$

The first term on the right hand side of Equation (4.28) is the free energy contribution due to the change in translational entropy of the polymers upon mixing. Translational entropy is related to the accessible translational configurations to the polymer chains, *i.e.,* it is related to the motion of the centres of mass of the polymer chains. The change in translational entropy is always positive, thus the first term always favours mixing. Note that the local entropy is not included in the first term. The local entropy is related to the accessible configurations to the monomers. For example,

68

a monomer may be more restricted in movement after mixing. The local entropy is actually included in the second term. The second term represents the changes in free energy due to changes in the local free energy. Aside from local entropy, the second term also includes change in free energy due to the interactions between monomers. These interaction forces favour the attraction of like monomers more than the attraction of unlike monomers. Hence, the second term in Equation (4.28) is usually positive and would not favour mixing. In its current form, Equation (4.28) is not much use to us in predicting the polymer mixture phase behaviour; it needs to be expressed more explicitly in measurable terms.

In his book (118), Flory derived the expression for the entropy of mixing ΔS_t between polymer chains and an arbitrary solvent. In order to do this, Flory made use of the liquid lattice theory. Figure 4.4 shows an illustration of the liquid lattice where black filled circles represent monomers and white circles represent solvent molecules. Although the lattice is illustrated in 2D, Flory's treatment was actually derived without any assumptions on dimensionality. In this case, it is straightforward to derive the entropy of mixing. Let us define n_1 as the number of solvent molecules and n_2 as the number of solute molecules. The lattice contains n_0 cells where $n_0=n_1+n_2$. The total number of combinations for arranging the n_0 molecules is $\Omega=n_0!/(n_1!n_2!)$. As defined by Boltzmann, $\Delta S_t = k \ln \Omega$. After applying Stirling's approximation, $\ln n! = n \ln (n) - n$, we get the following equation.

$$\Delta S_t = k[(n_1 + n_2)ln(n_1 + n_2) - n_1 ln(n_1) - n_2 ln(n_2)] \tag{4.29}$$

If rearranged, Equation (4.29) actually simplifies to the entropy of mixing for ideal gases. In the case of polymers, the same method cannot be directly applied due to two major differences. The

first challenge is the size difference between the polymer and solvent molecules. One polymer molecule cannot occupy the same size lattice cell as a smaller solvent molecule. The second challenge is the restriction in which each cell occupied by one polymer monomer must sit adjacent to another monomer of the same chain.
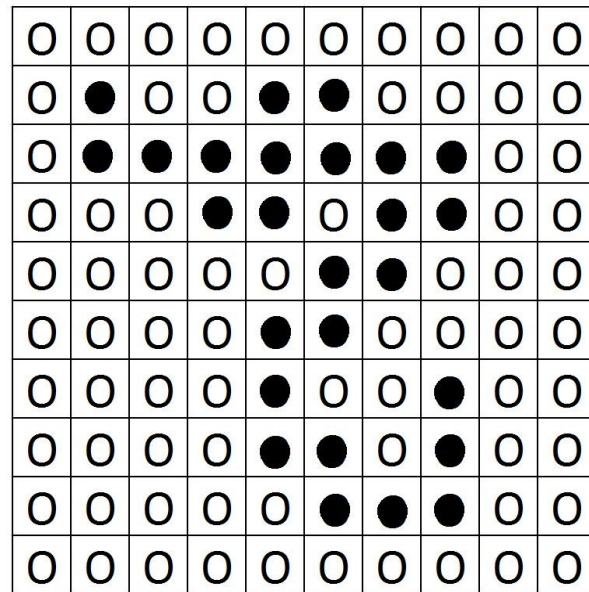

Figure 4.4 Flory's liquid lattice

Flory began his formulation by assuming an initial state of two unmixed substances, a crystallized polymer and an arbitrary solvent. He then defined a parameter, *x*, to denote the number of monomers there are for one polymer chain. Note that the monomer was defined such that it is of the same size as the solvent molecule. This treatment maintained the validity of the liquid lattice theory. Suppose that the polymer chains are laid in the lattice before the solvent molecules. Let us define the parameter *i* that indicates the number of polymer molecules already laid within the lattice, *i.e.,* in this moment, we are laying down polymer molecule number *i+1*. Also, in this moment, there are n_0-xi vacant cells available for the first monomer of the *(i+1)th* chain. Let us

also define z as the coordination number, *i.e.,* it is the number of first neighbors to any atom in the lattice. The second monomer of the $(i+1)^{th}$ chain is required to sit in one of the z cells counted. Now let us define the term f_i as the probability that a cell adjacent to a previously empty cell (*i.e.,* the cell that just got filled) is occupied. It is intuitive that the expected number of available cells for the second monomer is $z(1-f_i)$. It also follows that the expected number of available cells for the third monomer and all subsequent monomers is $(z-1)(1-f_i)$. Note that the latest two expressions neglect any monomers in their vicinity that are actually from another chain. We can now calculate the expected number of sets of cells, v_{i+1} that can hold our $(i+1)^{th}$ chain.

$$v_{i+1} = (n_0 - xi)z(z-1)^{x-2}(1-f_i)^{x-1} \tag{4.30}$$

If we now consider all indistinct polymer chains, we can calculate the total number of combinations that these polymer chains can be arranged in the lattice.

$$\Omega = \frac{1}{n_2!} \prod_{i=0}^{n_2} v_i \tag{4.31}$$

Strictly speaking, the value of f_i is not the same as $<f_i>$. Intuitively, $<f_i>$ is the number of vacant cells divided by the total number of cells, *i.e., $(n_0-xi)/n_0$*. For a lattice where $n_0 \to \infty$, the value of f_i also approaches $<f_i>$. Flory also noted that using a more detailed formula for f_i instead of its average value did not change the results significantly. Using the approximations *$z(z-1)^{x-2} \approx (z-1)^{x-1}$* and *$(n_0-xi)^x \approx (n_0-xi)!/(n_0-x(i+1))!$* together with the value of $<f_i>$, we re-express Equation (4.31) as

$$\Omega = \frac{1}{n_2!} \frac{n_0!}{(n_0 - xn_2)!} \left[\frac{z-1}{n_0} \right]^{n_2(x-1)} \tag{4.32}$$

At this moment, we have filled the lattice with all of our polymer chains. If the remaining solvent molecules are indistinguishable, then there is only one way for all the solvent molecules to fill the remaining void cells in the lattice. Thus, Equation (4.32) represents the total number of configurations for the mixture. Note that this would be equivalent to the configurational entropy of mixing of the perfectly ordered pure polymer and the pure solvent. Using Stirling's approximation and other simplifications, we arrive at the following formula. Note that the subscript 'C' refers to the entropy of mixing being derived from a pure crystallized polymer.

$$\Delta S_C = -k \left(n_1 ln \left[\frac{n_1}{n_1 + xn_2} \right] + n_2 ln \left[\frac{n_2}{n_1 + xn_2} \right] - n_2(x-1)ln \left[\frac{z-1}{e} \right] \right) \qquad (4.33)$$

The formation of the solution may be viewed as a 2-step process. The first step is the transformation of the crystallized polymer phase into a disoriented polymer phase. The second step is the mixing of the disoriented polymer phase with the solvent. We are more interested in the change in entropy for the second step. The entropy for the first step can easily be calculated from Equation (4.33) by setting the number of solvent molecules, $n_1 = 0$. The entropy of mixing for the second step can then easily be calculated by the difference of Equation (4.33) and Equation (4.33) at $n_1 = 0$ (*i.e.,* overall step − first step = second step).

$$\Delta S_t = -k(n_A ln\phi_A + n_B ln\phi_B) \qquad (4.34)$$

In Equation (4.34), φ_A and φ_B are the respective volume fractions for *A* and *B*, *i.e.,* $\varphi_A = V_A/V$. Flory's treatment could have easily been applied to a system of unlike polymer chains, instead of a polymer-solvent system. Flory claimed that the result in that case would be no different. It is

noteworthy that Equation (4.34) is simply a more generalized case of the expression for the entropy of mixing for ideal gases. Meanwhile, Equation (4.35) gives the expression for ΔG_{loc}.

$$\Delta G_{loc} = RT\frac{V}{v_c}\chi\phi_A\phi_B \qquad (4.35)$$

In Equation (4.35), R is the gas constant, v_C is a reference volume that is common for both polymer species, and χ is the well-known Flory-Huggins interaction parameter. Note that v_C can be any arbitrary volume; however, the volume of one of the monomers is usually chosen. The χ parameter reflects the interaction energy between A and B monomers. This parameter is dependent upon the chemical species of the monomers. A straightforward derivation of Equation (4.35) is presented by Strobl (43). The derivation considered the change in local free energy by the addition of one A chain into the mixture. Any changes to the local free energy were due to new A-B bonds formed with the additional A chain. The same scenario was considered with the addition of one B chain. The local free energy changes for both scenarios were then added together to yield Equation (4.35).

Combining Equations (4.34) and (4.35), we can now restate Equation (4.28) in a more explicit form. Note that the constants have also been re-expressed in order to give a more condensed form of the equation. Detailed derivations are shown by Strobl (43).

$$\Delta G_{mix} = RTn_c\left(\frac{\phi_A}{N_A}ln\phi_A + \frac{\phi_B}{N_B}ln\phi_B + \chi\phi_A\phi_B\right) \qquad (4.36)$$

In Equation (4.36), $n_c = V/v_c$, and N_A and N_B are the degrees of polymerization for polymers A and B. Notice that in the case where N_A and N_B are large, as is the case for most polymers, the first and

second terms disappear. It is important to note that derivation of the formula for the translational entropy was not a waste of time. The contributions of the entropy terms are significant at low degrees of polymerization. Strobl discusses the miscibility gap, one of the resulting effects at low degrees of polymerization (43). Now, let us consider the special case where the degree of polymerization for polymers A and B are equal, *i.e., $N_A=N_B=N$.* Under these conditions, Equation (4.36) can be simplified into Equation (4.37).

$$\Delta G_{mix} = RT(n_A + n_B)\chi N \phi_A \phi_B \qquad (4.37)$$

Upon careful examination of Equation (4.37), one can see that there are three parameters that can determine the phase behaviour of the polymer mixture: χ, N, and φ_A. Note that χ is already temperature dependent and that the terms (n_A+n_B) and φ_B are already related to φ_A. In fact, these three parameters χ, N, and φ_A are often used to construct phase diagrams for both polymer mixtures and block copolymers. For polymer mixtures, there are only two kinds of results. If ΔG_{mix} is negative, the mixture is homogeneous whereas the mixture separates into phases if ΔG_{mix} is positive. For block copolymers, the phase diagram is more complicated. The result is not only binary: there could be many ordered forms due to microphase separation. Obviously, more sophisticated methods are necessary to predict the phase behaviour of block copolymers. Nevertheless, we can treat block copolymers as a special case of a polymer mixture. In fact, block copolymer phase diagrams are still constructed using parameters defined by the Flory-Huggins treatment (119).

5 Multiscale computational study of P3HT-PFTBT active layers

The effects of polymer regioregularity, annealing temperature, and block copolymer architecture on the morphology of the polymer solar cell active layer are studied using a combination of molecular dynamics (MD) and dissipative particle dynamics (DPD). The electron donor and acceptor for the active layer are poly(3-hexylthiophene) (P3HT) and poly((9,9-dioctylfluorene)-2,7-diyl-alt-[4,7-bis(thiophen-5-yl)-2,1,3-benzothiadiazole]-2',2"-diyl) (PFTBT), respectively. The Flory-Huggins χ parameter between P3HT and PFTBT are calculated using MD simulations. Results are used as input for DPD simulations in order to predict the active layer phase morphology.

5.1 Background

The discussions in this chapter assume a basic understanding of polymer solar cells (PSCs), molecular dynamics (MD), dissipative particle dynamics (DPD), and the Flory-Huggins interaction parameter (χ). These topics were covered in Chapters 3 and 4. The background presented in this chapter is simply meant to orient the reader on how different topics presented in previous chapters come together to address the specific problems in this dissertation. Although references to figures and explanations in the previous chapters are made, relevant material are still reviewed as practical as possible for the convenience of the reader.

Polymer solar cells (PSCs) hold great promise in making solar energy more affordable. PSCs are cheaper to make and are easier to apply as building-integrated photovoltaics than their silicon-based counterparts. Unfortunately, their relatively low efficiencies hinder their successful commercialization. The PSC active layer morphology is one of the major factors limiting device

efficiencies. Figure 3.8 illustrates the evolution of the PSC active layer. The earliest devices were based on the single layer morphology. In this structure, the single active layer material absorbs photons to generate excitons (a bound electron-hole pair); however, exciton dissociation (separation of electron and hole) occurs only at the interface between the active layer and the electrodes (cathode and anode). Large improvements to device efficiencies were made when Tang introduced the bilayer heterojunction in 1986 (62). The bilayer heterojunction improved exciton dissociation with the introduction of two kinds of materials: the electron donor and the electron acceptor. Conjugated polymers are used as electron donors and fullerene derivatives are used as electron acceptors. Poly(3-hexylthiophene) (P3HT) and [6,6] – phenyl C_{61} butyric acid methyl ester (PCBM) are the benchmark donor and acceptor materials. Photon absorption and exciton generation occur in the electron donor phase as the absorption spectra of conjugated polymers match solar irradiation better than fullerene derivatives. Excitons then dissociate at the donor-acceptor interface (instead of the active layer-electrode interface) into electrons and holes. Excitons can only travel a maximum of about 10 nm before recombination, *i.e.,* excitons must find the donor-acceptor interface within 10 nm of its generation or the energy they hold will be lost. Although the bilayer heterojunction improved exciton dissociation, the stacked orientation of the two materials limited device thicknesses to about 20 nm (each of the donor and acceptor phases could only be 10 nm thick, assuming both phases can generate excitons). Devices that are too thin cannot absorb enough photons. This problem was solved when Yu *et al.* introduced the bulk heterojunction (BHJ) in 1995 (63). The BHJ is an interpenetrating network of donor and acceptor phases with phase domains in the range of 10-20 nm. The BHJ morphology allowed thicker devices without compromising exciton dissociation. The BHJ is so successful that it remains as the standard for active layer morphology to this day. Nevertheless, the BHJ can still be improved.

After exciton dissociation, the electrons are transferred from the donor phase to the acceptor phase while the holes remain in the donor phase. The electrons travel through the acceptor phase and find their way to the cathode whereas the holes travel through the donor phase and find their way to the anode. This step of charge collection is the biggest problem for the BHJ. Formation of the BHJ is random. The tortuous paths towards the electrodes slow down charge collection. Dead-end paths can also be formed for either phase, effectively trapping electrons and holes. In other words, the ideal active layer morphology is an ordered BHJ much like the lamellar structure in Figure 3.8. Notice how the lamellar structure simultaneously maintains benefits of the BHJ and facilitates charge collection. This lamellar structure can help push efficiencies high enough to make PSCs competitive with silicon photovoltaics.

A promising strategy to achieve the lamellar morphology is the use of block copolymers. Block copolymers are macromolecules made of at least two different kinds of polymers covalently linked together, *i.e.,* use of block copolymers for the active layer implies an all-polymer solar cell (both donor and acceptor are polymers). Block copolymers can form phase morphologies that are not normally seen in the case of simple polymer blends. These unusual phase morphologies are born of two competing factors. The first factor is the repulsive interaction between two unlike chemical species. The second factor is the covalent bond linking the two polymer species. The repulsive interaction pushes the two polymer species to segregate into different phases but the covalent link limits the degree of phase separation. This behaviour unique to block copolymers is called "microphase separation." Due to this behaviour, they cannot phase separate in macroscopic length scales (~100 − 1000 nm); instead, block copolymers phase separate in mesoscopic length scales (~ 5 − 100 nm) (120). Guo *et al*. recently showed that microphase separation can practically be used to achieve a lamellar morphology that improves performance for PSC devices (6). They used

poly(3-hexylthiophene) (P3HT) and poly((9,9-dioctylfluorene)-2,7-diyl-alt-[4,7-bis(thiophen-5-yl)-2,1,3-benzothiadiazole]-2',2"-diyl) (PFTBT) as electron donor and acceptors, respectively. Figure 5.1 shows the molecular structures of P3HT and PFTBT. Guo *et al.* reported better device efficiencies for P3HT-block-PFTBT devices than P3HT/PFTBT blend devices. They showed that device performance increased by more than 50% when lamellar structure was achieved for the active layer. They also found that thermal annealing had significant effects on the active layer morphology. Despite achieving a maximum power conversion efficiency (PCE) of 2.7%, block copolymer devices are still a long way from the highest organic photovoltaic (OPV) efficiency of 11.7% (23). Nevertheless, Guo *et al.* proved that block copolymers can pave the way for more competitive PSCs: we only need to find the best active layer materials and optimize their processing conditions.
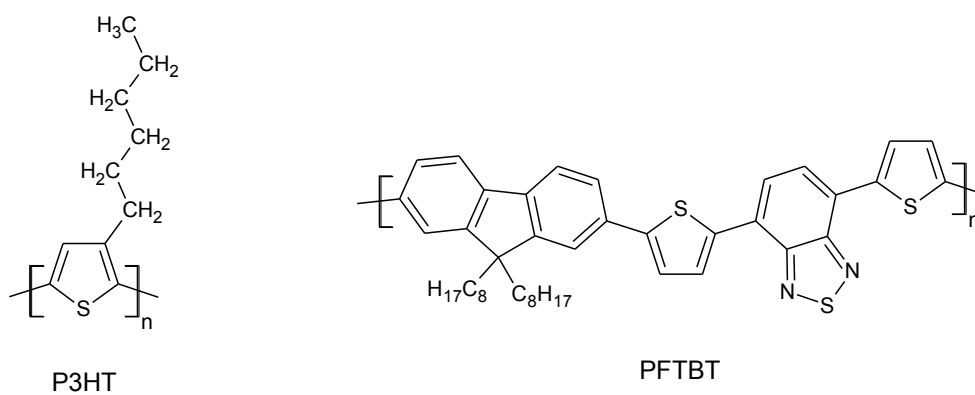
Figure 5.1 Molecular structures of P3HT and PFTBT

In our pursuit of better active layer materials, we must not forget to consider polymer regioregularity. Percent regioregularity (RR) is defined as the fraction of head-to-tail bonds in the polymer backbone. Figure 5.2 illustrates head-to-tail, head-to-head, and tail-to-tail bonds between P3HT monomers. Numerous studies have shown that high RRs (> 95%) can improve several

aspects of a P3HT/PCBM device including light absorption, charge transport, optical anisotropy, and conjugation length (121-125). These benefits are due to the ordered chain stacking within the P3HT phases. High P3HT RRs minimize steric interactions among the hexyl side chains resulting in more ordered crystalline phases. These benefits have inspired many to use highly regioregular P3HT in building their devices. However, many fail to consider the effect of RR on the active layer morphology as a whole (7). The studies cited above (121-125) only focused on the effect of RR on the P3HT phase morphology and ignored any effects to the PCBM phase. Other studies found that devices with moderate RRs (86% to 94%) exhibit better device stability through thermal annealing and operational aging (126-128). The ordered crystalline phases of highly regioregular P3HT induce greater degrees of phase segregation with PCBM for longer periods of thermal annealing and device operation, *i.e.,* the BHJ active layer morphology degrades more quickly for devices using highly regioregular P3HT. Highly regioregular P3HT have also been found to be incompatible with inkjet printing due to the formation of aggregates in the ink (129). Clearly, there is an RR optimization problem for P3HT/PCBM devices: RR must be high enough for better light absorption, charge transfer, anisotropy, and conjugation length whereas it must be low enough for thermal stability and processability.
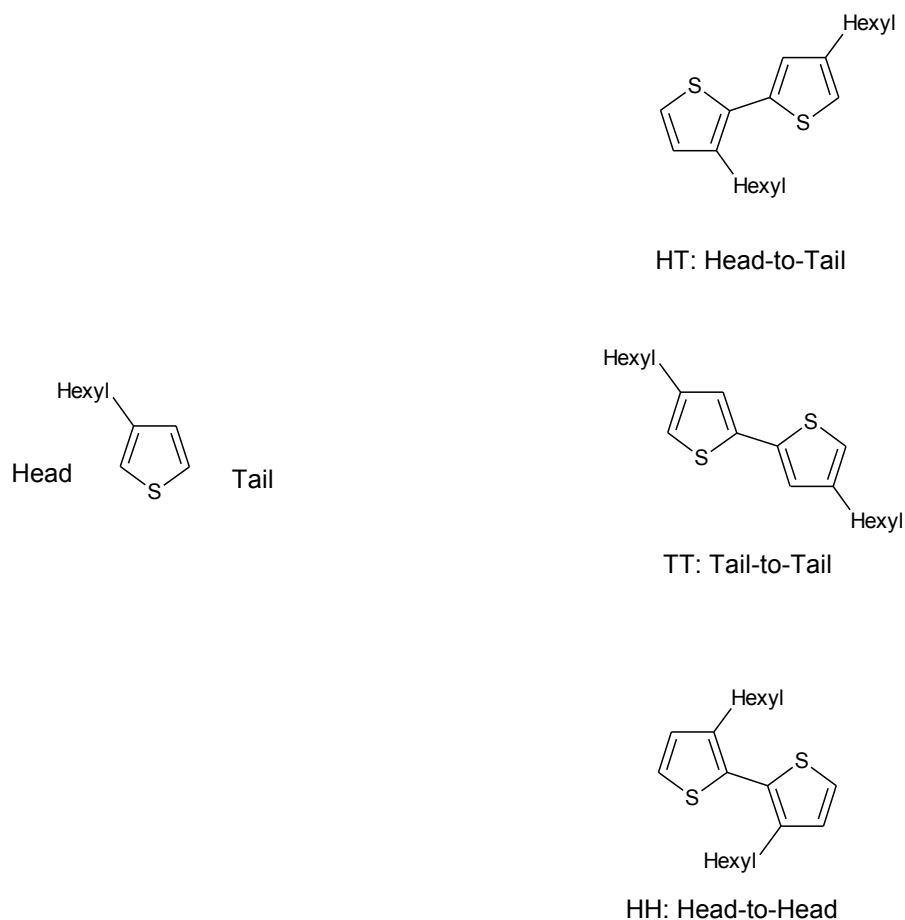
Figure 5.2 Head-to-tail, tail-to-tail, and head-to-head conformations of P3HT monomers

In contrast to P3HT/PCBM devices, the effects of RR in all-polymer solar cells are still largely unknown. The lack of benchmark materials for all-polymer solar cells can explain this issue. Figuring out the best donor-acceptor pair is already a huge challenge (86) and it takes precedence over optimizing polymer RR. Given the effects of RR on P3HT/PCBM devices, it is reasonable to assume that RR will also be a factor for all-polymer solar cells. In this dissertation, we specifically look at the effect of P3HT RR on the active layer morphology of an all-polymer solar cell. The P3HT/PFTBT system reported by Guo *et al.* was chosen as basis for our study due to their demonstration of the benefits of the block copolymer architecture (6).

Multiscale modeling is used to study the active layer morphology of the P3HT/PFTBT system. Figure 5.3 illustrates our computational strategy. This approach is commonly referred to as "message passing multiscale modelling" (130) as information is determined from a smaller scale and passed onto a larger scale in order to reduce the latter's degrees of freedom. The common strategy is to calculate atomistic dependent properties using molecular dynamics (MD) and pass on those properties as input to mesoscopic simulation techniques. Field theoretic methods such as MesoDyn (131-134) and particle-based methods such as Dissipative Particle Dynamics (DPD) (135-137) and coarse-grained molecular dynamics (CGMD) (138-141) have been used to study various polymer systems. In this dissertation, the Flory-Huggins interaction parameter (χ) between P3HT and PFTBT is calculated using atomistic MD. The χ parameter is then used as input for DPD simulations to study the mixing morphology of the two polymers for different levels of P3HT RR. The effects of annealing temperature and the effectiveness of the block copolymer architecture are also examined. All simulations presented in this dissertation were performed using the commercial software package, *Materials Studio 5.0*, by BIOVIA (formerly Accelrys). In the package, the following software modules were used: *Visualizer* for molecule construction and results visualization, *Amorphous Cell* for initial structure generation, *Discover* for MD simulation, and *DPD* for DPD simulations.
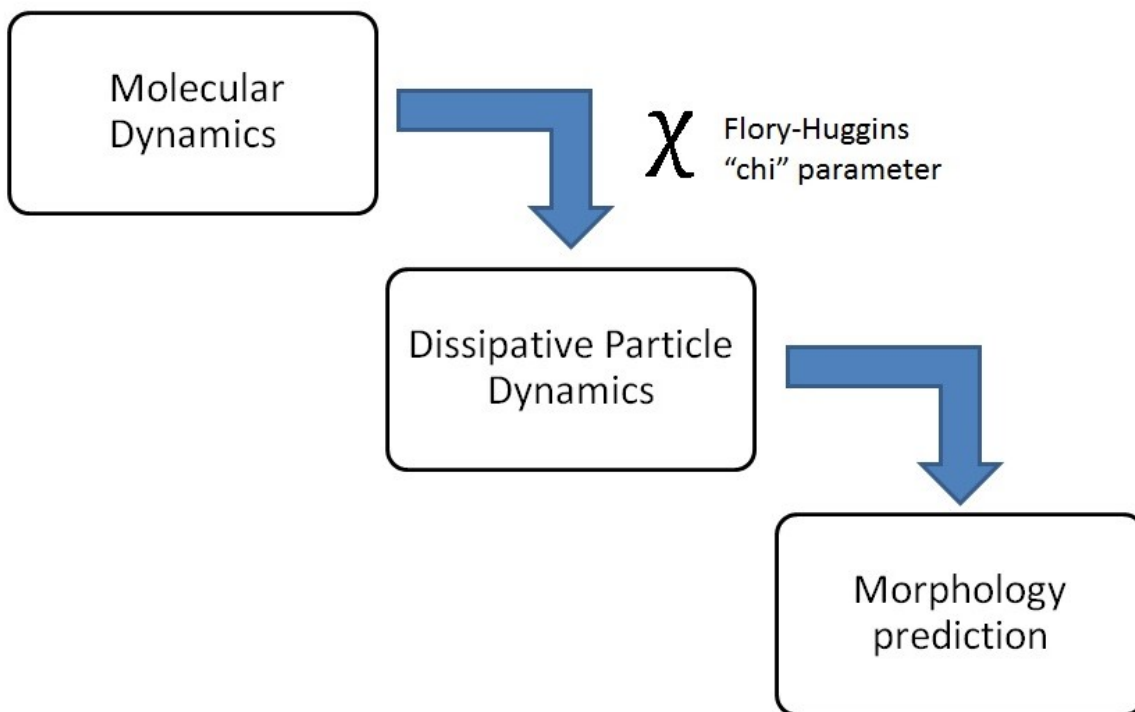
Figure 5.3. Message passing multiscale modeling strategy

5.2 Flory-Huggins interaction parameter (χ)

The Flory-Huggins interaction parameter (χ) values are calculated using atomistic MD simulations. We begin this section by outlining the procedures followed in our MD simulations. We then describe how the χ parameter is calculated using the MD simulation results. We finish this section with the analysis and discussion of our results.

5.2.1 Molecular dynamics (MD) methodology

Polymer structures were constructed using the polymer builder in *Visualizer*. P3HT and PFTBT model chains were built with 20 and 10 repeating units, respectively. Figure 5.1 shows the repeating unit structures used in the model chains. P3HT chains were built with varying degrees of RR. The chain with 100% RR was used as basis for all chains. To build chains with lower RRs,

bonds in the chain with 100% RR were flipped randomly. The probability of flipping was adjusted according to the desired level of RR. For example, a 10% flip probability was assigned to build a chain with 90% RR. The actual RR of the resulting chains were verified. Unlike P3HT, all PFTBT chains were built with 100% RR.

Table 5.1 lists the MD simulations conducted for this work. Three kinds of simulation cells were built as required for the calculation of the χ parameter between P3HT and PFTBT: pure P3HT cells, pure PFTBT cells, and cells containing a mixture of both. Pure P3HT cells contained 4 chains of 20-P3HT, pure PFTBT cells contained 2 chains of 10-PFTBT, and mixture cells contained 4 chains of 20-P3HT and 2-chains of 10-PFTBT. Consequently, all mixture cells contained 49 wt% P3HT and 51 wt% PFTBT. Five levels of P3HT RR were explored: 0%, 47%, 63%, 90%, and 100%. For each level of RR, three pure P3HT cells and three mixture cells were built for χ calculations. Since pure PFTBT cells are independent of P3HT RR, six pure PFTBT cells were generated for all RR levels. In addition, four annealing temperatures were explored: 373 K, 408 K, 438 K, and 503 K. The simulation cells used for the RR study at RR=100% was also used for the temperature study at T=438 K. For the other three temperatures (373 K, 408 K, and 503 K), two pure P3HT, two pure PFTBT, and two mixture cells were generated for χ calculations. All P3HT chains were 100% RR for the temperature studies. All simulation cells described above were constructed using *Amorphous Cell* (AC). AC builds molecules inside a 3-dimensional cell using a Monte Carlo process (109). Polymers are constructed by adding polymer segments one-by-one while minimizing close contacts and maintaining realistic torsion angle distributions. Candidates for the location of the new segment are evaluated based on the energy required for their insertion. Boltzmann weights are assigned to the candidates according to their insertion energies; candidates with lower insertion energies receive higher Boltzmann weights, meaning that they receive a

higher probability of being selected. To select the position of the new segment, a random number is generated and compared to the cumulative probabilities of the candidates. This process ensures that segments are introduced only to low energy insertion sites. Nevertheless, AC is known to fail when the target cell density is too high, especially for very large molecules such as polymers (109). To avoid this scenario, target cell densities were set between 0.05 g/cm^3 and 0.3 g/cm^3, way below the expected density of P3HT ~1 g/cm^3 (142). Subsequent MD simulations were all conducted using the *Discover* module. The cells were first subjected to 500 ps of NVT simulation to allow the polymer chains to reorient themselves into lower energy configurations. The cells were then subjected to NPT simulations to relax them to an equilibrium density. To determine the minimum amount of time for NPT simulations, density was tracked for a pure P3HT cell, a pure PFTBT cell, and a mixture cell up to 1500 ps. As shown in Figure 5.4, a steady-state density is reached within 400 ps of simulation for all three kinds of simulation cells. Thus, NPT simulations for this work were run for 1000 ps. The cells were then subjected to an additional 50 ps of NPT simulation to average the required properties for the calculation of χ. The Berendsen thermostat and barostat were used to control simulation temperature and pressures (0.1 MPa), respectively. Decay constants for both the thermostat and barostat were set at 0.1 ps. A time step of 1 fs was used for integrating the equations of motion. All MD simulations were conducted using 3D periodic boundary conditions to approximate bulk conditions.

Table 5.1. Summary of MD simulations

System	Regioregularity (%)	Temperature (K)	NVT MD (ps)	NPT MD (ps)	Repetitions
Mixture	0	438	500	1000	3
Mixture	47	438	500	1000	3
Mixture	63	438	500	1000	3
Mixture	90	438	500	1000	3
Mixture	100	438	500	1000	3
Mixture	100	373	500	1000	2
Mixture	100	408	500	1000	2
Mixture	100	503	500	1000	2
P3HT	0	438	500	1000	3
P3HT	47	438	500	1000	3
P3HT	63	438	500	1000	3
P3HT	90	438	500	1000	3
P3HT	100	438	500	1000	3
P3HT	100	373	500	1000	2
P3HT	100	408	500	1000	2
P3HT	100	503	500	1000	2
PFTBT	n/a	373	500	1000	2
PFTBT	n/a	408	500	1000	2
PFTBT	n/a	438	500	1000	6
PFTBT	n/a	503	500	1000	2
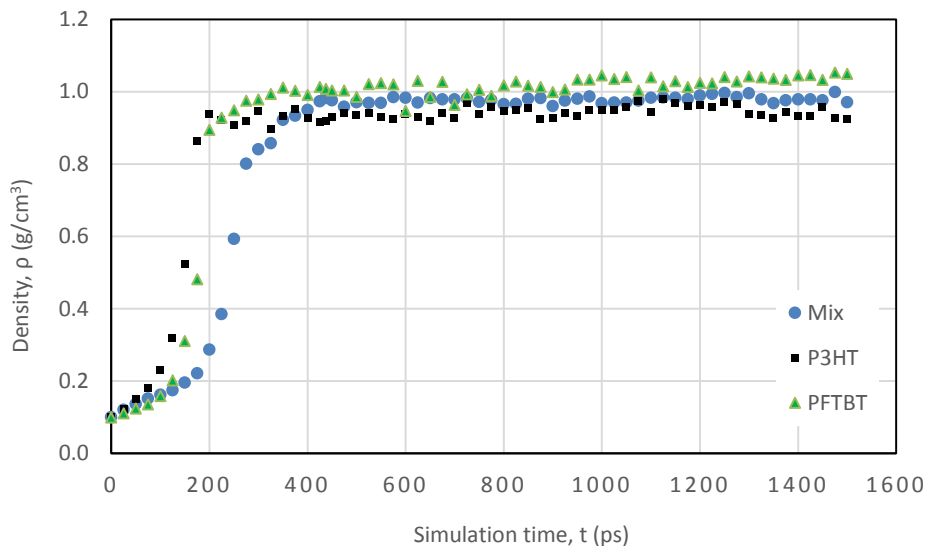
Figure 5.4 Evolution of simulation cell densities with respect to simulation time

The radial distribution function (RDF), *g(r)*, is often used to analyze the packing structure of crystals and molecules after an MD simulation. The RDF $g_{AB}(r)$ reflects the probability of finding an atom *B* at a radial distance *r* from any atom *A*. The RDF is defined by Equation (5.1) (143):

$$g_{AB}(r) = \frac{\langle n_{AB}(r) \rangle}{4\pi r^2 \Delta r \rho_{AB}} \tag{5.1}$$

In the above equation, *A* and *B* are the atom types of interest, *r* is the radial distance, ρ_{AB} is the combined number density of *A* and *B* particles in the bulk, and $<n_{AB}>$ is the average number of A-B pairs between the distances *r* and *r+Δr* (143). The RDF is used extensively in the analysis of results.

5.2.2 Calculation of χ

The χ parameter quantifies the incompatibility between two chemical species; it can be calculated using the following formula (144):

$$\chi = \frac{\Delta H_{mix}}{RT\phi_1\phi_2} \tag{5.2}$$

In the above equation, ΔH_{mix} is the enthalpy of mixing, R is the universal gas constant, T is the temperature, and φ_1 and φ_2 are the volume fractions of the two components, P3HT and PFTBT. The enthalpy of mixing can be approximated with the energy of mixing as shown in Equation (5.3):

$$\Delta H_{mix} \approx \Delta E_{mix} = E_{mixture} - E_1 - E_2 \tag{5.3}$$

In the above equation, ΔE_{mix} is the energy of mixing, $E_{mixture}$ is the total potential energy of the mixture cell, and E_1 and E_2 are the total potential energies of the P3HT and PFTBT cells, respectively. Note that by definition, $\Delta H_{mix} = \Delta E_{mix} + P\Delta V_{mix}$, for an isobaric system. The approximation in Equation (5.2) is valid as there should be no change in volume ($\Delta V = 0$) in the Flory-Huggins lattice theory. This assumption was successfully verified. In fact, ΔV_{mix} was only around 1%. This small change in volume translated to the values of ΔH_{mix} and ΔE_{mix} being computationally equal. The value of χ calculated using Equation (5.2) quantifies the repulsion between the two polymers in both their entirety. It is customary to scale the calculated value of χ above to a reference volume equivalent to that of the smaller repeating unit (145). The χ values reported in this dissertation were normalized with respect to the volume of the P3HT repeating

unit. These χ values can be used to predict whether the two polymers will mix in the blend by comparing it with the critical χ value, χ_c:

$$\chi_c = \frac{1}{2}\left(\frac{1}{\sqrt{n_1}} + \frac{1}{\sqrt{n_2}}\right)^2 \tag{5.4}$$

In the above equation, n_1 and n_2 are the number of repeating units for the two polymers. In our models, n_1 and n_2 are 20 and 10, respectively. Thus, χ_c is equal to 0.146 for all our results.

5.2.3 Results and Discussion

Figure 5.5 shows the relationship between the χ parameter and P3HT RR for five levels of RR: 0%, 47%, 63%, 90%, and 100%. All reported values in the figure were determined at 438 K. This specific temperature was chosen as Guo *et al.* determined this to be the optimal annealing temperature for P3HT/PFTBT devices (6). Each χ value was calculated from the average of three runs. Note that the error for each calculated χ is relatively large compared to the magnitude of the χ value itself. This is a natural disadvantage of Equations (5.2) and (5.3). The magnitude of the energy of mixing (ΔE_{mix}) is very small compared to the magnitudes of the total potential energies of the mixture ($E_{mixture}$), pure P3HT (E_1), and pure PFTBT (E_2). The red dashed line in Figure 5.5 shows the value of χ_c. Notice that the χ values for all levels of RR are above the critical value, *i.e.,* P3HT and PFTBT are expected to not mix when blended together. Also note that there seems to be a pattern to the relationship between χ and RR. The χ value lies around 3 for RRs less than 50% whereas it lies around 1 for RRs greater than 80%. There also seems to be a transition period at RR=63%. To explain these trends, we must look closer at Equations (5.2) and (5.3). Five variables determine the χ value: temperature, composition (volume fractions of the two polymers), energy

88

of the mixture, energy of pure P3HT, and energy of pure PFTBT. Among these five variables, only the energy of the mixture and the energy of pure P3HT were not controlled variables in Figure 5.5. Thus, we can gain more insight by looking at the potential energy trends of the mixture cells and the pure P3HT cells.
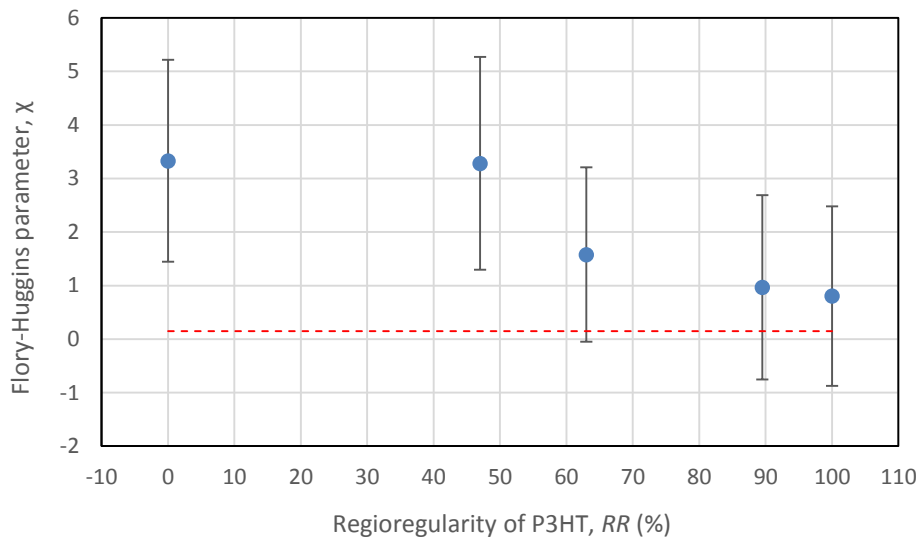
Figure 5.5 The Flory-Huggins interaction parameter between P3HT and PFTBT as a function of P3HT regioregularity at 438 K

Figures 5.6 and 5.7 respectively show the potential energy trends of the mixture cells and pure P3HT cells as a function of P3HT RR. There does not seem to be a pattern for Figure 5.6; the energies of the mixture cells appear to be equivalent with one another when the error bars are taken into consideration. For the sake of analysis, we can consider the mixture cell energies to be invariant with respect to P3HT RR. On the other hand, a clearer trend is shown in Figure 5.7. The pure P3HT cell energies increase with P3HT RR starting from RR=47%. The energy at RR=0% is comparable to the energy at RR=47%. This trend in the energy of pure P3HT cells corresponds to the trend shown in Figure 5.5. As the energy of pure P3HT increases, the χ value decreases as

dictated by Equations (5.2) and (5.3). To gain a better understanding of these trends, we look at the intermolecular radial distribution functions of the simulation cells.
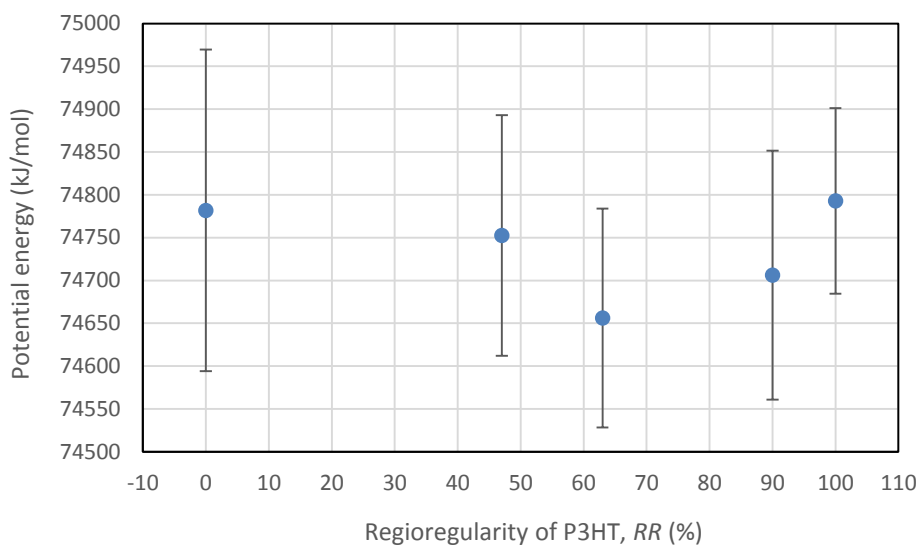
Figure 5.6 The potential energy of mixture cells with respect to P3HT regioregularity at 438 K
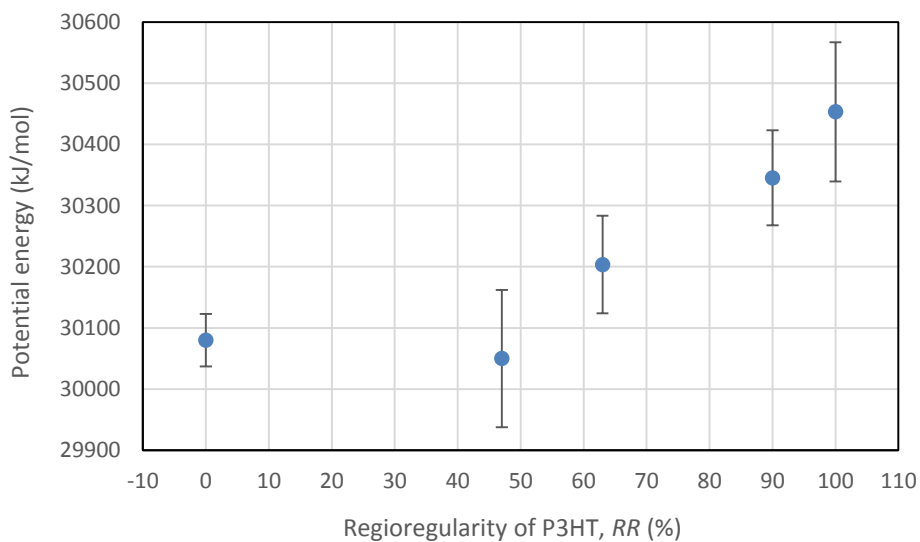
Figure 5.7 The potential energy of pure P3HT cells with respect to regioregularity at 438 K

Figure 5.8 shows the intermolecular radial distribution functions (RDFs) between the sulfur atoms of P3HT and PFTBT in the mixture cells at 438 K. Note that PFTBT has 3 sulfur atoms per repeating unit: two are located in two separate thiophene rings and one is connected to two nitrogen atoms. In all RDFs that follow, only the sulfur atoms in the thiophene rings are considered. As shown in the figure, there are no clear distinctions among the RRs of 0%, 47%, 90%, and 100%. These indistinct RDFs mean that the intermolecular structure between P3HT and PFTBT for all levels of RR are also indistinct. Note that the RDF of RR=63% is visibly lower than the other four for radial distances below 7 Å. This observation is consistent with the mixture cell potential energy being lowest at RR=63% as shown in Figure 5.6. Lower values of the RDF signify that the P3HT and PFTBT chains are farther away from each other. This configuration would be energetically favourable considering that P3HT and PFTBT are not miscible as shown in Figure 5.5. Nevertheless, it is important to note that such difference in the RDFs does not translate into significant differences in the mixture cell energies as shown in Figure 5.6. All in all, Figures 5.6 and 5.8 tell us that the interactions between P3HT and PFTBT in the mixture do not determine the χ-RR trend shown in Figure 5.5.
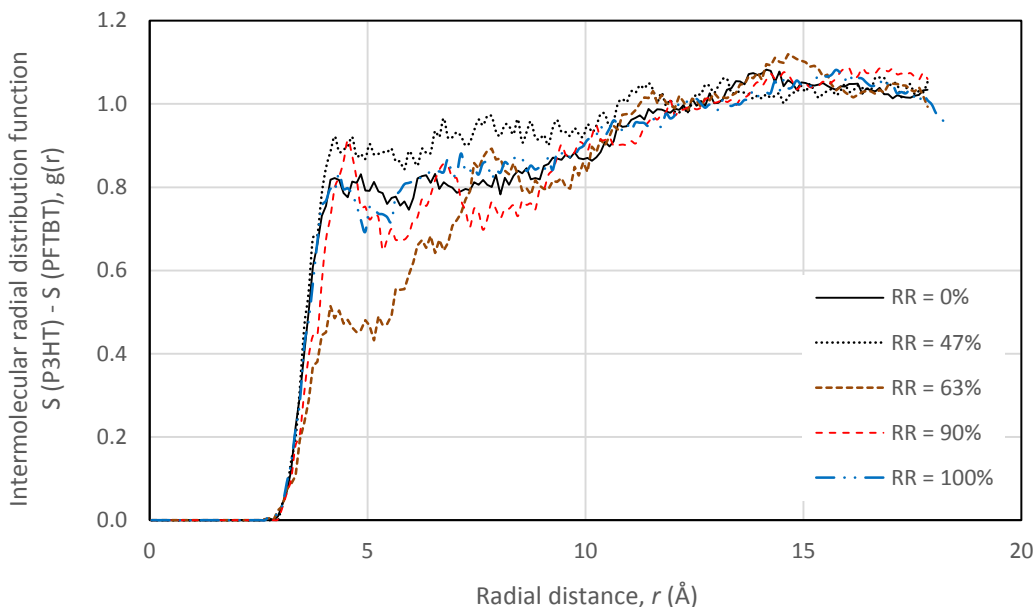
Figure 5.8 Intermolecular radial distribution functions between the thiophene sulfur atoms of P3HT and PFTBT in mixture cells at 438 K

Figure 5.9 shows the intermolecular RDFs between P3HT sulfur atoms in pure P3HT cells at 438 K. The figure shows undulating trends for all RRs which are consistent with RDFs reported by Alexiadis and Mavrantzas for the same system (146). These undulations suggest the formation of the energetically favourable π-π stacking (147) between the P3HT chains. More pronounced peaks indicate more π-π stacking, and consequently, lower energy for the pure P3HT phase. Figure 5.9 suggests that the degree of π-π stacking in the pure P3HT phase decreases with increasing RR, *i.e.,* there is more π-π stacking for RR=0% than RR=100%. This observation is consistent with the increasing energy trend shown in Figure 5.7 where the energy at RR=0% is lower than the energy at RR=100%. We can also examine the mean square end-to-end distance of the P3HT chains as a function of RR as shown in Figure 5.10. The π-π stacking structures are less likely to form when the P3HT chains are coiled up, *i.e.,* longer mean square end-to-end distances should correlate with more π-π stacking. Indeed, the trends shown in Figure 5.10 are largely consistent with the trends

in Figure 5.9. It is also noteworthy how much the trend in Figure 5.10 resembles the χ-RR trend shown in Figure 5.5. In short, the different levels of π-π stacking for different RR values determine the relationship between χ and RR. However, it is quite unexpected to find that higher levels of RR lead to less π-π stacking. According to experimental studies (121, 122), higher levels of RR lead to more ordered and denser π-π stacking. They explained this correlation as a result of less steric interactions for chains with higher RR. There are two possible explanations to reconcile the differences between the experimental observations in literature and the results of this work. First, there could be a difference in the stacking behaviour of P3HT chains between the crystalline phase and the amorphous phase. Experimental techniques only looked at the crystalline phase (146) whereas this work exclusively simulated the amorphous phase. Second, MD simulation times were not long enough leading to more π-π stacking than expected, especially for lower RRs. Simulation time would have to be extended or high temperature equilibration would have to be applied to verify the results (148). Unfortunately, these two explanations cannot be explored further due to the time constraints of the current project. Elucidation of this problem will have to be pursued in future studies.
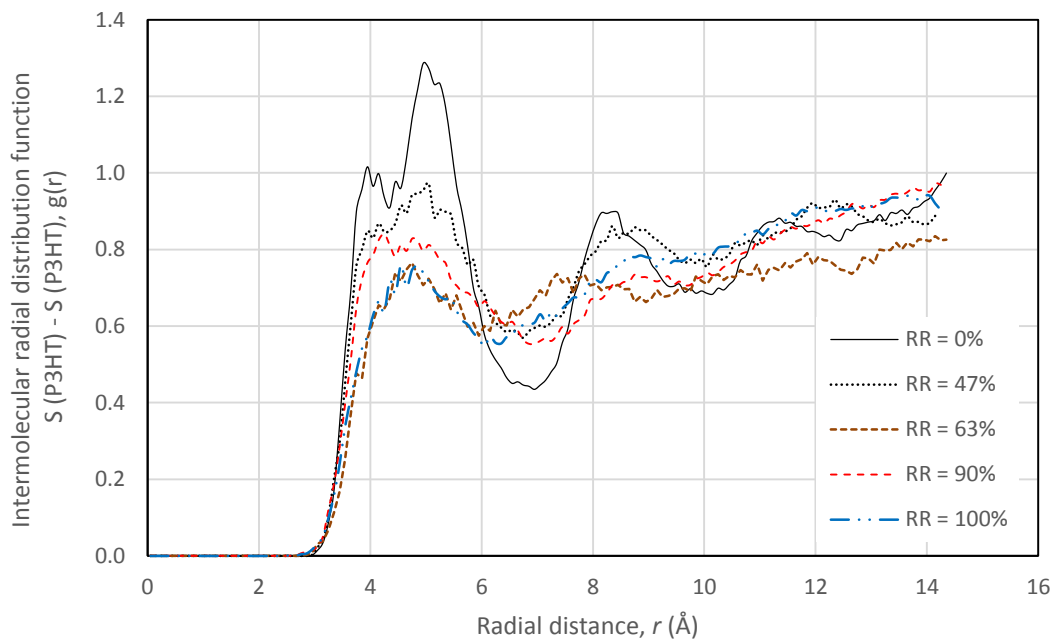
Figure 5.9 Intermolecular radial distribution functions between P3HT sulfur atoms in pure P3HT cells at 438 K
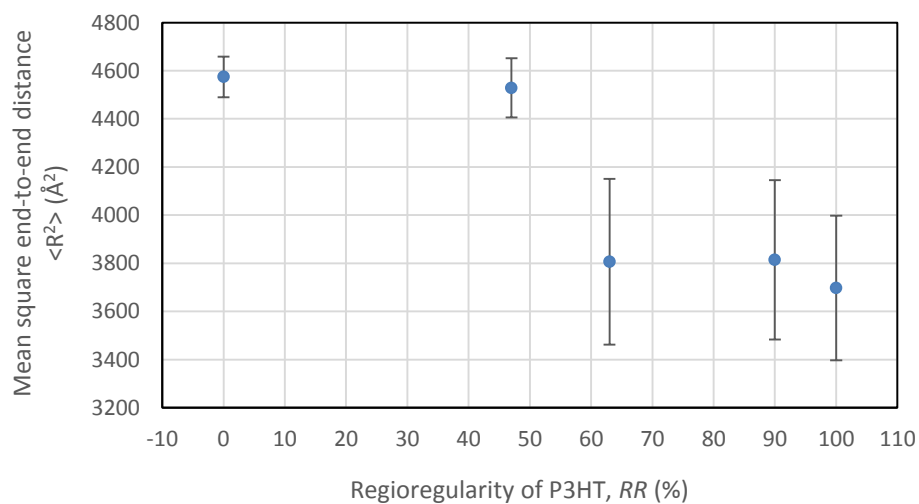
Figure 5.10 Mean square end-to-end distance of P3HT chains as a function of regioregularity in pure P3HT cells at 438 K

Figure 5.11 shows the relationship between the χ parameter and the reciprocal of temperature for four temperature levels: 503 K, 438 K, 408 K, and 373 K. The reciprocal of temperature was plotted on the x-axis instead of actual temperature as customarily done in literature (43). All reported values in the figure were determined at P3HT RR=100%. The χ value at 438 K was calculated from the average of three runs whereas the other three χ values were calculated from the average of two runs. Again, the error for each calculated χ is relatively large compared to the magnitude of the χ value itself due to the nature of Equations (5.2) and (5.3). The red dashed line in Figure 5.11 shows the value of χ_c. The χ values at 438 K, 408 K, and 373 K are all above the critical value, *i.e.,* P3HT and PFTBT are expected to not mix when blended together. However, the χ value at 503 K is below the critical value, *i.e.,* P3HT and PFTBT are expected to mix when blended together. Higher temperatures allow the polymer chains greater mobility, thus improving their miscibility. A regression line is fit in Figure 5.11 in the form of Equation (5.5):

$$\chi = \alpha + \beta \left(\frac{1}{T} \right) \qquad (5.5)$$

As shown, parameter values for α and β were calculated as -12.0 and 5.37×10^3 K, respectively. Now that the χ parameter values between P3HT and PFTBT have been determined for different conditions, the active layer morphologies these two polymers form can be predicted using DPD simulations.
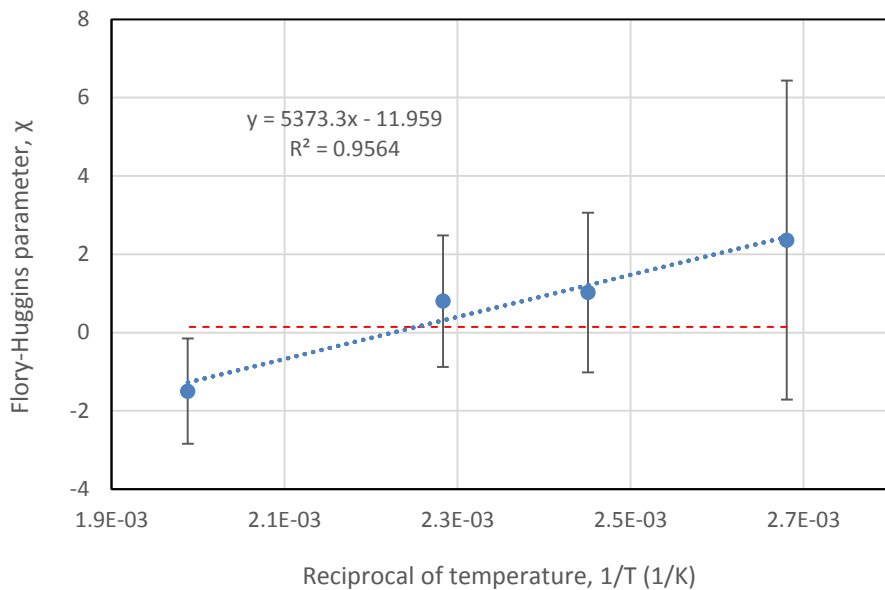
Figure 5.11 The Flory-Huggins interaction parameter as a function of the reciprocal of temperature at 100% P3HT regioregularities

5.3 Active layer morphologies

The active layer morphologies of P3HT/PFTBT systems are predicted by using the χ parameter values calculated in the preceding section as input to DPD simulations. In this section, we describe our DPD methodology and proceed straight to the analysis and discussion of our results.

5.3.1 Dissipative particle dynamics (DPD) methodology

All DPD simulations were conducted using the *DPD* module. DPD is a particle-based mesoscopic method implemented by coarse-graining atomistic elements. DPD simulations are conducted using reduced units. These reduced units can be translated to real physical quantities by setting the values of the bead mass (m), interaction radius (r_c), and reference energy (E_{ref}). The bead mass and interaction radius are set in the beginning of simulations according the system of interest. The reference energy is taken as the Boltzmann energy:

$$E_{ref} = kT \tag{5.6}$$

In the above equation, k is the Boltzmann constant and T is the physical temperature of the system. Note that all DPD simulations are conducted under the canonical ensemble (NVT), *i.e.,* system temperature is constant. All other physical dimensions can be derived by combining m, r_c and $E_{ref.}$ For example, the physical simulation time (t) can be calculated from the reduced simulation time (t_r) using the following formula:

$$t = t_r r_c \sqrt{\frac{m}{E_{ref}}} \tag{5.7}$$

In DPD, polymers are modeled as Gaussian chains as shown in Figure 5.12. Each bead represents a Kuhn segment of the polymer (109). For diblock copolymers, the Kuhn length of the stiffer block is chosen. Zhang *et al.* calculated the Kuhn lengths of P3HT and PFTBT to be 8 nm and 11.8 nm, respectively (149). Thus, a DPD bead mass of 3.71 kg/mol was used as it corresponds to an 11.8 nm segment of PFTBT. The beads were connected with harmonic springs of equilibrium length zero and spring constant of 4.0. The P3HT-PFTBT diblock copolymer was modeled as two connected chains with 4000 beads each, *i.e.,* a diblock model contained 8000 beads in total. This diblock model has a total mass of 29,600 kg/mol, comparable to the experimental 29,000 kg/mol by Guo *et al.* (6) The simulation cell comprised 64,000 (40 x 40 x 40) grids that contained 3 beads each. This setup amounted to a total of 24 polymer chains within a cubic box with each side measuring 106.0 nm. For P3HT-PFTBT blends (not diblock copolymers), the same setup was used,

except the P3HT and PFTBT chains were not covalently linked, resulting to 48 polymer chains. The 3D periodic boundary condition was applied to all simulations. The DPD systems were simulated for a total time of 1000 reduced units with a time step of 0.05; this translated to a physical simulation time of 84.6 ns. The dissipation parameters were set at 4.5 reduced units. The repulsion parameters for like beads (*i.e.,* P3HT-P3HT or PFTBT-PFTBT interactions) were set at 25 reduced units. The repulsion parameters for unlike beads (*i.e.,* P3HT-PFTBT interactions) were set according to the following equation:

$$a_{ij} = a_{ii} + 3.50\chi_{ij} \tag{5.8}$$

In the above equation a_{ij} and a_{ii} are the repulsion parameters for unlike and like beads, respectively, and χ_{ij} is the Flory-Huggins parameter between species i and j (P3HT and PFTBT). The dissipative and repulsive parameter values and equations were recommended by BIOVIA based on other studies in literature (109, 115, 117). Note that the χ parameter used here was normalized for the DPD bead volume and not the P3HT repeating unit as was done in the previous section. The unlike repulsion parameters used in this work are listed in Table 5.2. Note that not all the systems listed were simulated to minimize computational costs. Only one simulation was done for RR=0% and RR=47% because they have the same repulsion parameter values. For analytical purposes, the simulation done for RR=90%, T=438 K was interpreted as equivalent to the case of RR=100%, T=408 K due to the proximity of their repulsion parameters to each other (4% difference). Meanwhile, no DPD simulation was conducted for T=503 K as the negative repulsion parameter suggests complete miscibility between the P3HT and PFTBT phases.

Table 5.2 Unlike repulsion parameters for DPD simulations

Regioregularity RR (%)	Temperature T (K)	Unlike repulsion parameter a_{ij}
0	438	273
47	438	273
63	438	144
90	438	97
100	438	86
100	373	195
100	408	101
100	503	-86
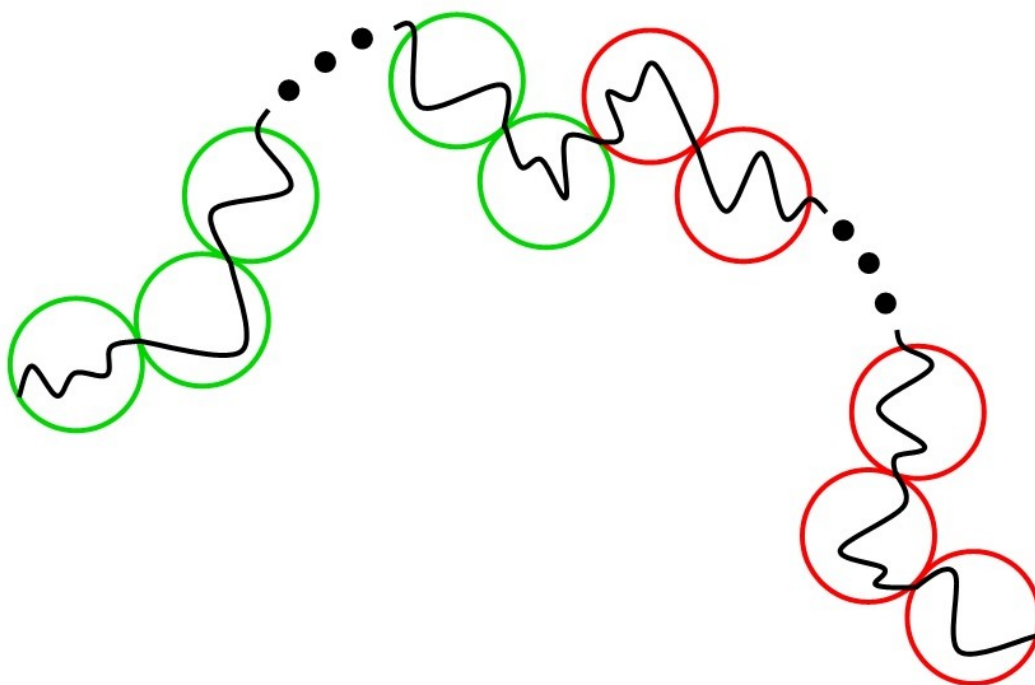
Figure 5.12 Illustration of a DPD diblock copolymer

5.3.2 Results & discussion

Figure 5.13 shows the orientation of the Cartesian axes with respect to the DPD simulation cells. Note that the placement of the x, y, and z axes was arbitrary and was only done to facilitate the comparison of the simulation results in Table 5.3. Table 5.3 shows the phase morphologies of P3HT and PFTBT systems according to our DPD results. In the images shown, P3HT is red and PFTBT is green. The first column describes the simulated system. The second column shows isometric pictures of the simulation cells. The third, fourth, and fifth columns show slices of the simulation cell parallel to the x-y, x-z, and y-z planes, respectively. Note that the slice planes were taken from the middle of the simulation cell, *i.e.,* all the slice planes shown intersect the centre point of the simulation cell. The first row shows the ideal phase morphology that reflects the lamellar structure shown in Figure 3.8. The second row shows the phase morphologies when P3HT and PFTBT are simply mixed in a blend, *i.e.,* they are not spliced covalently. This system does not resemble the ideal morphology in the slightest. Improvements to the morphology are shown in the third row for a diblock copolymer system with P3HT RR = 0% or 47%. Although we see hints of the ideal morphology in slice planes x-y and x-z, slice plane y-z is still far from ideal. P3HT RR increases as we move down the table. Drastic improvement is observed as P3HT RR is increased from 47% (3rd row) to 63% (4th row). Only small improvements are seen as P3HT RR is increased from 63% (4th row) to 90% (5th row) and from 90% (5th row) to 100% (6th row). Although Guo *et al.* never studied the effect of P3HT RR, they did report a lamellar morphology using diblock copolymers at 438 K with RR = 96% (6). Again, only small improvements are seen as temperature is increased from 373 K (7th row) to 408 K (5th row) and from 408 K (5th row) to 438 K (6th row). This trend is expected as thermal annealing is known to improve the active layer phase morphology of PSC devices (88). The degradation of the morphology from a lamellar structure at 438 K (6th

row) to a completely random structure at 503 K where the two phases are completely miscible (not simulated) is also expected. Extremely high temperatures have been reported to cause active layer morphology degradation for the same reason of too much miscibility between the donor and acceptor phases (88). It is also noteworthy that increasing the P3HT RR has greater benefits to the active layer morphology than increasing the annealing temperature. Our results confirm that using highly regioregular (RR > 90%) P3HT gives the best device performance. In the case of diblock copolymers, however, there does not seem to be an optimization problem for P3HT RR concerning its effects on active layer morphology. Our results suggest that increasing RR to 100% is most beneficial. Overall, the DPD simulations were able to qualitatively predict the active layer morphologies based on changing P3HT RR and the annealing temperature.
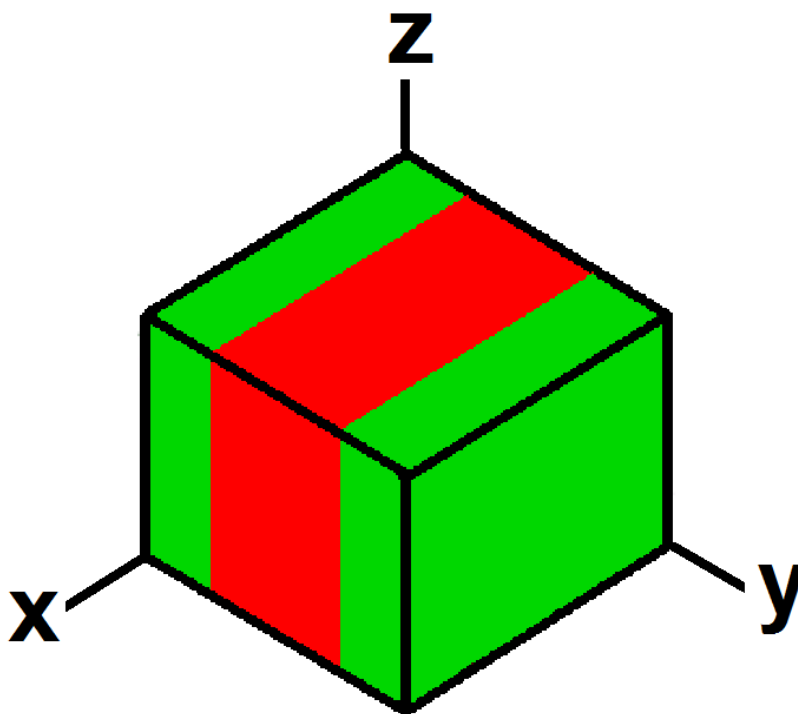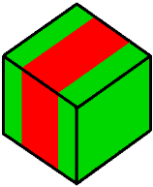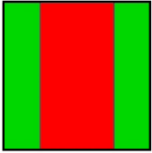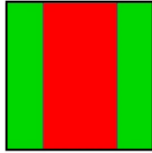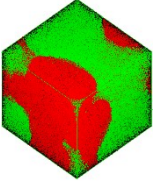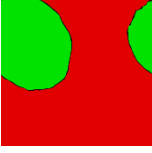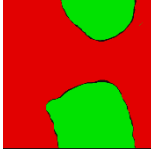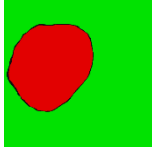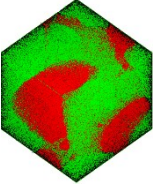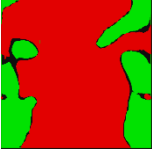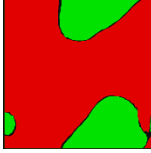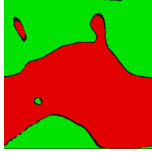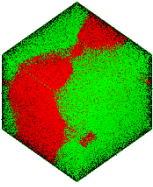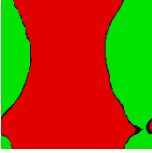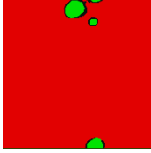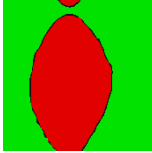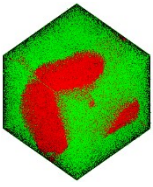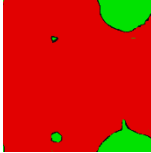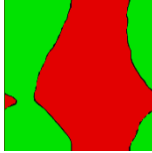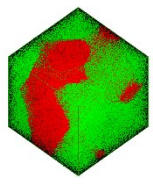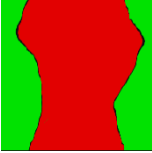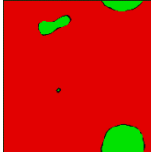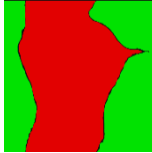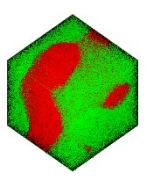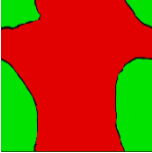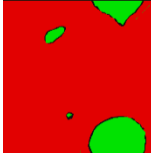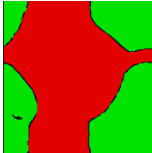
Figure 5.13 Orientations of the x, y, and z axes relative to the DPD simulation cell

Table 5.3 Phase morphologies as predicted by DPD simulations

System	Isometric	x-y	x-z	y-z
Ideal				
Blend RR = 100% T = 438 K				
Diblock copolymer RR = 0%/ 47% T = 438 K				
Diblock copolymer RR = 63% T = 438 K				
Diblock copolymer RR = 90% / 100% T = 438 K / 408 K				
Diblock copolymer RR = 100% T = 438 K				
Diblock copolymer RR = 100% T = 373 K				

Despite the qualitative utility of the results, the actual success of the DPD simulations in predicting the phase morphologies of conjugated block copolymer systems must be qualified. The DPD results have two major shortcomings. First, the actual size of the phase domains was not predicted accurately. Guo *et al.* (6) reported phase domains around 10 nm for the P3HT-block-PFTBT system at 438 K with RR = 96%. Our results show phase domains around 50 nm for the same system with RR = 100%. Second, Guo *et al.* reported that the lamellar morphology was not achieved for the diblock copolymer system at 373 K with RR = 96% whereas our results indicate a morphology only slightly different from that of 438 K. There are two possible explanations for the inaccuracies. First, DPD itself is not enough to accurately predict the morphologies of rod-coil polymers like P3HT. The DPD methodology works well with coil-coil polymers which rely only on Gaussian chain statistics and the interaction between unlike beads characterized by the χ parameter. The self-assembly of rod-coil block copolymers is complicated by the introduction of the anisotropic interactions of the rod blocks (71). In fact, two additional parameters are introduced to properly describe the behaviour of rod-coil block copolymers. The Maier-Saupe interaction strength quantifies the tendency of the rod blocks to align with each other. The other parameter is a measure of geometrical asymmetry which is a ratio between the radius of gyration of the coil block and the length of the rod block (71). Neither of these two parameters are included in DPD simulations. For more accurate results, the use of a more complicated simulation tool that considers these two parameters is necessary. Second, as mentioned before, MD simulation times were not long enough; this deficiency resulted in underestimated χ values which in turn contributed to the quantitative inaccuracy of the DPD results.

6 Conclusions and future work

The P3HT/PFTBT system was studied with a multiscale computational scheme that combined atomistic molecular dynamics (MD) and mesoscopic dissipative particle dynamics (DPD). The Flory-Huggins interaction parameters (χ) between P3HT and PFTBT were calculated using MD simulations. The χ parameters were then used as input for DPD simulations in order to predict the morphology formed by the P3HT/PFTBT system under different conditions.

Using MD simulations, average χ parameter values were calculated to be 3.3 for RR < 50%, 1.6 for RR=63%, and 0.9 for RR $\geq$ 90%. This χ-RR trend was caused by the increased π-π stacking for lower RR values. The reason for the increased π-π stacking remains to be unclear. In the crystalline phase, it is expected that higher RR would lead to better π-π stacking, and not the other way around. However, the RR and π-π stacking relationship may prove to be different in the amorphous phase as simulated in this work. It is suggested that this relationship in the amorphous phase be investigated in future studies. It will also be beneficial to extend the MD equilibration time or use high temperature equilibration to improve the quality of the MD simulation results.

In terms of temperature, the χ parameter was found to increase linearly with respect to the reciprocal of the absolute temperature (1/T) from 373 K to 503 K. The slope and intercept of the regression line for χ vs. (1/T) was calculated to be 5.37×10^3 K and -12.0, respectively.

Using DPD simulations, it was found that increasing RR to at least 63% greatly improves the morphology of P3HT-block-PFTBT active layers. Beneficial effects to the morphology were also found when increasing annealing temperature up to 438 K. Extreme temperatures (in this case 503 K) led to excessive miscibility between the two active layer components, thereby precluding the

formation of phase separated domains at the nanoscale. The beneficial effects of increasing RR were found to be greater than that of increasing annealing temperature. It was also observed that the ideal lamellar structures were not achievable when P3HT and PFTBT were simply mixed in a blend, *i.e.,* the diblock copolymer structure is essential in achieving the desired lamellar morphology.

Although qualitatively useful, the DPD simulations were not able to predict the phase domain sizes accurately. Experimental studies reported domain sizes around 10 nm whereas the DPD simulations predicted sizes around 50 nm. In addition, DPD simulations predicted a lamellar phase morphology for P3HT-block-PFTBT at 373 K whereas experimental studies reported otherwise. These inaccurate predictions were caused by the fact that DPD was designed to model coil-coil polymers and not rod-coil polymers like P3HT. To accurately predict the morphology of rod-coil polymers, the anisotropic interactions of the rod segments must be taken into consideration. The DPD method itself must be improved or a more complex computational tool must be used to accurately predict active layer morphologies.

The multiscale strategy of combining MD and DPD served as a qualitative guide to achieving the ideal phase morphology. High RRs, high annealing temperatures, and the block copolymer strategy were all found to be important in achieving the lamellar morphology. The relationship between RR and π-π stacking in amorphous phases should be explored in future studies. Finally, the predictive power of the methodology above can be improved by extending the MD equilibration time of these systems and by including anisotropic rod-rod interactions in the DPD simulations.

Bibliography

(1)   McKevitt, S.; Ryan, T. *The Solar Revolution;* Icon Books: London, 2014; pp. 1-346.

(2)   International Energy Agency. Executive Summary. *Energy Technology Perspectives 2014: Harnessing Electricity's Potential;* Paris, 2014; pp. 2-9.

(3)   Gevorgyan, S. A.; Søndergaard, R.; Krebs, F. C. Introduction. In *Polymeric Solar Cells: Materials, Design, and Manufacture;* Krebs, F. C., Ed.; DEStech Publications: Lancaster, PA, 2010; pp. 1-9.

(4)   International Energy Agency. *Technology Roadmap: Solar Photovoltaic Energy;* Paris, 2014; pp. 1-55.

(5)   Krebs, F. C. Manufacture. In *Polymeric Solar Cells: Materials, Design, and Manufacture;* Krebs, F. C., Ed.; DEStech Publications: Lancaster, PA, 2010; pp. 97-118.

(6)   Guo, C.; Lin, Y.-H.; Witman, M. D.; Smith, K. A.; Wang, C.; Hexemer, A.; Strzalka, J.; Gomez, E. D.; Verduzco, R. Conjugated Block Copolymer Photovoltaics with near 3% Efficiency through Microphase Separation. *Nano Lett.* **2013**, 13, 2957-2963.

(7)   Dang, M. T.; Hirsch, L.; Wantz, G.; Wuest, J. D. Controlling the Morphology and Performance of Bulk Heterojunctions in Solar Cells. Lessons from the Benchmark Poly(3-hexylthiophene):[6,6]-Phenyl-C_{61}-butyric Acid Methyl Ester System. *Chem. Rev.* **2013**, 113, 3734-3765.

(8)   Intergovernmental Panel on Climate Change. *Renewable Energy Sources and Climate Change Mitigation;* Cambridge University Press: New York, 2012; pp. 3-208, 333-400.

(9)   Intergovernmental Panel on Climate Change. *Climate Change 2007: Synthesis Report*; Core Writing Team, Pachauri, R. K., Reisinger, A., Eds.; Contribution of Working Groups I, II and III to the Fourth Assessment Report of the IPCC; Geneva, Switzerland, 2008; pp. 26-41.

(10)   International Energy Agency. *Solar Energy Perspectives;* Paris, 2011; pp. 1-161.

(11)   International Energy Agency. Executive Summary. *World Energy Outlook 2014;* Paris, 2014; pp. 1-7.

(12)   Pelland, S.; McKenney, D. W.; Poissant, Y.; Morris, R.; Lawrence, K.; Campbell, K.; Papadopol, P. *The Development of Photovoltaic Resource Maps for Canada.* 31st Annual Conference of the Solar Energy Society of Canada (SESCI), Montreal, Canada, Aug 20-24, 2006; [Online]. http://www.nrcan.gc.ca/energy/publications/sciences-technology/renewable/solar-photovoltaic/6199 (accessed April 15, 2015).

(13)   Balzani, V.; Credi, A.; Venturi, M. Photochemical Conversion of Solar Energy. *ChemSusChem* **2008**, 1, 26-58.

(14)   Gust, D.; Moore, T. A.; Moore, A. L. Solar Fuels via Artificial Photosynthesis. *Acc. Chem. Res.***2009**, 42, 1890-1898.

(15)   Fahrenbruch, A. L.; Bube, R. H. *Fundamentals of Solar Cells: Photovoltaic Solar Energy Conversion;* Academic Press: New York, 1983; pp. 1-24.

(16)   Moore, J. M. Photovoltaic Cells. In *Solar Energy: Renewable Energy and the Environment;* Foster, R., Ghassemi, M., Cota, A., Eds.; Energy and the Environment Series; Ghassemi, A., Ed.; CRC Press: Boca Raton, FL, 2010; pp. 115-133.

(17)   O'Regan, B.; Grätzel, M. A low-cost, high-efficiency solar cell based on dye-sensitized colloidal TiO_2 films. *Nature* **1991**, 353, 737-740.

(18)   Hagfeldt, A.; Boschloo, G.; Sun, L.; Kloo, L.; Pettersson, H. Dye-Sensitized Solar Cells. *Chem. Rev.* **2010**, 110, 6595-6663.

(19)   Kamat, P. V. Quantum Dot Solar Cells. The Next Big Thing in Photovoltaics. *J. Phys. Chem. Lett.* **2013**, 4, 908-918.

(20)   Madsen, M. V. Why polymer solar cells. Plasticphotovoltaics.org - a hub for OPV research. http://plasticphotovoltaics.org/lc/lc-polymersolarcells/lc-pol-why.html (accessed April 21, 2015).

(21)   Peng, C.; Huang, Y.; Wu, Z. Building-integrated photovoltaics (BIPV) in architectural design in China. *Energy Build.* **2011**, 43, 3592-3598.

(22)   Jelle, B. P.; Breivik, C.; Røkenes, H. D. Building integrated photovoltaic products: A state-of-the-art review and future research opportunities. *Sol. Energ. Mat. Sol. C.* **2012,** 100, 69-96.

(23)   Mitsubishi Chemical. R&D Strategy: Organic Photovoltaics. http://www.m-kagaku.co.jp/english/r_td/strategy/technology/topics/opv/ (accessed April 22, 2015).

(24)   Jørgensen, M.; Norrman, K.; Gevorgyan, S. A.; Tromholt, T.; Andreasen, B.; Krebs, F. C. Stability of Polymer Solar Cells. *Adv. Mater.* **2012,** 24, 580-612.

(25)   Norrman, K.; Madsen, M. V.; Gevorgyan, S. A.; Krebs, F. C. Degradation patterns in water and oxygen of an inverted polymer solar cell. *J. Am. Chem. Soc.,* **2010**, 132, 16883-16892.

(26)   Jørgensen, M.; Norrman, K.; Krebs, F. C. Stability/degradation of polymer solar cells. *Sol. Energy Mater. Sol. Cells,* **2008**, 92, 686-714.

(27)   Krebs, F. C. *Stability and Degradation of Organic and Polymer Solar Cells;* Krebs, F. C., Ed.; Wiley: Chichester, West Sussex, U.K., 2012; pp. 1-332.

(28)   Krebs, F. C. Fabrication and processing of polymer solar cells: A review of printing and coating techniques. *Sol. Energ. Mat. Sol. C.* **2009,** 93, 394-412.

(29)   Sze, S. M.; Lee, M. K. *Semiconductor devices: physics and technology,* 3rd ed.*;* Wiley: New York, 2012;

(30)   Servagent, N. Insulator, semiconductor, conductor. Semiconductor physics: Fundamentals. Optique pour l'ingénieur. http://www.optique-ingenieur.org/en/courses/OPI_ang_M05_C02/co/Contenu_02.html (accessed May 04, 2015).

(31)   Nave, R. Band Theory of Solids. Dept. of Physics and Astronomy, Georgia State University. hyperphysics.phy-astr.gsu.edu/hbase/solids/band.html (accessed May 07, 2015).

(32)   Spanggaard, H.; Krebs, F. C. A brief history of the development of organic and polymeric photovoltaics. *Sol. Energ. Mat. Sol. C.* **2004,** 83, 125-146.

(33)   Hunt, I. π Molecular Orbitals. Chapter 10: Conjugation in Alkadienes and Allylic Systems. University of Calgary. www.chem.ucalgary.ca/courses/351/Carey5th/Ch10/ch10-6-0.html (accessed May 12, 2015).

(34)   McMurry, J. *Organic chemistry,* 5th ed.; Brooks/Cole: Pacific Grove, CA, 2000; pp.1-24, 522-547.

(35)   Rawn, J. D.; Ouellette, R. J. *Organic chemistry;* Elsevier: San Diego, CA, 2014; pp. 1-39, 357-395.

(36)   Fung, D. D. S.; Choy, W. C. H. Introduction to Organic Solar Cells. In *Organic Solar Cells: Materials and Device Physics;* Choy, W. C. H., Ed.; Springer: New York, 2013; pp. 1-16.

(37)   Mayer, A. C.; Scully, S. R.; Hardin, B. E.; Rowell, M. W.; McGehee, M. D. Polymer-based solar cells. *Mater. Today.* **2007**, 10, 28-33.

(38)   Luhman, W. A.; Holmes, R. J. Investigation of Energy Transfer in Organic Photovoltaic Cells and Impact on Exciton Diffusion Length Measurements. *Adv. Funct. Mater.* **2011**, 21, 764-771.

(39)   Markov, D. E.; Amsterdam, E.; Blom, P. W. M.; Sieval, A. B.; Hummelen, J. C. Accurate Measurement of the Exciton Diffusion Length in a Conjugated Polymer Using a Heterostructure with a Side-Chain Cross-Linked Fullerene Layer. *J. Phys. Chem. A.* **2005**, 109, 5266-5274.

(40)   Mikhnenko, O. V.; Azimi, H.; Scharber, M.; Morana, M.; Blom, P. W. M.; Loi, M. A. Exciton diffusion length in narrow bandgap polymers. *Energy Environ. Sci.* **2012**, 5, 6960-6965.

(41)   Wang, H.; Wang, H.-Y.; Gao, B.-R.; Wang, L.; Yang, Z.-Y.; Du, X.-B.; Chen, Q.-D.; Song, J.-F.; Sun, H.-B. Exciton diffusion and charge transfer dynamics in nano phase-separated P3HT/PCBM blend films. *Nanoscale.***2011**, 2, 2280-2285.

(42)   McNeill, C. R. Morphology of all-polymer solar cells. *Energy Environ. Sci.* **2012**, 5, 5653-5667.

(43)   Strobl, G. *The Physics of Polymers: Concepts for Understanding Their Structures and Behavior,* 3rd ed.*;* Springer-Verlag: Berlin Heidelberg, 2007; pp. 1-491.

(44)   Heeger, A. J. Semiconducting and Metallic Polymers: The Fourth Generation of Polymeric Materials (Nobel Lecture). *Angew. Chem. Int. Ed.* **2001**, 40, 2591-2611.

(45)   Rienstra-Kiracofe, J. C.; Tschumper, G. S.; Schaefer III, H. F.; Nandi, S.; Ellison, G. B.; Atomic and Molecular Electron Affinities: Photoelectron Experiments and Theoretical Computations. *Chem. Rev.***2002**, 102, 231-282.

(46)   Zhou, H.; Yang, L.; You, W. Rational Design of High Performance Conjugated Polymers for Organic Solar Cells. *Macromolecules.* **2012**, 45, 607-632.

(47)   Shaheen, S. E.; Brabec, C. J.; Sariciftci, N. S.; Padinger, F.; Fromherz, T.; Hummelen, J. C. 2.5% efficient organic plastic solar cells. *Appl. Phys. Lett.* **2001**, 78, 841-843.

(48)   Brabec, C. J.; Winder, C.; Sariciftci, N. S.; Hummelen, J. C.; Dhanabalan, A.; van Hal, P. A.; Janssen, R. A. J. A Low-Bandgap Semiconducting Polymer for Photovoltaic Devices and Infrared Emitting Diodes. *Adv. Funct. Mater.***2002,** 12, 709-712.

(49)   Kittel, C. *Introduction to Solid State Physics,* 6th ed.; John Wiley: New York, 1986; p. 185.

(50)   Boudreault, P-L. T.; Najari, A.; Leclerc, M. Processable Low-Bandgap Polymers for Photovoltaic Applications. *Chem. Mater.***2011,** 23, 456-469.

(51)   Shaheen, S. E.; Vangeneugden, D.; Kiebooms, R.; Vanderzande, D.; Fromherz, T.; Padinger, F.; Brabec, C. J.; Sariciftci, N. S. Low band-gap polymeric photovoltaic devices. *Synth. Met.***2001**, 121, 1583-1584.

(52)   Winder, C.; Sariciftci, N. S.; Low bandgap polymers for photon harvesting in bulk heterojunction solar cells. *J. Mater. Chem.* **2004**, 14, 1077-1086.

(53)   Bundgaard, E.; Krebs, F. C.; Low band gap polymers for organic photovoltaics. *Sol. Energ. Mat. Sol. C.* **2007**, 91, 954-985.

(54)   He, Y. Acceptor Materials for Solution-Processed Solar Cells. In *Organic Solar Cells: Fundamentals, Devices, and Upscaling;* Rand, B. P.; Richter, H., Eds.; Pan Stanford: Boca Raton, FL, 2014; pp. 127-179.

(55)   Sariciftci, N. S.; Smilowitz, L.; Heeger, A. J.; Wudl, F. Photoinduced Electron Transfer from a Conducting Polymer to Buckminsterfullerene. *Science.***1992**, 258, 1474-1476.

(56)   Janssen, R. A.; Hummelen, J. C.; Lee, K.; Pakbaz, K.; Sariciftci, N. S.; Heeger, A. J.; Wudl, F.; Photoinduced electron transfer from π-conjugated polymers onto Buckminsterfullerene, fulleroids, and methanofullerenes. *J. Chem. Phys.* **1995**, 103, 788-793.

(57)   Hummelen, J. C.; Knight, B. W.; LePeq, F.; Wudl, F.; Yao, J.; Wilkins, C. L. Preparation and characterization of fulleroid and methanofullerene derivatives. *J. Org. Chem.***1995**, 60, 532-538.

(58)   Yang, C.; Kim, J. Y.; Cho, S.; Lee, J. K.; Heeger, A. J.; Wudl, F. Functionalized Methanofullerenes used as n-Type Materials in Bulk-Heterojunction Polymer Solar Cells and in Field-Effect Transistors. *J. Am. Chem. Soc.* **2008**, 130, 6444-6450.

(59)   Sonar, P.; Lim, J. P. F.; Chan, K. L. Organic non-fullerene acceptors for organic photovoltaics. *Energy Environ. Sci.* **2011**, 4, 1558-1574.

(60)   Cheng, P.; Zhao, X.; Zhou, W.; Hou, J.; Li, Y.; Zhan, X. Towards high-efficiency non-fullerene organic solar cells: Matching small molecule/polymer donor/acceptor. *Org. Electron.***2014**, 15, 2270-2276.

(61)   Liu, T.; Troisi, A. What Makes Fullerene Acceptors Special as Electron Acceptors in Organic Solar Cells and How to Replace Them. *Adv. Mater.***2013**, 25, 1038-1041.

(62)   Tang, C. W. Two-layer organic photovoltaic cell. *Appl. Phys. Lett.* **1986**, 48, 183-185.

(63) Yu, G.; Gao, J.; Hummelen, J. C.; Wudl, F.; Heeger, J. Polymer Photovoltaic Cells: Enhanced Efficiencies via a Network of Internal Donor-Acceptor Heterojunctions. *Science.* **1995**, 270, 1789-1791.

(64) Burkhart, B.; Thompson, B. C. Solution-Processed Donors. In *Organic Solar Cells: Fundamentals, Devices, and Upscaling;* Rand, B. P.; Richter, H., Eds.; Pan Stanford: Boca Raton, FL, 2014; pp. 3-69.

(65) Hoppe, H.; Sariciftci, N. S. Morphology of polymer/fullerene bulk heterojunction solar cells. *J. Mater. Chem.* **2006**, 16, 45-61.

(66) Janssen, R. A. J.; Hummelen, J. C.; Sariciftci, N. S. Polymer-fullerene bulk heterojunction solar cells. *MRS Bull.* **2005**, 30, 33-36.

(67) Li, G.; Shrotriya, V.; Huang, J.; Yao, Y.; Moriarty, T.; Emery, K.; Yang, Y. High-efficiency solution processable polymer photovoltaic cells by self-organization of polymer blends. *Nature Mat.* **2005**, 4, 864-868.

(68) Reyes-Reyes, M.; Kim, K.; Dewald, J.; Lopez-Sandoval, R.; Avadhanula, A.; Curran, S.; Carroll, D. L. Meso-Structure Formation for Enhanced Organic Photovoltaic Cells. *Org. Lett.* **2005**, 7, 5749-5752.

(69) Yang, X.; Loos, J.; Veenstra, S. C.; Verhees, W. J. H.; Wienk, M. M.; Kroon, J. M.; Michels, M. A. J.; Janssen, R. A. J. Nanoscale Morphology of High-Performance Polymer Solar Cells. *Nano Lett.* **2005**, 5, 579-583.

(70) Heeger, A. J. 25th Anniversary Article: Bulk Heterojunction Solar Cells: Understanding the Mechanism of Operation. *Adv. Mater.* **2014**, 26, 10-28.

(71) Segalman, R. A.; McCulloch, B.; Kirmayer, S.; Urban, J. J. Block Copolymers for Organic Optoelectronics. *Macromolecules.* **2009**, 42, 9205-9216.

(72) Søndergaard, R.; Gevorgyan, S. A.; Krebs, F. C. Materials and Processing. In *Polymeric Solar Cells: Materials, Design, and Manufacture;* Krebs, F. C., Ed.; DEStech Publications: Lancaster, PA, 2010; pp. 97-118.

(73) Krebs, F. C.; Gevorgyan, S. A.; Alstrup, J. A roll-to-roll process to flexible polymer solar cells: Model studies, manufacture and operational stability studies. *J. Mater. Chem.* **2009**, 19, 5442-5451.

(74) Galagan, Y. Flexible Substrates and Barriers. In *Organic Solar Cells: Fundamentals, Devices, and Upscaling;* Rand, B. P.; Richter, H., Eds.; Pan Stanford: Boca Raton, FL, 2014; pp. 591-637.

(75)   Yoo, S.; Lee, J.-Y.; Kim, H.; Lee, J. Electrodes in Organic Photovoltaic Cells. In *Organic Solar Cells: Fundamentals, Devices, and Upscaling;* Rand, B. P.; Richter, H., Eds.; Pan Stanford: Boca Raton, FL, 2014; pp. 219-276.

(76)   Duan, C.; Zong, C.; Huang, F.; Cao, Y. Interface Engineering for High Performance Bulk-Heterojunction Polymeric Solar Cells. In *Organic Solar Cells: Materials and Device Physics;* Choy, W. C. H., Ed.; Springer: New York, 2013; pp. 43-79.

(77)   Krebs, F. C.; Norrman, K. Analysis of the failure mechanism for a stable organic photovoltaic during 10 000 h of testing. *Prog. Photovoltaics Res. Appl.* **2007**, 15, 697-712.

(78)   Lögdlund, M.; Brédas, J. L. Theoretical studies of the interaction between aluminum and poly(p-phenylenevinylene) and derivatives. *J. Chem. Phys.* **1994**, 101, 4357-4364.

(79)   Rivaton, A.; Chambon, S.; Manceau, M.; Gardette, J.; Lemaître, N.; Guillerez, S. Light-induced degradation of the active layer of polymer-based solar cells. *Polym. Degrad. Stab.***2010**, 95, 278-284.

(80)   Po, R.; Carbonera, C.; Bernardi, A.; Camaioni, N. Interfacial Layers. In *Organic Solar Cells: Fundamentals, Devices, and Upscaling;* Rand, B. P.; Richter, H., Eds.; Pan Stanford: Boca Raton, FL, 2014; pp. 181-217.

(81)   De Jong, M. P.; Van Ijzendoorn, L. J.; De Voigt, M. J. A. Stability of the interface between indium-tin-oxide and poly(3,4-ethylenedioxythiophene)/poly(styrenesulfonate) in polymer light-emitting diodes. *Appl. Phys. Lett.* **2000**, 77, 2255-2257.

(82)   Kawano, K.; Pacios, R.; Poplavskyy, D.; Nelson, J.; Bradley, D. D. C.; Durrant, J. R. Degradation of organic solar cells due to air exposure. *Sol. Energ. Mat. Sol. C.* **2006**, 90, 3520-3530.

(83)   Park, S. H.; Roy, A.; Beaupré, S.; Cho, S.; Coates, N.; Moon, J. S.; Moses, D.; Leclerc, M.; Lee, K.; Heeger, A. J. Bulk heterojunction solar cells with internal quantum efficiency approaching 100%. *Nature Photon.***2009**, 3, 297-303.

(84)   Dam, H. F.; Larsen-Olsen, T. T.; How to measure solar cells. Plasticphotovoltaics.org - a hub for OPV research. http://plasticphotovoltaics.org/lc/characterization/lc-measure.html (accessed June 2, 2015).

(85)   Li, Y. Molecular Design of Photovoltaic Materials for Polymer Solar Cells: Toward Suitable Electronic Energy Levels and Broad Absorption. *Acc. Chem. Res.* **2012**, 45, 723-733.

(86)   Facchetti, A. Polymer donor-polymer acceptor (all-polymer) solar cells. *Mater. Today.* **2013**, 16, 123-132.

(87)   Anthony, J. E.; Facchetti, A.; Heeney, M.; Marder, S. R.; Zhan, X. n-Type Organic Semiconductors in Organic Electronics. *Adv. Mater.* **2010**, 22, 3876-3892.

(88)   Kim, Y.; Choulis, S. A.; Nelson, J.; Bradley, D. D. C. Composition and annealing effects in polythiophene/fullerene solar cells. *J. Mater. Sci.* **2005**, 40, 1371-1376.

(89)   Kim, Y.; Choulis, S. A.; Nelson, J.; Bradley, D. D. C.; Cook, S.; Durrant, J. R. Device annealing effect in organic solar cells with blends of regioregular poly(3-hexylthiophene) and soluble fullerene. *Appl. Phys. Lett.* **2005**, 86, 063502.

(90)   Reyes-Reyes, M.; Kim, K.; Carroll, D. L.; High-efficiency photovoltaic devices based on annealed poly(3-hexylthiophene) and 1-(3-methoxycarbonyl)-propyl-1-phenyl-(6,6)-C_{61} blends. *Appl. Phys. Lett.* **2005**, 87, 083506.

(91)   Padinger, F.; Rittberger, R. S.; Sariciftci, N. S. Effects of Postproduction Treatment on Plastic Solar Cells. *Adv. Funct. Mater.* **2003**, 13, 85-88.

(92)   Peet, J.; Kim, J. Y.; Coates, N. E.; Ma, W. L.; Moses, D.; Heeger, A. J.; Bazan, G. C. Efficiency enhancement in low-bandgap polymer solar cells by processing with alkane dithiols. *Nature Mater.* **2007**, 6, 497-500.

(93)   Allen, M. P.; Tildesley, D. J. *Computer simulation of liquids*; Oxford University: New York, 1987.

(94)   Frenkel D.; Smit, B. *Understanding molecular simulation: from algorithms to applications,* 2nd ed.; Academic Press: San Diego, CA, 2002.

(95)   Phan-Thien, N. Dissipative Particle Dynamics. *Understanding Viscoelasticity;* Graduate Texts in Physics; Springer-Verlag: Berlin Heidelberg, 2013; 147-194.

(96)   Alder, B. J.; Wainwright, T. E. Molecular dynamics by electronic computers. In *Proc. of the Int. Symp. On Statistical Mechanical Theory of Transport Processes (Brussels, 1956);* Progigine, I., Ed.; Wiley: New York, 1958; pp. 97-131.

(97)   Rahman, A. Correlations in the motion of atoms in liquid argon. *Phys. Rev.* **1964**, 136, A405-A411.

(98)   Hill, T. L. *An introduction to statistical thermodynamics*; Dover: New York, 1986.

(99)   McQuarrie, D. A. *Statistical mechanics*; Harper & Row: New York, 1976.

(100)   Cramer, C. J.; *Essentials of computational chemistry,* 2nd ed.; Wiley: Hoboken, NJ, 2004.

(101) Sun, H.; Ren, P.; Fried, J. R. The COMPASS force field: parameterization and validation for phosphazenes. *Comput. Theor. Polym. Sci.* **1998**, 8, 229-246.

(102) Sholl, D. S.; Steckel, J. A. *Density functional theory: a practical introduction*; Wiley: New Jersey, 2009.

(103) Berendsen, H. J. C.; Postma, J. P. M.; DiNola, A.; Haak, J. R. Molecular dynamics with coupling to an external bath. *J. Chem. Phys.* **1984**, 81, 3684-3690.

(104) Andersen, H. C. Molecular dynamics simulations at constant pressure and/or temperature. *J. Chem. Phys.* **1980**, 72, 2384.

(105) Nosé, S. A molecular dynamics method for simulations in the canonical ensemble. *Mol. Phys.* **1984**, 52, 255-268.

(106) Hoover, W. G. Canonical dynamics: equilibrium phase-space distributions. *Phys. Rev. A.* **1985**, 31, 1695-1697.

(107) Bussi, G.; Donadio, D.; Parrinello, M. Canonical sampling through velocity rescaling. *J. Chem. Phys.* **2007**, 126, 014101.

(108) van der Spoel, D.; Lindahl, E.; Hess, B.; GROMACS development team. *GROMACS User Manual version 4.6.5.;* 2013, www.gromacs.org

(109) Accelrys Software Inc. *Materials Studio Release Notes, Release 5.0;* Accelrys Software Inc.: San Diego, CA, 2009.

(110) Parrinello, M.; Rahman, A. Polymorphic transitions in single crystals: A new molecular dynamics method. *J. Appl. Phys.* **1981**, 52, 7182-7190.

(111) Nosé, S.; Klein, M. L. Constant pressure molecular dynamics for molecular systems. *Mol. Phys.* **1983**, 50, 1055-1076.

(112) Martyna, G. J.; Tuckerman, M. E.; Tobias, D. J.; Klein, M. L. Explicit reversible integrators for extended systems dynamics. *Mol. Phys.* **1996**, 87, 1117-1157.

(113) Hoogerbrugge, P. J.; Koelman, J. M. V. A. Simulating microscopic hydrodynamics phenomena with dissipative particle dynamics. *Europhys. Lett.* **1992**, 19, 155-160.

(114) Koelman, J. M. V. A.; Hoogerbrugge, P. J. Dynamic simulation of hard-sphere suspensions under steady shear. *Europhys. Lett.* **1993**, 21, 363-368.

(115)   Accelrys Software Inc. *Mesoscale simulation training materials* (accessed through personal communications)*;* Accelrys Software Inc.: San Diego, CA, 2014.

(116)   Español, P. Dissipative Particle Dynamics. *Handbook of Materials Modeling*; Springer: Netherlands, 2005; 2503-2512.

(117)   Groot, R. D.; Warren, P. B. Dissipative particle dynamics: Bridging the gap between atomistic and mesoscopic simulation. *J. Chem. Phys.* **1997**, 107, 4423-4435.

(118)   Flory, P. J. *Principles of Polymer Chemistry*, 6th ed.; Cornell University: Ithaca, NY, 1967.

(119)   Hamley, I. W. Introduction to Block Copolymers. In *Developments in Block Copolymer Science and Technology;* Hamley, I. W., Ed.; Wiley: Chichester, West Sussex, 2004; pp. 1-29.

(120)   Fredrickson, G. H. *The Equilibrium Theory of Inhomogeneous Polymers*; Oxford University: New York, 2006.

(121)   Kim, Y.; Cook, S.; Tuladhar, S. M.; Choulis, S. A.; Nelson, J.; Durrant, J. R.; Bradley, D. D. C.; Giles, M.; McCulloch, I.; Ha, C.-S.; Ree, M. A strong regioregularity effect in self-organizing conjugated polymer films and high-efficiency polythiophene: fullerene solar cells. *Nat. Mater.* **2006**, 5, 197-203.

(122)   Mauer, R.; Kastler, M.; Laquai, F. The Impact of Polymer Regioregularity on Charge Transport and Efficiency of P3HT:PCBM Photovoltaic Devices. *Adv. Funct. Mater.* **2010**, 20, 2085-2092.

(123)   Urien, M.; Bailly, L.; Vignau, L.; Cloutet, E.; de Cuendias, A.; Wantz, G.; Cramail, H.; Hirsch, L.; Parneix, J.-P. Effect of the regioregularity of poly(3-hexylthiophene) on the performances of organic photovoltaic devices. *Polym. Int.* **2008**, 57, 764-769.

(124)   Chuang, S.-Y.; Chen, H.-S.; Lee, W.-H.; Huang, Y.-C.; Su, W.-F.; Jen, W.-M.; Chen, C.-W. Regioregularity effects in the chain orientation and optical anisotropy of composite polymer/fullerene films for high-efficiency, large-area organic solar cells. *J. Mater. Chem.* **2009**, 19, 5554-5560.

(125)   Adachi, T.; Brazard, J.; Ono, R. J.; Hanson, B.; Traub, M. C.; Wu, Z.-Q.; Li, Z.; Bolinger, J. C.; Ganesan, V.; Bielawski, C. W.; Vanden Bout, D. A.; Barbara, P. F. Regioregularity and Single Polythiophene Chain Conformation. *J. Phys. Chem. Lett.* **2011**, 2, 1400-1404.

(126)   Woo, C. H.; Thompson, B. C.; Kim, B. J.; Toney, M. F.; Fréchet, J. M. J. The influence of Poly(3-hexylthiophene) Regioregularity on Fullerene-Composite Solar Cell Performance. *J. Am. Chem. Soc.* **2008**, 130, 16324-16329.

(127)   Sivula, K.; Luscombe, C. K.; Thompson, B. C.; Fréchet, J. M. J. Enhancing the Thermal Stability of Polythiophene: Fullerene Solar Cells by Decreasing Effective Polymer Regioregularity. *J. Am. Chem. Soc.* **2006**, 128, 13988-13989.

(128)   Ebadian, S.; Gholamkhass, B.; Shambayati, S.; Holdcroft, S.; Servati, P. Effects of annealing and degradation on regioregular polythiophene-based bulk heterojunction organic photovoltaic devices. *Sol. Energy Mater. Sol. Cells.* **2010**, 2258-2264.

(129)   Hoth, C. N.; Choulis, S. A.; Schilinsky, P.; Brabec, C. J. On the effect of poly(3-hexylthiophene) regioregularity on inkjet printed organic solar cells. *J. Mater. Chem.* **2009**, 19, 5398-5404.

(130)   Fermeglia, M.; Pricl, S. Multiscale modeling for polymer systems of industrial interest. *Prog. Org. Coat.* **2007**, 58, 187-199.

(131)   Jawalkar, S. S.; Adoor, S. G.; Sairam, M.; Nadagouda, M. N.; Aminabhavi, T. M. Molecular modeling on the binary blend compatibility of poly (vinyl alcohol) and poly (methyl methacrylate): An atomistic simulation and thermodynamic approach. *J. Phys. Chem. B.* **2005,** 109, 15611-15620.

(132)   Jawalkar, S. S.; Aminabhavi, T. M. Molecular modeling simulations and thermodynamic approaches to investigate compatibility/incompatibility of poly(l-lactide) and poly(vinyl alcohol) blends. *Polymer.***2006**, 47, 8061-8071.

(133)   Jawalkar, S. S.; Raju, K. V.S. N.; Halligudi, S. B.; Sairam, M.; Aminabhavi, T. M. Molecular modeling simulations to predict compatibility of poly(vinyl alcohol) and chitosan blends: A comparison with experiments. *J. Phys. Chem. B.* **2007**, 111, 2431-2439.

(134)   Jawalkar, S. S.; Nataraj, S. K.; Raghu, A. V.; Aminabhavi, T. M. Molecular dynamics simulations on the blends of poly(vinyl pyrrolidone) and poly(bisphenol-a-ether sulfone). *J. Appl. Polym. Sci.* **2008**, 108, 3572-3576.

(135)   Fu, Y.; Liao, L.; Yang, L.; Lan, Y.; Mei, L.; Liu, Y.; Hu, S. Molecular dynamics and dissipative particle dynamics simulations for prediction of miscibility in polyethylene terephthalate/polylactide blends. *Mol. Simul.* **2013**, 39, 415-422.

(136)   Luo, Z.; Jiang, J. Molecular dynamics and dissipative particle dynamics simulations for the miscibility of poly(ethylene oxide)/poly(vinyl chloride) blends. *Polymer.* **2010**, 51, 291-299.

(137)   Scocchi, G.; Posocco, P.; Fermeglia, M.; Pricl, S. Polymer-Clay Nanocomposites: A Multiscale Molecular Modeling Approach. *J. Phys. Chem. B.* **2007**, 111, 2143-2151.

(138) Lee, C.-K.; Pao, C.-W. Solubility of [6,6]-Phenyl-C61-butyric Acid Methyl Ester and Optimal Blending Ratio of Bulk Heterojunction Polymer Solar Cells. *J. Phys. Chem. C*. **2012**, 116, 12455-12461.

(139) Lee, C.-K.; Hua, C. C.; Chen, S. A. Single-Chain and Aggregation Properties of Semiconducting Polymer Solutions Investigated by Coarse-Grained Langevin Dynamic Simulation. *J. Phys. Chem. B*. **2008**, 112, 11479-11489.

(140) Lee, C.-K.; Hua, C. C.; Chen, S. A. Multiscale Simulation for Conducting Conjugated Polymers from Solution to the Quenching State. *J. Phys. Chem. B*. **2009**, 113, 15937-15948.

(141) Schwarz, K. N.; Kee, T. W.; Huang, D. M. Coarse-grained simulations of the solution-phase self-assembly of poly(3-hexylthiophene) nanostructures. *Nanoscale*. **2013**, 5, 2017-2027.

(142) Lee, C. S.; Dadmun, M. D. Important thermodynamic characteristics of poly(3-hexyl thiophene). *Polymer*. **2014**, 55, 4-7.

(143) Fu, Y.; Liao, L.; Yang, L.; Lan, Y.; Mei, L.; Liu, Y.; Hu, S. Molecular dynamics and dissipative particle dynamics simulations for prediction of miscibility in polyethylene terephthalate/polylactide blends. *Mol. Simul.* **2013**, 39, 415-422.

(144) Patel, S.; Lavasanifar, A.; Choi, P. Application of Molecular Dynamics Simulation To Predict the Compatibility between Water-Insoluble Drugs and Self-Associating Poly(ethylene oxide)-b-poly(ε-caprolactone) Block Copolymers. *Biomacromolecules*. **2008**, 9, 3014-3023.

(145) Khajeh, A. R. A.; Shankar, K.; Choi, P. Prediction of the Active Layer Nanomorphology in Polymer Solar Cells Using Molecular Dynamics Simulation. *Appl. Mater. Interfaces*. **2013**, 5, 4617-4624.

(146) Alexiadis, O.; Mavrantzas, V. G.; All-Atom Molecular Dynamics Simulation of Temperature Effects on the Structural, Thermodynamic, and Packing Properties of the Pure Amorphous and Pure Crystalline Phases of Regioregular P3HT. *Macromolecules*. **2013**, 46, 2450-2467.

(147) Grimme, S. Do Special Noncovalent π-π Stacking Interactions Really Exist? *Angew. Chem. Int. Ed.* **2008**, 47, 3430-3434.

(148) Noorjahan, A.; Choi, P. Thermodynamic properties of poly(vinyl alcohol) with different tacticities estimated from molecular dynamics simulation. *Polymer*. **2013**, 54, 4212-4219.

(149) Zhang, W.; Gomez, E. D.; Milner, S. T. Predicting Chain Dimensions of Semiflexible Polymers from Dihedral Potentials. *Macromolecules*. **2014**, 47, 6453-6461.